SCUOLA DI DOTTORATO
UNIVERSITÁ DEGLI STUDI DI MILANO-BICOCCA

Department of Materials Science

PhD Program in Materials Science and Nanotechnology
Cycle XXXVII

DESIGN OF FILLER MATERIALS WITH STIMULI-RESPONSIVE PROPERTIES FOR SMART COMPOSITES APPLICATIONS

PhD Candidate: Sara Fernanda ORSINI

Registration number: 811935

Tutor: Prof. Massimiliano D'ARIENZO

Coordinator: Prof. Francesco MONTALENTI

ACADEMIC YEAR 2023/2024

A mio nonno Antonio

Preface

In recent years, the need for materials that align with environmental sustainability, the circular economy, and energy efficiency has become increasingly urgent. This thesis focuses on the development of stimuli-responsive materials, with particular emphasis on hybrid materials and nanocomposites, which are pivotal for advancing both technology and sustainability. Hybrid materials, composed of both organic and inorganic components, have emerged as versatile solutions across various industries due to their ability to enhance mechanical, thermal, and optical properties. These materials not only offer advanced functionality, but they also provide opportunities to reduce environmental impact, an increasingly critical issue in materials science.

Reducing environmental impact can be achieved by utilizing materials derived from waste, which can be re-evaluated and repurposed, thus minimizing the reliance on raw resources. Additionally, optimizing the processes for developing new materials and improving the performance of existing ones can further mitigate their environmental footprint throughout their lifecycle. Stimuli-responsive materials, also known as smart materials, are particularly promising in addressing these challenges. These materials are designed to react to environmental changes, making them ideal for advanced applications

that require adaptability. Smart materials can sense and respond to stimuli such as light, heat, pH, or mechanical stress, undergoing reversible changes triggered by external conditions. For example, photo-responsive and thermo-responsive materials can undergo reversible structural changes when exposed to specific wavelengths of light or temperature gradients, respectively, further expanding their potential applications. Photo-responsive systems can be applied, for example, in the development of smart, biodegradable packaging materials that can assemble and disassemble on demand simply by changing the wavelength of light. This capability would not only allow for the recovery of the original materials but also reduce long-term waste accumulation. Similarly, thermo-responsive systems can be utilized in the creation of lubricants that are essential for reducing friction and wear in mechanical systems. This not only conserves energy but also extends the lifespan of machinery, thereby lowering the demand for raw materials and energy-intensive manufacturing processes. In a broader context, the thesis underscores the importance of continued innovation in designing materials that respond to environmental stimuli while adhering to the circular economy principles. By focusing on energy efficiency and reduction of environmental impact, the development of these advanced materials appears crucial for fostering sustainable processes and products which can be easily adapted to the evolving technological and ecological demand.

Contents

Glossary

AC	*Acrylic Coumarin*
AGU	*Anhydroglucose Unit*
APTES	*3-Aminopropyltriethoxysilane*
ATR-FTIR	*Attenuated Total Reflectance Fourier Transform Infrared*
BET	*Brunauer-Emmett-Teller Theory*
BJH	*Barrett-Joyner-Halenda Method*
CHNS	*Carbon, Hydrogen, Nitrogen, Sulfur elemental analysis*
CINN	*Cinnamic Acid*
CINN-APTES	*3-Aminopropyltriethoxysilane modified with Cinnamic unit*
CINN-NHS	*N-Hydroxysuccinimide Ester of Cinnamic Acid*
CNCl	*Cinnamyl Chloride*
CNCOCl	*Cinnamoyl Chloride*
CPMAS	*Cross Polarization Magic Angle Spinning*
CS1-3	*Cinnamyl Starch (1-3)*
DCC	*N,N'-dicyclohexylcarbodiimide*

DRS	*Diffuse Reflectance Spectroscopy*
DS	*Degree of Substitution*
DSC	*Differential Scanning Calorimetry*
EDX	*Energy Dispersive X-ray Spectroscopy*
GuPTES	*3-Aminopropyltriethoxysilane modified with Guanidinium unit*
HE TD-NMR	*Hanh Echo Time-Domain Nuclear Magnetic Resonance*
HMC	*7-Hydroxy-4-methylcoumarin*
HSQC	*Heteronuclear Single Quantum Coherence*
MPTMS	*3-(Methacryloyloxy)propyltrimethoxysilane*
NFs	*Nanofibers*
NHS	*N-Hydroxysuccinimide*
NLDFT	*Non-local Density Functional Theory*
NMR	*Nuclear Magnetic Resonance*
NPs	*Nanoparticles*
PS	*Pristine Starch*
PyZCA	*1H-Pyrazole-1-carboxamidine hydrochloride*
SEM	*Scanning Electron Microscopy*
Sep	*Sepiolite nanofibers*
SepGu-sPEG_Y	*Nanocomposite with SepOH@GuPTES NFs incorporated into sulfo-PEG with a relative weight ratio 1:Y respectively*
SepOH	*Pretreated sepiolite nanofibers*
SNFs	*Solvent-free Nanofluids*

SiGu-sPEG_Y	*Nanocomposite with SiO_2@GuPTES NPs incorporated into sulfo-PEG with a relative weight ratio 1:Y respectively*
SiO_2	*Silica*
SiO_2@CN	*Silica nanoparticles functionalized with CINN-APTES*
SiO_2@MP	*SiO_2 nanoparticles functionalized with MPTMS*
SiO_2@MP-AC	*SiO_2@MP modified with AC*
ss-NMR	*Solid-State Nuclear Magnetic Resonance*
sulfo-PEG	*Poly(ethylene glycol) 4-nonylphenyl 3-sulfopropyl ether potassium salt*
TEM	*Transmission Electron Microscopy*
TEOS	*Tetraethyl orthosilicate*
TGA	*Thermogravimetric Analysis*
UV-Vis	*Ultraviolet-Visible*
X	*SiO_2 NPs or SepOH NFs*
X@AP	*Filler functionalized with APTES*
X@AP-CN	*X@AP modified with CINN-NHS*
X@AP-CNCOCl	*X@AP modified with CNCOCl*
X@GuPTES	*Filler functionalized with GuPTES*

Chapter 1

Introduction and Aims

1.1 Hybrid materials and Nanocomposites

Recent technological advancements have significantly increased the demand for new materials with advanced functionalities. Traditional materials like metals, ceramics, and plastics are often unable to meet the diverse requirements of modern applications. In response, a new class of materials called "hybrid materials" has emerged. According to the International Union of Pure and Applied Chemistry (IUPAC), hybrid materials are composed of a blend of inorganic, organic, or both types of components that interpenetrate on a sub-micrometer scale. Today, hybrid materials are considered one of the most promising classes of innovative materials, with applications across a wide range of fields, including technology, optics, electronics, mechanics, and biology (Figure 1.1).[1–3]

Figure 1.1: Applications of composites and hybrid materials[2]

Developing hybrid materials is not solely a human innovation, as nature provides numerous examples, such as wood (cellulose fibres in a lignin matrix), bone (collagen reinforced with mineral apatite), crustacean shells, and mollusc shells. Nature has long achieved an optimal balance of durability, mechanical strength, density, permeability, hydrophobicity, and other material properties. Human inspiration for hybrid materials comes from observing these natural systems.[4–6]

While it is difficult to pinpoint exactly when humans began developing hybrid materials, ancient civilizations used mixtures of organic and inorganic components, such as pigments for decorative art, including paintings and frescoes.[7, 8] However, the systematic development of true hybrid materials began in the late 20th and early 21st centuries, driven by advancements in chemical and physical characterization techniques that enabled analysis at the sub-micrometer scale.[9]

The unique characteristic of hybrid materials lies in the fact that their final properties are not merely the sum of the individual properties of their components but are primarily derived from the strong synergy created at the interface between these components. The core concept of hybrid materials is this "hybrid interface" which is responsible for the advanced properties of the final material.[10, 11] The nature of the interface is crucial for classifying hybrid materials, which are divided into two main classes based on the type of interactions between their components (Figure 1.2). **Class I** includes materials where the interactions between the phases are weak, such as van der Waals forces, weak electrostatic interactions, or hydrogen bonds. In contrast, **Class II** comprises materials where the interactions are strong,

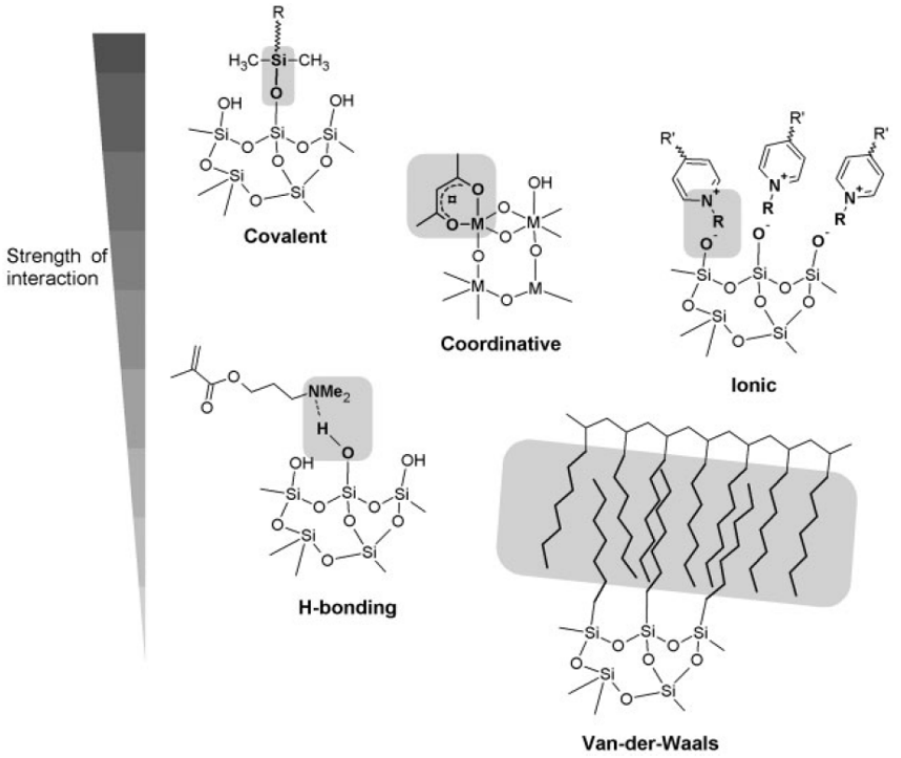

Figure 1.2: Typical interactions entailed in hybrid materials and their relative strength variations[10]

such as ionic, covalent, or coordination bonds. It is important to note, however, that in some cases, classification can be ambiguous, as a coordination bond may be weaker than a hydrogen bond. As a result, the classification of a material often requires evaluating the strength of chemical interactions on a case-by-case basis.[10]

The terms "hybrid material" and "nanocomposite" are often mistakenly used interchangeably, but they refer to distinct concepts. A nanocomposite is a type of hybrid material in which at least one component has at least one dimension in the 1-100 nm range. While it is accurate to call a nanocomposite a hybrid material, the reverse is not true, a hybrid material

is not necessarily a nanocomposite. This distinction is important because numerous studies have shown that nanoscale dimensions play a crucial role in significantly altering the final properties of the material, compared to non-nanoscale components. The size of the components at the nanoscale especially affects properties such as optical and mechanical behaviour.[2, 10]

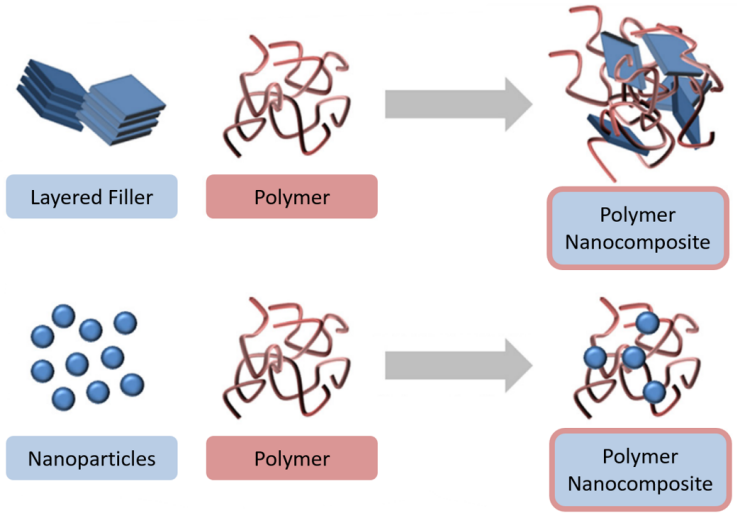

Figure 1.3: Overview of top-down approaches for preparing polymer nanocomposites[12]

Among all of them, polymer nanocomposites provide a creative platform for developing a wide range of new materials by combining organic flexibility with the robustness of inorganic components, generally designated as filler or nanofiller (Figure 1.3). These materials are highly adaptable, allowing for the incorporation of inorganic clusters or nanoparticles into organic polymer matrices, which enhances their optical, electronic, or magnetic properties. A key advantage is their polymer-like processability, eliminating the need for high-temperature treatments typically required for inorganic solids. This allows for shaping in bulk or film forms, which is particularly useful for

producing scratch-resistant coatings and improving material performance through surface treatments.[12–14]

Their optical transparency, achieved by avoiding light scattering, makes them ideal for optical applications. Phase separation between organic and inorganic components can also be controlled to create porous materials. The ability to modify the properties of polymer nanocomposites at the molecular scale with suitable filler enables the fine-tuning of characteristics like hydrophobicity, mechanical strength, or scratch resistance. Moreover, polymer nanocomposites are highly promising for smart technologies, offering applications in electrochromic systems, sensors, biohybrids, and electroactive materials, with improved stability and performance of organic or biomolecules when integrated into inorganic frameworks.[15–19]

In the following section, the main filler classes utilized in polymer nanocomposites will be described, with a specifical focus on SiO_2 nanoparticles and natural occurring clays fibers, which represent promising candidates in terms of performance, availability, sustainability, and costs.

1.2 Nanofillers

1.2.1 Nanofillers definition and classification

Nanofillers are nanoscale materials incorporated into polymer matrices to enhance or introduce specific properties, significantly improving the performance of the resulting polymer nanocomposites. These fillers can either be functional, designed to add new properties or improve existing ones, or act as extenders, where they serve merely as filler materials. The benefits of nanofillers stem from several factors, including their ability to improve mechanical, adhesive, thermal, electrical, and optical properties, depending on their homogeneous distribution within the matrix and the interaction between the filler and the polymer. The high surface-to-volume ratio of nanofillers plays a crucial role in maximizing these effects. Nanocomposites containing nanofillers are widely applied in various fields such as energy storage, electronics, coatings, biomedical devices, and catalysis.[20–23]

Nanofillers can be classified based on their **dimensions**, one of the key parameters for modulating the final properties of the composite, as well as their **porosity** and **chemical nature**. These parameters influence the way nanofillers interact with the polymer matrix and determine their utilization in specific applications.[13, 24]

Classification by dimensions

- One-dimensional nanofillers are characterized by one dimension in the range of 1-100 nm, typically exhibiting sheet-like structures, like for example montmorillonite, ZnO nanopatterns, and nanographene discs.

- Two-dimensional nanofillers have two of the three dimensions in the range of 1-100 nm. This category includes carbon nanotubes, boron nitride (BN) tubes, sepiolite fibers, gold and silver nanotubes, two-dimensional graphene, SiO_2, ZnO, and TiO_2.

- Three-dimensional nanofillers have all the three dimensions within the nanoscale range, like SiO_2, Al_2O_3, TiO_2, polyhedral oligomeric silsesquioxane (POSS), carbon black, and quantum dots.

Classification by porosity

- Macroporous nanofillers have pores with diameters greater than 50 nm.

- Mesoporous nanofillers feature pores ranging from 2 to 50 nm in diameter.

- Microporous nanofillers have pores smaller than 2 nm.

Classification by chemical nature

Nanofillers are also classified according to their chemical composition, which influences their interaction with the polymer matrix and dictates the types of applications for which they are best suited.

- Organic nanofillers that include nanoparticles derived from organic or natural sources, such as micelles, dendrimers, liposomes, and nanospheres. These materials are valued for their nontoxicity, biodegradability, and compatibility with biological systems.

- Inorganic nanofillers that include metallic nanoparticles, carbon-based nanoparticles, and ceramics like nanoclays and silicates. Inorganic fillers provide enhanced biocompatibility, hydrophilicity, and chemical stability, and are widely used in areas like optoelectronics, biomedicine, photocatalysis, and imaging.

Among the inorganic nanofillers, silica (SiO_2)[25–27] nanoparticles and natural clays (such as sepiolite, montmorillonite, and kaolinite)[28–32] play a key role in the mechanical reinforcement in polymer composites. These fillers are widely used in industries such as tire manufacturing, where they significantly enhance the Young's modulus (stiffness), heat resistance, solvent resistance, and transparency of the materials. Additionally, they play a key role in reducing flammability, a critical property for applications requiring fire retardance. Silica and clays are particularly effective in elastomeric matrices, where their high surface area enables strong filler-matrix interactions, resulting in improved mechanical performance. Furthermore, the hydroxyl groups on the surface of these materials allow them to form hydrogen bonds with water vapor, thereby improving the moisture absorption capabilities of the composite and reducing gas permeability. This makes them ideal for applications in coatings, packaging, and moisture barriers, where controlled permeability and absorption are critical.[33, 34] According to these considerations, the following sections provide a brief literature overview of the characteristics and exploitation in polymer nanocomposites of silica nanoparticles and phyllosilicates (specifically sepiolite nanofibers), including details on the effect of filler size/anisotropy and concentrations, as well as selected applications.

1.2.2 Silica Nanoparticles (SiO_2 NPs)

Silica (SiO_2) nanoparticles have gained significant attention as nanofillers due to their versatility and the wide range of properties they can impart to polymer composites.[33, 35] Although silica can be found naturally in crystalline forms such as quartz or cristobalite, synthetic silica is preferred for industrial applications due to its purity and tunable properties, typically produced in an amorphous form. The use of synthetic silica avoids the impurities present in natural sources, making it ideal for high-performance materials.[36, 37] Silica nanoparticles are particularly valued for their high surface area, low refractive index, and mechanical, thermal, and chemical stability, which make them useful across various industries, including catalysis, chromatography, pharmaceuticals, and food packaging.[35]

The synthesis of silica nanoparticles can be categorized into top-down and bottom-up approaches. Top-down methods reduce the size of bulk materials through mechanical or physical processes, while bottom-up methods involve chemical synthesis from atoms or molecules. One of the most commonly used bottom-up techniques is the sol-gel process, which offers precise control over the size, shape, porosity, and morphology of the nanoparticles by adjusting key reaction parameters such as temperature, pH, and the use of templating agents.[35] A notable example of this process is the Stöber method[38], developed in the 1960s, which enables the production of uniformly sized, monodisperse spherical silica nanoparticles. This method involves the hydrolysis of alkoxysilanes (e.g., tetraethoxyorthosilicate, TEOS) in an alcohol solution, followed by condensation to form Si-O-Si bonds. The process is typically catalyzed by ammonia, yielding spherical nanoparticles ranging in

size from 20 nm to several micrometres. This control over particle size and morphology is essential for tailoring the properties of silica nanocomposites. For instance, silica nanoparticles can significantly improve the composite material's mechanical strength, thermal resistance, optical transparency, and electrical properties. Additionally, the surface hydroxyl groups (Si-OH) present on silica nanoparticles can be functionalized with organic compounds to enhance compatibility between the inorganic filler and the organic polymer matrix, further improving the composite's performance.[39]

The ability to produce pure, homogeneous silica nanoparticles with controlled properties and the option to modify their surfaces, makes them particularly attractive as nanofillers. These particles are extensively used in applications requiring high-performance materials, including coatings, optical devices, and electronic applications. Their unique combination of properties ensures that silica nanoparticles continue to be a crucial component in developing advanced polymer nanocomposites. Rahman et al.[35] compiled a table summarizing examples of polymer nanocomposites incorporating SiO_2 nanoparticles, demonstrating that various parameters, such as the type of polymer, filler content, and nanoparticle size/morphology, can lead to different enhancements in the composite's properties (Figure 1.4).

1.2.3 Silicates: Structure, Properties, and Applications

The use of nanometer-sized silicates as fillers for nanocomposites emerged in the late 1980s to early 1990s, when montmorillonite nanoparticles were incorporated into a nylon-6 matrix, notably in the automotive industry.[40] Since then, research on these nanosilicates has expanded significantly, as they

Polymer matrix	Silica size (nm)	Silica content	Major property changes (with increasing filler content)	Reference
Polyurethane	175, 395 and 730	1–10 wt.%	Constant T_g at different particle size and concentrations	[66]
Epoxy (DGEBA)	400	50–70 wt.%	(i) Decreased CTE and increased T_g (ii) Increased brittleness	[46]
Epoxy (DGEBF)[a]	90	1–7 wt.%	(i) Increased fracture toughness (ii) Larger deformation resistance (up to 3 wt. %)	[67]
Polyimide	20	10–50 wt.%	(i) Increased dielectric constant (ii) Enhanced thermal stability	[68]
Epoxy (commercial)	25	1–14 vol.%	(i) Decreased T_g and increased T_β (ii) Increased microhardness, fracture toughness, and modulus	[65]
Thermoplastic polyurethane	7	10 wt.%	(i) Decreased T_g (ii) Increased shear and storage modulus (iii) Increased tensile and peel strength	[69]
Epoxy (DGEBA)[b]	240 & 1560	30 vol.%	(i) Increased storage and loss modulus (ii) Decreased T_g with the increase in the fraction of 1560 nm particles	[70]
Epoxy (commercial)	N/A	10–30 phr	(i) Decreased T_g (up to 20 phr) (ii) Decreased storage modulus and elastic modulus (up to 20 phr)	[71]
Epoxy (DGEBA)	75 and 330	1–5 wt.%	(i) Increased aggregation level (ii) Increased elastic modulus (modeled) (iii) Higher modulus for smaller particles	[72]
Epoxy (TGDDM)[c]	12.5	5 and 10 wt.%	(i) Decreased T_g, constant T_β (ii) Increased elastic and yield modulus (iii) Increased brittle fractureness	[73]
Epoxy (DGEBA)	10–20	10–70 wt.%	(i) Decreased T_g (ii) Increased thermal stability	[74]
Acrylic polymer[d]	15–20	10–50 wt.%	(i) Increased thermal stability (ii) Enhanced hardness (iii) Excellent optical transparency	[75]
Epoxy	4000	14–39 vol.%	(i) Increased Young's modulus (ii) Immonotonic variation in the yield strength and yield stress	[76]
Epoxy (BPA)[e]	9	2.17 vol.%	(i) Decreased frictional coefficient and specific wear rate (ii) Modified silica nanoparticles promote cure reaction of epoxy	[77]
Polyurethane	14–260	1–4 wt.%	(i) Increased T_g (ii) T_g increased with particle size up to 66 nm and then decreased (iii) Decreased surface and interface free energies by incorporation silica	[78]
Polystyrene	25–200	5–10 wt.%	(i) Increased DTA peaks (ii) Strong interaction between silanes group and polymer chains	[59]
Polyurethane	30	5	Increased SiO_2 dispersion	[79]
Polypropylene	50–110	1–5 wt.%	(i) Larger thermal degradation stabilization (ii) Larger elastic modulus	[85]

[a]Diglycidylether of bisphenol F; [b]Diglycidylether of bisphenol A; [c]Tetraglycidyl 4-4′-diaminodiphenylmethane; [d]Based on 3-(trimethoxysilyl)propyl methacrylate; [e]Bisphenol A epoxy resin (type E-51).

Figure 1.4: Overview of different types of silica-polymer nanocomposites reported in the literature, including details on filler sizes, concentrations, and select results[35]

offer improvements in the thermal and mechanical properties of composite materials, similar to other inorganic nanofillers but requiring much smaller quantities.[41, 42] The most utilized are the hydrated phyllosilicates, with the general chemical formula $(Ca,Na,H)(M)_2(Si,Al)_4O_{10}(OH)_2{\cdot}nH_2O$, where "M" represents metals such as aluminum, magnesium, iron, or zinc. These systems possess a lamellar or leaflet structure, with particle diameters typically ranging from 1 to 2 nanometers, but less than 4 nanometers overall. The structure of phyllosilicates consists of alternating layers of tetrahedral SiO_4 units and octahedral AlO_6 or MO_6 units, and the classification of these materials is strongly influenced by the arrangement of these layers and the specific metals present in the composition (Figure 1.5).[43]

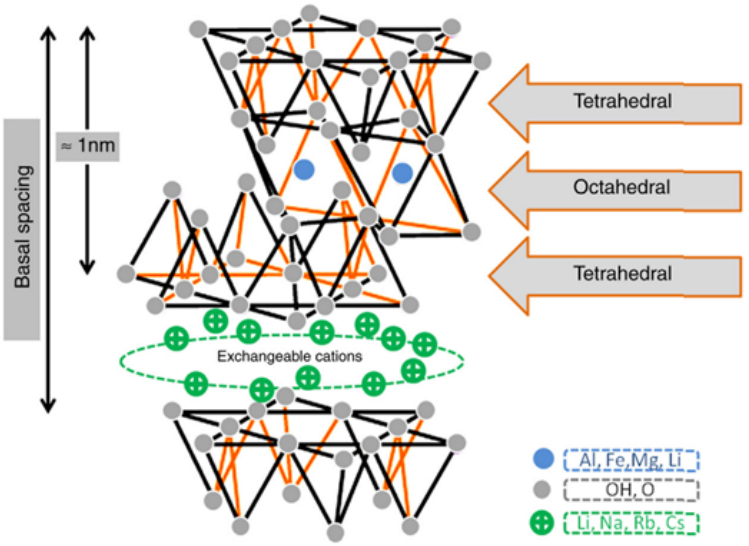

Figure 1.5: Structure of layered silicates[12]

Classification of phyllosilicates:

- 1:1 Silicates → In these minerals, each tetrahedral sheet is bonded to one octahedral sheet, creating alternating layers, as seen in kaolinite

and halloysite. This structure provides moderate reinforcing properties but limits their use in high-performance applications due to weaker interlayer interactions.

- 2:1 Silicates → These comprise two tetrahedral sheets sandwiching one octahedral sheet, as observed in montmorillonite, smectite, and vermiculite. The 2:1 arrangement increases the material's strength, flexibility, and thermal stability, making these minerals highly desirable for advanced applications. The layers in these materials are held together by weak forces, allowing intercalation of water and polar substances between the layers, enhancing their filler performance.

The incorporation of nanometer-sized clays or silicates into polymer matrices offers several key benefits: enhanced mechanical strength[44] due to their layered structure and high aspect ratio, which improves stiffness and tensile strength; increased thermal stability[45] by acting as barriers to heat flow; improved barrier properties[46] for reduced gas permeability, important for applications like food packaging; the ability to achieve these enhancements with low filler content, making materials lighter and more efficient; and maintaining biodegradability[47], particularly with natural silicates like montmorillonite and sepiolite, supporting eco-friendly applications. While advantageous as fillers in polymer nanocomposites, silicates face challenges such as aggregation, where strong van der Waals forces lead to particle clumping, reducing their effectiveness. Exfoliation is another issue, as some silicates like sepiolite do not exfoliate easily, limiting their ability to reinforce polymer matrices. Additionally, the hydrophilicity of many silicates makes them incompatible with hydrophobic polymers, often requiring surface modifications to improve dispersion and performance.[48] Sepiolite, a fibrous silicate,

stands out from other phyllosilicates due to its unique structure and distinct properties, including high surface area and porosity. The next section will describe in detail the main structural features of Sepiolite fibers.

1.2.3.1 Sepiolite

The structure of sepiolite consists of two-dimensional sheets of silica tetrahedra with a central magnesium octahedral sheet. Additionally, the structure exhibits an inversion of the apical tetrahedral units every six units, leading to the presence of surface Si-OH groups. These groups, similar to those on silica, enhance the reactivity of sepiolite and allow for chemical modifications and functionalization. The sheets are about 1.34 nm thick and are covalently bonded in a "checkerboard" pattern, which prevents exfoliation (Figure 1.6). Sepiolite appears as needle-like fibers, measuring between 40-150 nm in width and 1-10 µm in length. These fibers often aggregate into bundles with diameters ranging from 0.1 to 1 µm, which further combine into larger, randomly oriented aggregates ranging from 10 to 100 µm in size.[49]

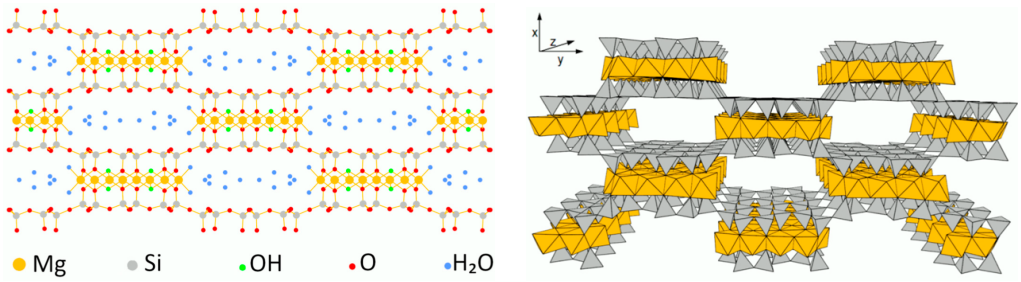

Figure 1.6: Models of sepiolite structure: (left) ball-and-stick model, (right) polyhedral representation[50]

The Si-OH groups on the sepiolite surface enable chemical modification, improving its compatibility with polymer matrices. This modification allows

for the self-assembly of sepiolite fibers within polymer networks, contributing to enhanced mechanical properties in the resulting nanocomposites. Furthermore, the fibrous morphology of sepiolite provides unique reinforcing characteristics, improving the elastic modulus of the nanocomposites in which it is incorporated.[51]

Sepiolite has a wide range of applications due to its fibrous structure and large surface area. In polymer nanocomposites, it acts as a filler, significantly enhancing mechanical strength and thermal stability, particularly in polymers such as styrene-butadiene rubber, where its fibers exhibit self-assembling behaviour.[52] In bio-nanocomposites sepiolite is preferred for food packaging applications because it improves mechanical properties and barrier performance while retaining biodegradability.[53] Its large surface area also makes sepiolite valuable in catalysis, offering abundant sites for adsorption and promoting chemical reactions.[54] Additionally, sepiolite is utilized in environmental remediation, where its porosity and high surface area allow it to effectively adsorb pollutants, making it a valuable material in environmental cleanup efforts.[55] While challenges such as aggregation and limited exfoliation persist, the potential of silicates, particularly in biodegradable materials and environmental technologies, highlights their importance in modern materials science.

In summary, nanofillers are versatile materials that, when integrated into polymer matrices, enhance a wide range of properties, including mechanical strength, thermal stability, and optical transparency, as a function of their size, shape and aspect ratio. Their action in nanocomposites encompasses a suitable incorporation/dispersion in the host matrix, which strongly re-

lies not only on the morphological features but, most importantly, on their surface features. In line with these considerations, the following section will cover the aspect of the surface compatibilization of filler nanomaterials and the effect of the surface functionalization on the final polymer nanocomposite properties.

1.3 Compatibilizing agents and functionalization reaction

Achieving homogeneous dispersion of the nanofiller is a critical issue as it directly influences the ultimate properties of the material. There are two primary approaches to pursue this goal: the first involves the effective dispersion of the nanofiller within the polymer matrix by exploiting specifically tailored mixing or incorporation techniques; the second involves the chemical surface modification of the nanofiller to enhance its compatibility with the polymer. The polymer matrix may also undergo chemical modifications to further improve compatibility with the nanofiller.

Focusing on the second approach, extensive research efforts demonstrated that surface functionalization of nanofillers can significantly improve the compatibility between the organic and inorganic components, leading to better dispersion. The potential applications of these advancements span numerous fields, including microelectronics, dyes, packaging, and biomedicine.[39, 56]

For silica and silicates, surface functionalization through silanes is particularly effective. These compatibilizing agents, with the general chemical formula $Si(OR)_3R'$, feature a $Si(OR)_3$ group that reacts with hydroxyl groups on the nanofiller surface, while the R' group interacts with the polymer matrix. Figure 1.7 illustrates some commonly used silanes.[35]

Among silanes, 3-aminopropyltriethoxysilane (APTES) is particularly important due to its versatile amine functionality. APTES is widely used for

Name (acronym)	Formula
Vinyltriethoxysilane (VTS)	$(C_2H_5O)_3Si–CH=CH_2$
Methacryloxypropyltriethoxysilane (MPTS)	$(C_2H_5O)_3Si–CH_2CH_2CH_2–O–CO–C(CH_3)=CH_2$
3-Glycidyloxypropyltrimethoxysilane (GPTS)	$(CH_3O)_3Si–CH_2CH_2CH_2–O–CH_2CH(O)CH_2$
3-Aminopropyltrimethoxysilane (APTS)	$(CH_3O)_3Si–CH_2CH_2CH_2NH_2$
3-Mercaptopropyltriethoxysilane (McPTS)	$(C_2H_5O)_3Si–CH_2CH_2CH_2SH$
Chloropropyltriethoxysilane (CPTS)	$(C_2H_5O)_3Si–CH_2CH_2CH_2Cl$

Figure 1.7: Commonly used silane coupling agents[35]

metal cation sequestration, the formation of salt bridges, and as a basic catalyst.[57] It also facilitates reactions with activated derivatives of carboxylic acids, forming amides and enabling the covalent anchoring of various organic compounds onto inorganic nanoparticles. Similarly, methacryloxypropyltrimethoxysilane (MPTMS) anchors organic molecules or polymers. In this case, radical reactions between acrylic or methacrylic groups are exploited, allowing the formation of longer polymer chains from small organic molecules. This ability to anchor organic compounds is highly valuable, as it imparts specific functionality to the filler, enhancing the properties and applications of the final system.[17]

In general, most studies employ two different strategies. The first is a conventional two-step process, in which the filler is first functionalized with a silane (such as APTES or MPTMS), and then the organic functionalities grafted onto the surface are modified with the desired functionality in a subsequent step.[58] The second entails a one-pot technique, where both the functionalization of the filler and the modification of the silane's terminal group occur simultaneously.[59] However, both methods have drawbacks, since they can result in low reaction yields of the modification of the silane's terminal group and, consequently, the unreacted groups may impart insta-

bility to final application of the system.

The ideal scenario is to have a pure silane containing the desired functional group. However, when such a silane is not commercially accessible, a potential alternative is to synthesize the required silane from an available one (e.g., APTES) under conditions that prevent the self-condensation of the silanol groups.

Surface functionalization of silica and silicates with silanes can be performed in either aqueous or non-aqueous environments. Non-aqueous conditions are generally preferred when using APTMS or APTES, as the amine group can promote uncontrolled hydrolysis and polycondensation in aqueous environments. Organic solvents, by contrast, allow for better control of reaction parameters, with the reaction typically proceeding via direct condensation under reflux. However, for large-scale production, aqueous environments are more practical. In these cases, silanes first undergo hydrolysis and condensation, forming siloxane bonds and releasing water, as illustrated in Figure 1.8.[35]

Several key parameters influence the success of the functionalization reaction with organosilanes, including temperature, the concentration of organosilane, and the amount of water and solvent used. Proper control of these factors enables the formation of a homogeneous single layer of organosilane on the nanoparticle surface. Conversely, excessive amounts of water and silane can lead to the formation of uncontrolled multilayer structures. In extreme cases, this results in sol-gel condensation and gelation rather than effective particle functionalization, due to dominant hydrolysis and self-condensation

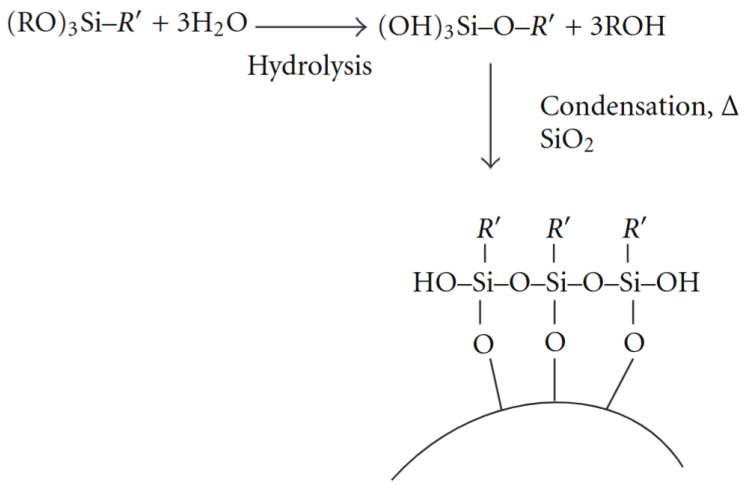

Figure 1.8: Chemical modification of silica surfaces in an aqueous system[35]

mechanisms.

For SiO_2 nanoparticles, one-pot synthesis methods in which synthesis and functionalization occur simultaneously have been developed. This approach reduces time and energy compared to the conventional process, involving nanoparticle synthesis and functionalization. Conversely, in the one-pot method, silanes or TEOS co-condensation occurs via a modified Stöber process. However, while the traditional approach preserves particle size and porosity distribution, the one-pot strategy often results in larger nanoparticles.[39]

A notable example of the impact of surface functionalization on nanocomposite properties is presented in a study by D'Arienzo et al.[17] In this research, the inclusion of TMMS (3-methacryloxypropyltrimethoxysilane) as a compatibilizing agent in a composite of silica nanoparticles (SiO_2) and ladder-like polysilsesquioxane (LPMASQ) brings several advantages. The TMMS functionalization enhances compatibility between the silica nanoparticles and the

silsesquioxane matrix, resulting in better dispersion and stronger interactions. This leads to more homogeneous surfaces and a marked improvement in thermal stability, with an increase of about 30°C compared to composites without TMMS. Additionally, TMMS functionalization boosts hydrophobicity by providing methacrylate groups, which react with those in LPMASQ, optimizing the polymer-filler interaction without increasing surface roughness of the film. This study highlights how including a functionalizing agent improves filler dispersion within the polymer matrix and, through cross-linking with the matrix, forms a network that significantly enhances the hydrophobic properties of the nanocomposite film (Figure 1.9).

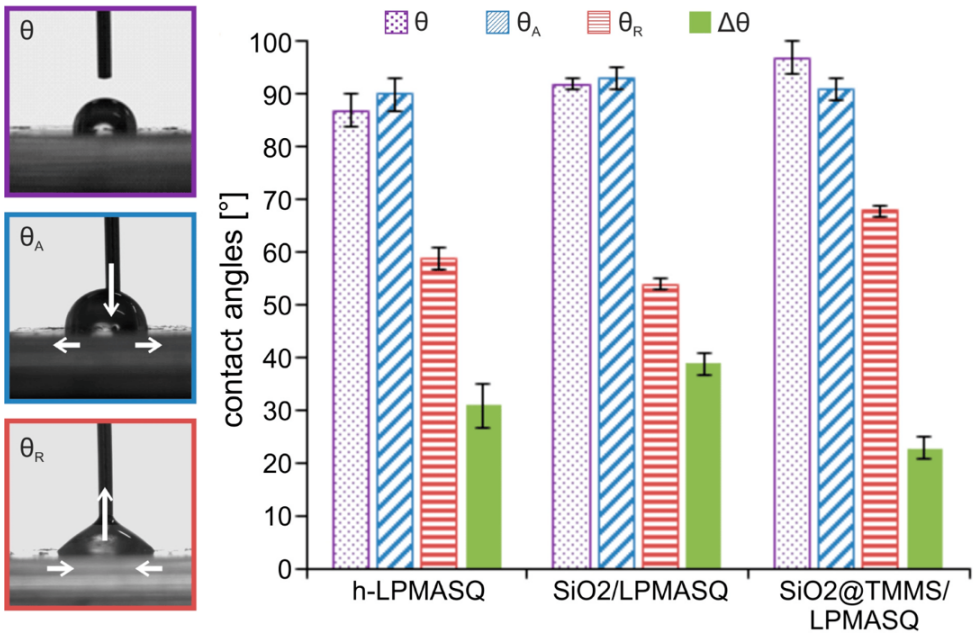

Figure 1.9: Contact angle values for LPMASQ, SiO_2/LPMASQ, and SiO_2@TMMS/LPMASQ surfaces. The images on the left show representative snapshots for the static contact angle (top), the advancing contact angle (θ_A, center), and the receding contact angle (θ_R, bottom)[17]

1.4 Smart polymer nanocomposites: an emerging class of materials

In recent years, a new era of smart materials and technologies has emerged alongside the hybrid and composite materials era. The definition of smart materials, however, remains somewhat controversial. Spillman Jr. et al.[60] attempted to better define the field of smart materials and structures, examining their current state and potential benefits. Their analysis of survey results and other contributions revealed a broad range of sometimes conflicting views, all of which are considered to align with the concept of smart materials and structures. The conclusion is that smart materials are advanced materials capable of responding to external or internal stimuli and environmental changes, triggering specific functions in response. These materials represent an evolution in materials science, from inert substances to materials designed for specific functions and, ultimately, to materials capable of adaptive, active, and intelligent responses.[61, 62]

The definition of smart materials has expanded to include materials that can receive, transmit, or process stimuli and respond by producing a useful effect, which may include signaling their response. These stimuli can range from strain, stress, temperature, and chemicals (including pH) to electric and magnetic fields, hydrostatic pressure, radiation, and more. In addition, a key criterion for a material to be considered "smart" is that its ability to receive and respond to stimuli in a useful way must be reversible during its performance lifecycle. Materials that are formally classified as smart include piezoelectric materials, electrostrictive materials, electrorheological materials, magnetorheological materials, thermoresponsive materials,

pH-sensitive materials, UV-sensitive materials, smart polymers, smart gels (such as hydrogels), smart catalysts, and shape memory alloys. Technical applications of smart structures include composite materials embedded with fiber optics, microelectromechanical systems (MEMS), vibration and sound control, shape control, health or lifetime monitoring, intelligent processing, self-repair (healing), artificial organs, and advanced damping systems. They are used in a wide range of industries, including automobiles, aerospace (space systems, aircraft), naval vessels, civil engineering, machine tools, recreational equipment, and medical devices (Figure 1.10).[63]

Among the various smart materials, two classes have gained significant attention in recent years: photo-responsive nanocomposites and stimuli-responsive solvent-free nanofluids. Their main characteristics, action mechanisms and applications will be described in the following sections.

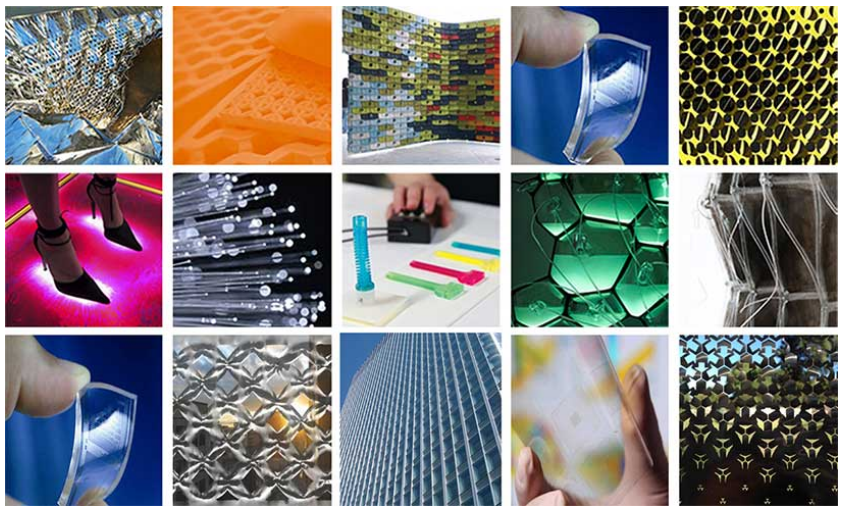

Figure 1.10: Examples of current applications of smart materials[64]

1.4.1 Photo-responsive polymer nanocomposites

The use of light as a stimulus to impart properties to the materials is particularly appealing due to its ability to be controlled remotely and precisely. Light can be switched rapidly and focused on specific areas, allowing for targeted responses. Many photoreactive systems have been inspired by nature, which has evolved complex biological mechanisms that harness light as a source of energy and information. For instance, light-induced cis-trans isomerization in the retinal-bound protein opsin initiates a cascade of events, including protein conformation and membrane permeability changes, ultimately leading to neural signaling and the perception of light.[65, 66] Photoresponsive materials can also be used for the development of smart nanocomposite. For example, Liu et. al[67] reports the development of a photoresponsive nanocomposite using self-assembly of an azobenzene-modified silane in a silica framework. The azobenzene molecules, known for their light-induced isomerization, were incorporated into mesoporous silica films. The resulting nanocomposite exhibited reversible photoisomerization between trans and cis forms upon exposure to UV light or heat, which in turn controlled the pore size and surface properties (Figure 1.11). These dynamic properties have potential applications in controlled release systems, molecular valves, and optically switchable membranes.

Another interesting study presents the development of a nanostructured, photoresponsive film made from a coumarin-modified monomer that exhibits photoreversibility and self-healing properties (Figure 1.12). The film can polymerize and depolymerize using UV light without the need for catalysts, heat, or other stimuli. Key findings include the ability to heal scratches

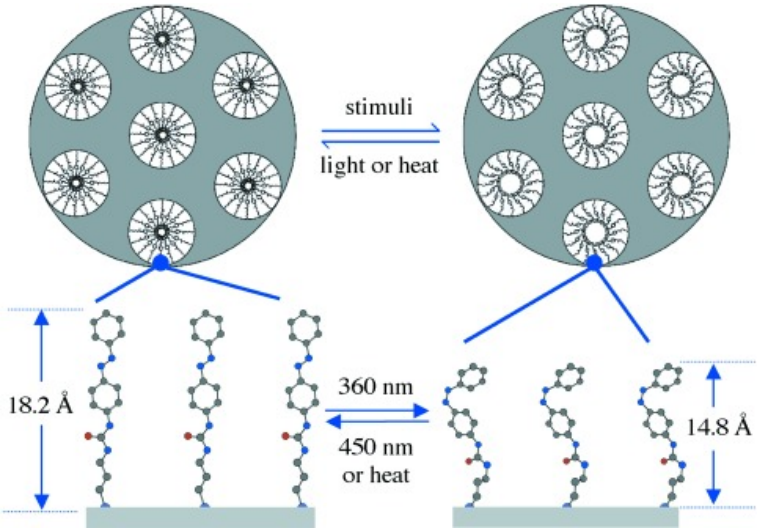

Figure 1.11: Photoresponsive nanocomposites prepared by evaporation-induced self-assembly procedure[67]

by merely using UV light and significant mechanical properties recovery after damage. Photoreversible reactions, such as the $2\pi + 2\pi$ cycloaddition of coumarin moieties, enable the polymer network to reversibly form and break under different UV wavelengths, resulting in highly reversible polymerization and potential for recyclability. The mechanism was confirmed using infrared and UV-visible spectroscopy, and molecular weight changes were tracked by GPC analysis. This photoreversible process allows the polymer to transition from a cross-linked state back to monomers and oligomers, enabling the film to self-heal after damage, with up to 91% recovery in mechanical properties.[68]

In recent years, growing environmental and sustainability concerns have highlighted the urgent need to reduce the reliance on fossil-based raw materials and lower net CO_2 emissions. As a result, biobased materials have gained

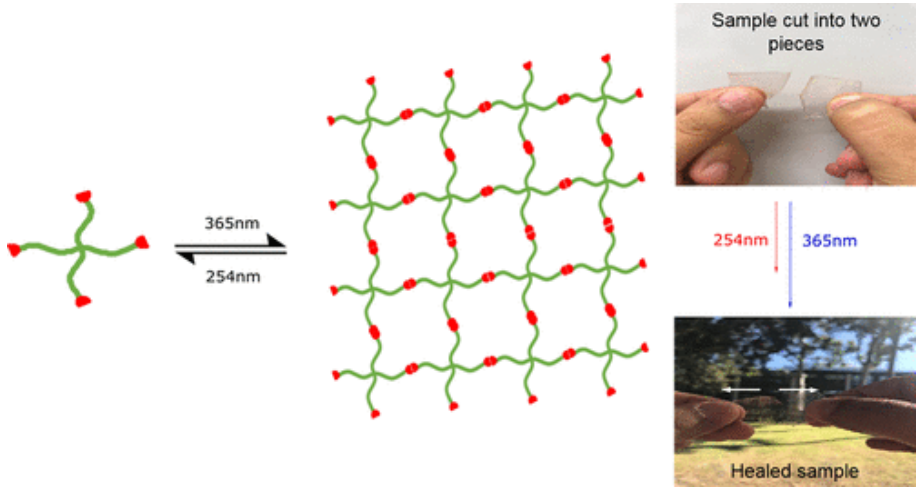

Figure 1.12: Schematic illustration of the preparation of photoreversible smart polymers[68]

significant attention across various fields, including the development of photoresponsive biobased materials.[69] The term "biobased" refers to materials or products that are wholly or partially derived from biomass sources such as plants, vegetables, and microorganisms.

One example of photoresponsive biobased materials is a study, done by Zhang et al[70], which explores the use of cellulose nanocrystals (CNCs), derived from wood pulp, as UV-absorbing and reinforcing agents in poly(vinyl chloride) (PVC) films. In this study, the CNCs are modified with cinnamate groups, which absorb UV light and undergo $2\pi + 2\pi$ cycloaddition crosslinking when exposed to UV radiation (Figure 1.13). This modification enhances the UV resistance, thermal stability, and mechanical strength of the PVC films. The resulting films remain transparent to visible light while effectively blocking harmful UV radiation, making them ideal for protective coatings and packaging applications. Moreover, the renewable origin of CNCs adds to the environmental sustainability of these materials.

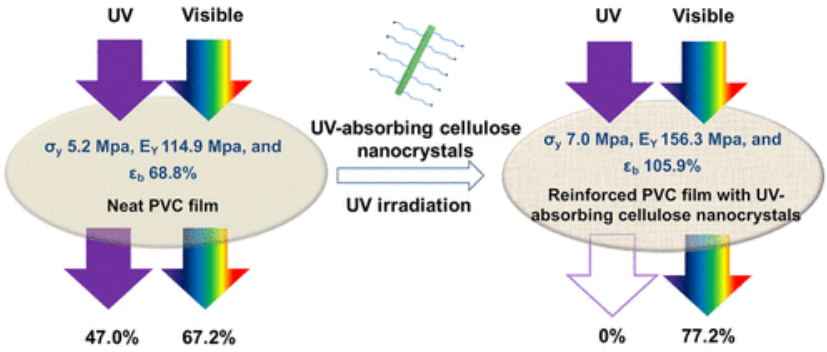

Figure 1.13: UV-Absorbing Cellulose Nanocrystals as Functional Reinforcing Fillers in Poly(vinyl chloride) Films[70]

Another example concerns developing a biobased, photo-reversible self-healing polymer derived from lignin, a renewable resource. This polymer uses cinnamate-like monomers that enable crosslinking and UV-triggered decomposition through a $2\pi + 2\pi$ cycloaddition reaction. When exposed to UV light, these polymers can autonomously heal cracks without external intervention, demonstrating significant self-healing capabilities. With their eco-friendly, renewable origin and UV-responsive properties, these polymers have potential applications in various industries (Figure 1.14).[71]

Both examples illustrate how biobased materials can contribute to developing sustainable, environmentally friendly technologies while offering advanced functional properties.

In summary, various light-induced processes, including isomerization, Diels-Alder cyclization, coordination, disulfide exchange, transesterification, imine formation, and photodimerization reactions, are being utilized to develop photoresponsive (bio)materials. In particular, the $2\pi + 2\pi$ cycloaddition

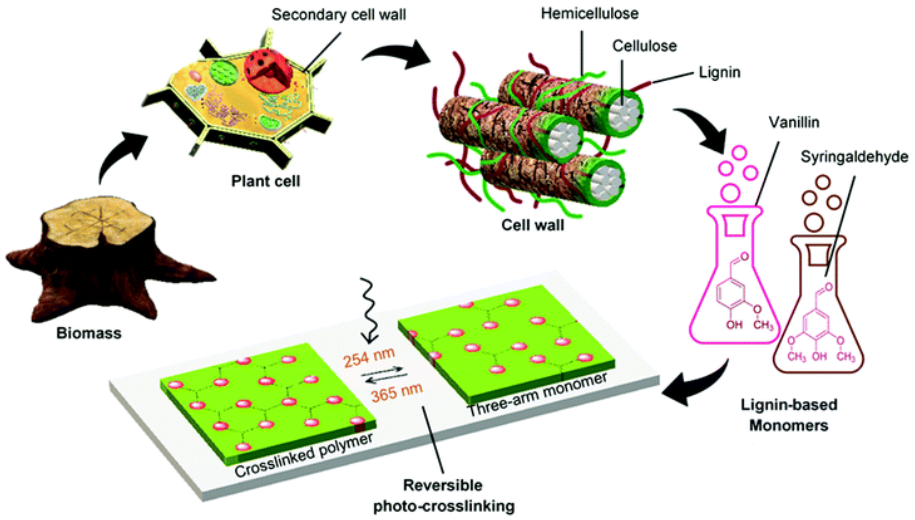

Figure 1.14: Synthesis of photo-responsive polymers from lignin-based monomers[71]

reaction seems to be very promising and easy to be exploited for these purposes. In view of these considerations, the mechanism and the functional groups suitable to undergo this photoinduced process will be described in the next subsection.

1.4.1.1 Photoreversible $2\pi + 2\pi$ cycloaddition reactions and photoreversible units

A growing area of focus is the $2\pi + 2\pi$ cycloaddition reactions, which allow control over material structures and their properties through light exposure. This photochemical reaction involves the formation of a cyclobutane ring from two alkene reactants through a typical photochemical mechanism. The process occurs via an interaction between the HOMO (π^*) of one alkene and the LUMO (π) of another alkene, following a suprafacial pathway, as illustrated in Figure 1.15.[72]

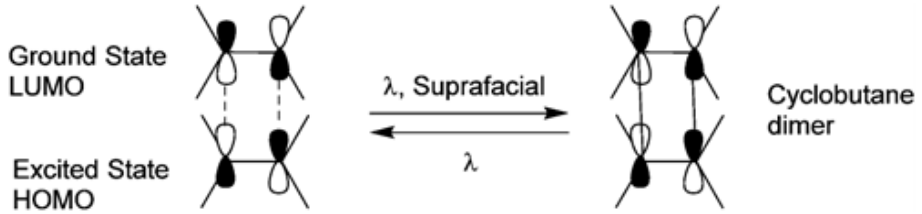

Figure 1.15: Orbital symmetry required for suprafacial [$2\pi + 2\pi$] cycloaddition of two generic alkenes[72]

These reactions have been applied to create new materials, including 2D nanosheets and photoresponsive molecular organic frameworks (MOFs), although some require specific conditions like a crystalline state. Recent progress includes the development of photoreversible linear polymers, particularly using $2\pi + 2\pi$ cycloadditions with thymines and styrylpyrene.[73]

Cinnamic acid, stilbene, thymine, coumarin are typical molecules which can undergo these sustainable reactions, as both forward and reverse processes are light-driven (see Figure 1.16).

In particular, cinnamic acid and coumarin have recently attracted great interest as both naturally occurring molecules found in various plants. Cinnamic Acid is commonly derived from the bark of cinnamon trees (Cinnamomum species) and is also found in other plants like balsams and certain fruits. It is part of the phenylpropanoid pathway in plants, which synthesizes various secondary metabolites. Cinnamic acid is a precursor for lignins, flavonoids, and other important plant compounds. Its natural occurrence makes it a sustainable candidate for use in eco-friendly nanocomposite materials. Coumarin is found in many plants, including tonka beans

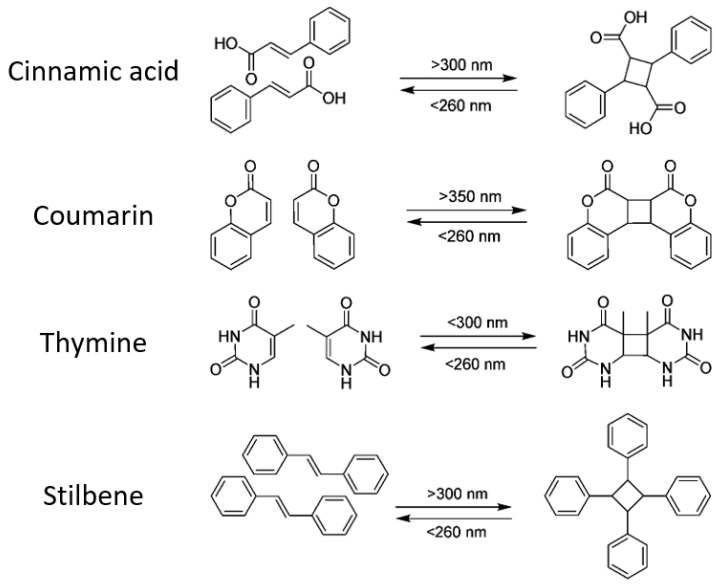

Figure 1.16: Moieties capable of undergoing photo-reversible dimerization by UV irradiation[72]

(Dipteryx odorata), sweet clover (Melilotus species), and some grasses. It has a characteristic vanilla-like scent and is used in perfumes and flavorings. In plants, coumarin plays a role in defence mechanisms against herbivores and pathogens. Its natural abundance and renewable sourcing make it an attractive option for developing sustainable materials. Both molecules' natural origin provides the potential for creating biodegradable and environmentally friendly nanocomposites.[74, 75] Mostly coumarin derivatives anchored to hybrid NP surfaces have been explored, providing several examples of either potential drug-delivery or light-triggered assembly systems. An interesting study discusses the modification of MCM-41 mesoporous silica with a photoresponsive coumarin derivative, allowing for controlled storage and release of guest molecules. UV light induces photodimerization of coumarin, closing the pores and trapping molecules like phenanthrene inside. Exposure to

shorter UV wavelengths breaks the dimer, releasing the trapped molecules (Figure 1.17).[76]

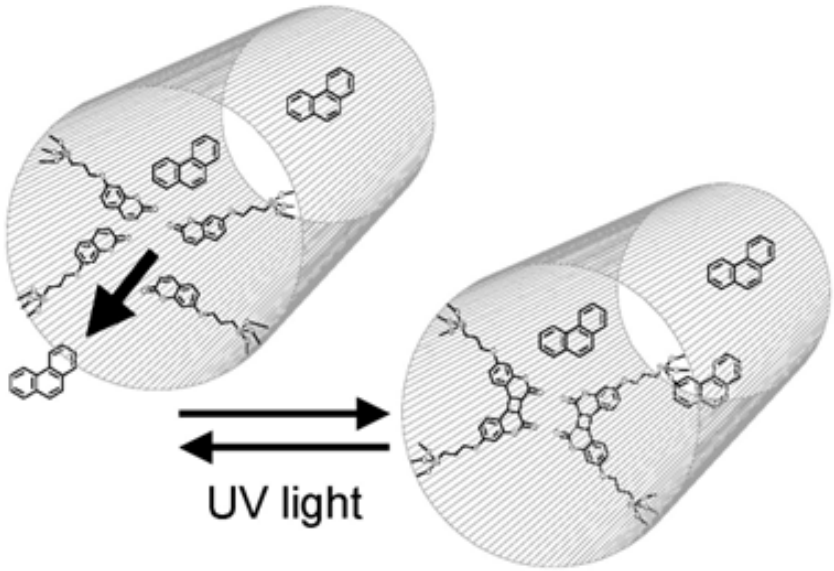

Figure 1.17: Mechanism of Photo-Switched Storage and Release of Guest Molecules in the Pore Void of Coumarin-Modified MCM-41[76]

1.4.2 Stimuli-responsive Solvent-free Nanofluids (SNFs)

Solvent-free nanofluids (SNFs) are advanced liquid-like materials consisting of nanoparticles (either inorganic or organic) functionalized with polymer chains, providing exceptional mechanical, thermal, and electrical properties. These nanofluids do not require traditional solvents, which makes them environmentally friendly and reduces potential issues like solvent evaporation. The long polymer chains grafted onto the surface of the nanoparticles prevent their aggregation, allowing the nanoparticles to remain stably dispersed. As a result, SNFs display liquid-like behavior even at room temperature, which

enhances their processability and usability across various applications.[77, 78]

SNFs are composed of two main parts:

1. **Core** → This represents the nanoparticle, which can be classified into three broad categories:

   - Inorganic nanomaterials include materials like titanium dioxide (TiO_2), silica (SiO_2), magnetite (Fe_3O_4), calcium carbonate ($CaCO_3$), graphene oxide (GO), carbon nanotubes (CNTs), and kaolinite. These materials are often chosen for their unique optical, magnetic, mechanical, and catalytic properties.
   - Small organic molecules include tetraaniline (TANI), which provides certain properties like electrical conductivity and liquid-crystalline behavior.
   - Organic-inorganic hybrids materials like polyaniline-Fe_3O_4, metal-organic frameworks (MOFs), and polyhedral oligomeric silsesquioxane (POSS), which combine properties from both organic and inorganic components for specialized applications.

2. **Shell** → The core is wrapped with an organic shell, consisting of a single or double layer of polymer chains. These chains include materials such as polysiloxane, polyetheramine, or sulfonates. The shell weakens the interaction between the nanoparticles, preventing aggregation and ensuring that the nanoparticles remain stably dispersed. The shell essentially acts as a substitute for traditional solvents, allowing the nanoparticle to exhibit liquid-like flow behavior, which improves its thermal stability and ease of processing.

The fabrication techniques greatly influence the properties of SNFs, including their mechanical strength, conductivity, and stability. The main methods for fabricating SNFs include physical adsorption (nanoparticles with hydroxyl-rich surfaces can physically adsorb polymers onto their surface), covalent bonding (organic molecules can form covalent bonds with surface groups like hydroxyl or carboxyl groups on the nanoparticles), ionic bonding (an inner organic layer, or “corona,” is covalently bonded to the nanoparticle core, the outer flexible long organic chains, known as the "canopy," are attached through ionic bonds) (Figure 1.18). The last one is the most common strategy for preparing SNFs as it ensures stability and enhances properties like mechanical strength and conductivity. This method allows the nanoparticles to retain their physical and chemical properties while exhibiting enhanced fluidity and processability.[79]

Solvent-free nanofluids (SNFs) possess a range of distinctive properties and benefits that make them highly versatile materials. One of their key attributes is their high dispersion stability, which comes from the polymer shell that prevents nanoparticles from aggregating, ensuring consistent application performance. This stability and enhanced mechanical, thermal, and electrical properties allow SNFs to excel when durability, heat resistance, and conductivity are crucial. Moreover, SNFs exhibit liquid-like behaviour even at room temperature, making them highly processable without needing for traditional solvents. This simplifies handling and makes them more environmentally friendly by reducing solvent-related concerns. Additionally, the unique structure of SNFs improves their thermal stability, making them resilient in high-temperature environments.[77, 79]

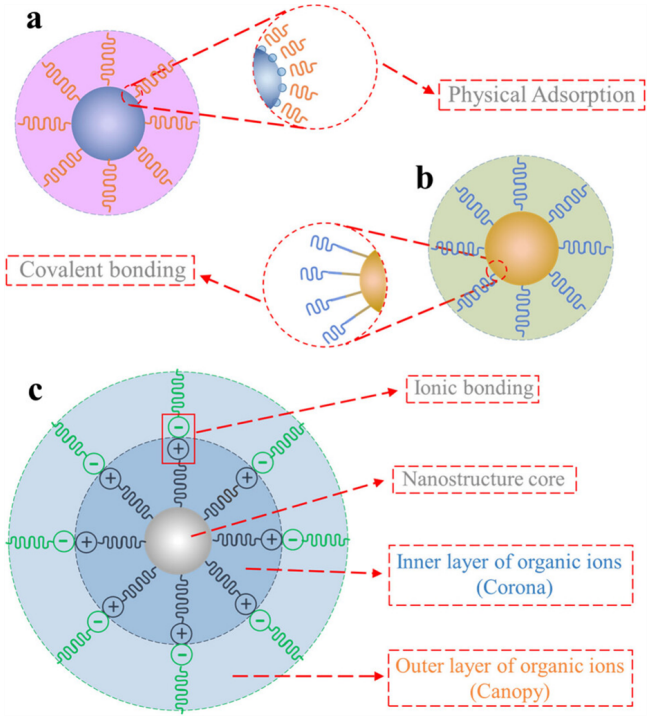

Figure 1.18: The structure of the solvent-free nanofluids[79]

The practical applications of SNFs span several industries. In energy storage, SNFs improve the efficiency of batteries and supercapacitors by enhancing conductivity and preventing nanoparticle clumping, which contributes to more reliable and efficient energy systems. As lubricants, SNFs reduce friction and wear in mechanical systems, thus extending the lifespan of machinery and improving operational efficiency. In thermal management, SNFs are used in heat transfer systems due to their superior thermal conductivity, making them valuable for cooling systems in electronics or energy-efficient thermal materials. SNFs also play a significant role in environmental applications, such as gas capture and separation, where they help capture and store gases like carbon dioxide. Furthermore, their ability to enhance the strength and thermal properties of polymer composites makes SNFs useful

in advanced coatings, structural materials, and electronic devices (Figure 1.19).[79]

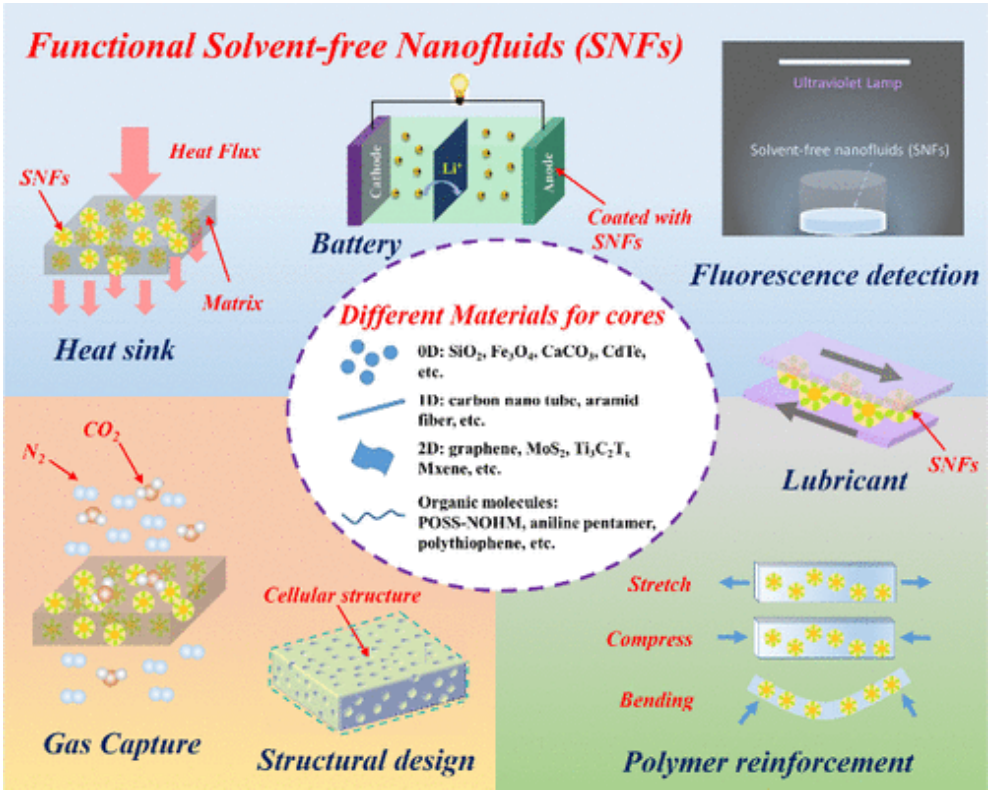

Figure 1.19: Functional Solvent-free Nanofluids application[79]

One of the pioneering studies introducing this concept was conducted by Athanasios B. Bourlinos.[80, 81] His research focuses on the surface functionalization of nanoparticles such as SiO_2 and γ-Fe_2O_3 with large organic counterions, like sulfonates, to create materials that behave as viscous fluids at room temperature, despite being composed of solid nanoparticles (Figure 1.20). These functional nanofluids hold potential applications in lubricants, coatings, and electronics, as their design reduces interparticle interactions, leading to improved stability and tunability. These materials exhibit liquid-

like behavior even under shear stress, making them ideal for dynamic applications where traditional nanoparticles may fail.

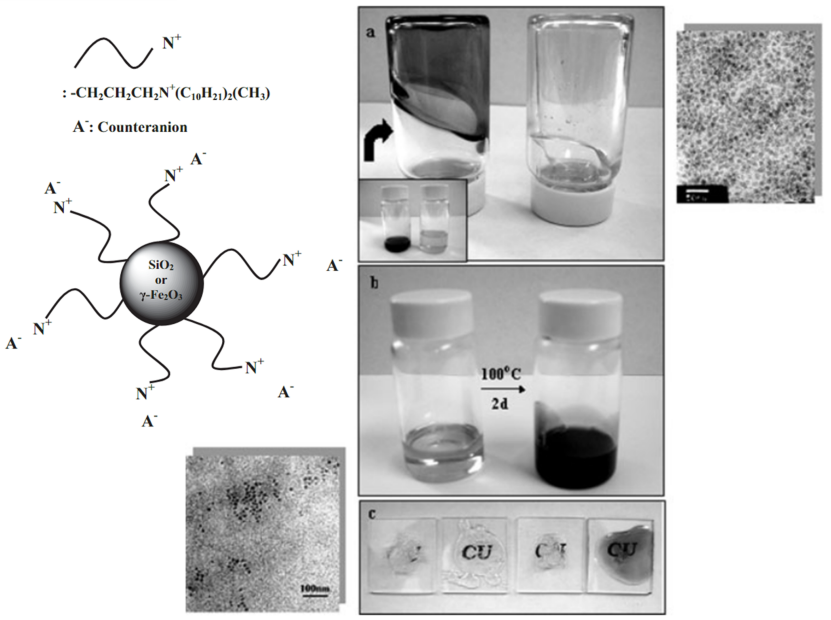

Figure 1.20: Schematic of the ionically modified nanoparticles and photos of the silica sulfonated nanosalt[80]

This work has laid a convincing foundation for using solvent-free ionic nanofluids (SNFs) across various applications. By adjusting the core, corona, and canopy structures, it is possible to obtain tunable properties, which can be further modified with or without the application of external stimuli. A notable example is the development of a multi-stimuli responsive nanofluid that exhibits reversible structural color changes in response to temperature and magnetic fields. Using Poly(N-isopropyl acrylamide) (PNIPAM), a thermoresponsive polymer, and superparamagnetic nanoparticles, the nanofluid's interdroplet spacing can be controlled by temperature, while its optical properties can be tuned under a magnetic field. Adding SDS surfactant enhances

its thermo-magnetic responsiveness, increasing both stability and tunability. This system holds potential for applications in optical devices, smart drug delivery, and temperature sensors.[82]

1.4.2.1 Thermoresponsive SNFs for application as smart lubricants

Among the various applications of stimuli-responsive SNFs, the development of thermoresponsive smart lubricants has gained significant attention. With increasing energy consumption and wear-related failures in mechanical systems, minimizing friction and wear is crucial for energy efficiency and sustainability. Conventional lubricants, typically consisting of base oils and additives like zinc dialkyldithiophosphate (ZDDP), provide friction-reduction and anti-wear benefits but face challenges such as poor dispersion stability and limited performance under extreme conditions.[83, 84] While nanoparticles (NPs) and ionic liquids (ILs) offer some improvements, they still encounter issues like NP agglomeration and the need for solvents in some ILs.

Nanofluids (NFs) represent a major innovation in lubrication technology. Even under extreme conditions, they provide solvent-free, stable dispersions with enhanced tribological performance. Combining a nanoparticle core with an ionic corona gives NFs superior load-carrying capacity and promotes the formation of tribofilms, which protect surfaces and reduce wear.[85] Developing of task-specific lubricants that respond to external stimuli, such as light, electricity, and heat, offers exciting potential for achieving "smart lubrication" in energy-efficient systems, especially in intelligent and automated machinery. These advantages make NFs highly suitable for modern lubrica-

tion systems, surpassing the limitations of traditional lubricants by offering improved performance, adaptability, and sustainability.

A significant study done by Guo et al[86], explores the synthesis, characterization, and application of solvent-free ionic silica nanofluids (NFs) as innovative lubricants (Figure 1.21). The study highlights their smart lubrication properties, particularly their ability to reduce friction and wear under an external electrical field. The nanofluids are made by grafting ionic corona and canopy layers onto silica nanoparticles (SiO_2), enhancing dispersion stability and fluidity at room temperature. The research examines four types of silica NFs with varying corona chain lengths and analyzes their tribological performance, including their friction-reduction and wear-prevention properties. The longer corona chains result in better lubrication performance due to thicker organic-inorganic hybrid layers forming at the friction interface.

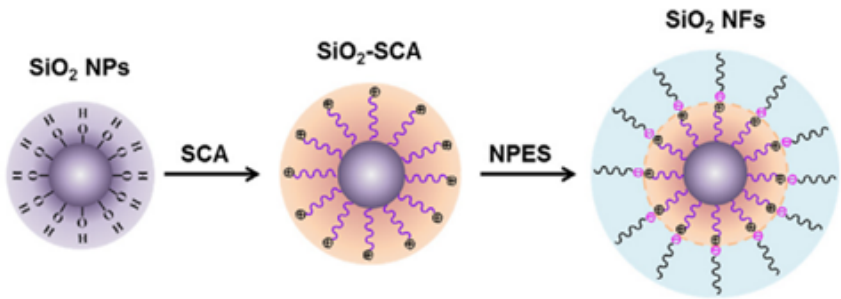

Figure 1.21: Schematic illustration of the synthesis routes of SNFs[86]

One critical aspect not addressed in this paper, but highly relevant in the context of lubricants, is thermo-responsive properties. Friction naturally generates heat, and the spatial arrangement of canopy chains in the nanofluid is strongly influenced by temperature. Since this study highlights that the

lubrication performance is dependent on the thickness of the hybrid inter-chain layer, it follows that the properties of the lubricant could also be modulated by temperature.[87]

Nonetheless, this work envisages the possibility of using of silica-based SNFs to develop of smart lubricants. In particular, by modifying the core (for example, exploring the influence of anisotropic nanoparticles such as sepiolite), as well as the corona and canopy (by testing different ionic units that may generate stronger ionic bonds), the final properties of the lubricants can be fine-tuned to further improve performance. These adjustments could enhance thermal stability and make the materials more adaptable to extreme conditions. Additionally, exploring more cost-effective synthesis methods would increase their practical viability for large-scale applications.

1.5 Aim of the thesis

Given this background, the aim of this thesis is to develop and optimize filler materials with stimuli-responsive properties, particularly photo- and thermoresponsive properties, for use in smart composites.

In this context, silica nanoparticles and sepiolite nanofibers provide a versatile platform for functionalization with stimuli-responsive units. The presence of hydroxyl groups on the large surface area of these fillers allows for the anchoring of molecules with specific functionalities, such as cinnamic and coumarin groups, which enable light-induced reversible crosslinking when incorporated into a suitably modified polymer matrix.

Additionally, guanidinium-based ionic groups can be grafted onto the filler surface, creating strong ionic interactions with sulfonated polymer chains that undergo structural rearrangement depending on the input temperature.
bigskip By integrating these systems, the thesis aims to promote the development of composites that dynamically respond to environmental changes while encouraging sustainable practices in materials design.

In the following sections, a brief description of the research activity will be provided according to the materials' stimuli-responsive features and final application.

Photoresponsive Nanocomposites for Smart Packaging

The first objective of the thesis is to develop materials capable of responding to specific wavelengths of light, which holds great promise for smart packaging applications. One of the most attractive features of these pack-

aging materials is their ability to assemble, disassemble, or alter mechanical properties in response to light, enabling improved functionality such as self-healing, controlled degradation, or on-demand release of substances.

This part focuses on creating photoresponsive fillers, specifically silica nanoparticles and sepiolite nanofibers, functionalized with cinnamic or coumarin units. These units are well-known for their ability to undergo photoreversible $2\pi + 2\pi$ cycloaddition reactions under UV light, making them ideal candidates for materials requiring tunable properties. The reversible formation and cleavage of cyclobutane bonds allow for "on-demand" covalent crosslinking of the final nanocomposite when the functionalized fillers are incorporated into a polymer matrix suitably modified with the same units. Silica nanoparticles are chosen due to their high surface area, transparency, mechanical reinforcement capabilities, and thermal stability. Sepiolite nanofibers are selected for their fibrous morphology, enhancing the final material's elasticity and toughness. Both fillers have great compatibility with various polymers, including bio-based ones like starch and their functionalization with cinnamic units is described using two approaches. The first approach involves the synthesis of a novel alkoxysilane that covalently bears cinnamic units, which are used for the direct functionalization of the filler surface. The second approach is a two-step process. First, the filler surface is modified with a compatibilizing agent, which prepares the surface for further functionalization. In the second step, cinnamic units are grafted onto the modified surface. Both strategies are explored and compared to determine the most effective approach for achieving optimal photoresponsive behavior in smart nanocomposites.

Starch is chosen as the polymer matrix due to its biodegradability, renewability, and cost-effectiveness. As a bio-based material, starch aligns with the thesis's sustainability goals, particularly for packaging applications, where reducing environmental impact is critical. Although commercially available starch has been used in this work, future plans will involve extracting starch from food waste, further promoting material revaluation and sustainability. Challenges of starch, such as high hydrophilicity, low mechanical strength, and thermal instability, are addressed by incorporating cinnamic units to facilitate cross-linking. This enhancement is expected to improve the mechanical properties and water resistance of the final material. By integrating photoresponsive fillers into the starch matrix, this thesis aims to produce a preliminary smart nanocomposite with tunable film-forming capabilities, making it suitable for various packaging applications. Incorporating cinnamic units will potentially lead to materials with enhanced durability and controlled degradation, offering significant advantages to industries looking for sustainable, smart packaging solutions. In addition to cinnamic units, coumarin-based photoresponsive fillers are also be explored. Coumarin operates via a similar light-activated mechanism but undergoes photoreversible cycloaddition reactions at different wavelengths. Coumarin-functionalized silica nanoparticles are synthesized using a two-step process to achieve distinct photoresponsive behaviors that complement those of the cinnamic-based systems. By incorporating cinnamic or coumarin fillers into a biobased polymer matrix suitably modified with the same unit, the generation of nanocomposites exhibiting a wider range of light-activated properties have been demonstrated, envisaging their potential use for packaging applications that require adaptability and precision.

Thermoresponsive SNFs for application as smart lubricants

The second goal of the research activity is to develop and investigate thermoresponsive solvent-free nanofluids (SNFs) that exhibit liquid-like behavior without the need for traditional solvents. This aligns with the growing demand for environmentally sustainable and high-performance materials, particularly for applications such as smart lubricants. The project focuses on functionalizing silica nanoparticles and sepiolite nanofibers with guanidinium units, creating a system that can interact with sulfonated polyethylene glycol (sulfo-PEG) chains. The primary objective is to leverage strong ionic interactions at the polymer-nanofiller interface to enhance system stability and responsiveness under varying thermal conditions. The guanidinium functionalization of these nanoparticles is a central aspect of the research. Guanidinium groups, known for their strong basicity and resonance stabilization, form stable non-covalent complexes with anionic species. These interactions are particularly relevant in guanidinium-sulfonate complexes, characterized by their high affinity. The first phase of this work focuses on synthesizing an alkoxysilane containing the guanidinium unit and subsequently using it to functionalize silica nanoparticles and sepiolite nanofibers. After functionalizing the fillers, the research integrates them into a sulfo-PEG matrix to study how varying the polymer-to-filler ratio influences the thermal, structural, and dynamic properties of the resulting nanocomposites. The research also explores the thermoresponsive behavior of these solvent-free nanofluids, focusing on how the material's viscosity and transparency change with temperature. This thermoresponsive property holds significant potential for smart lubricant applications, where reducing friction and wear in mechanical systems is crucial.

In Conclusion, this research aims to push the boundaries of smart, responsive materials by combining the mechanical reinforcement properties of inorganic nanoparticles with the stimulus-responsive behavior of organic chains. This approach opens up new possibilities for industrial applications where material adaptability, responsiveness, and sustainability are essential.

1.6 Structure of the thesis

Chapter 2 focuses on developing light-responsive fillers using silica nanoparticles (SiO_2 NPs) and sepiolite nanofibers (Sep NFs). It begins with synthesizing of SiO_2 NPs via the Stöber method and the pretreatment of Sep NFs to improve their surface properties. A novel photo-responsive compound, cinnamyl alkoxysilane (CINN-APTES), is created using carbodiimide chemistry to act as a light-sensitive compatibilizing agent. The surface functionalization of SiO_2 NPs and Sep NFs is achieved through one-step and double-step methods, both of which are analyzed for their effectiveness, with a preliminary proof of functionalized fillers photoreversible properties. Additionally, the first attempts of functionalizing of SiO_2 NPs with a coumarin moiety, offering enhanced control of light-triggered reactions across different wavelengths, is reported.

Chapter 3 outlines the synthesis, characterization, and evaluation of a novel photo-responsive etherified starch derived from yuca starch, developed in collaboration with Dr. Simona Petroni and Prof. Laura Cipolla. The starch was modified via etherification with cinnamyl chloride to enhance its properties and introduce light-responsive features. Key experimental methods included etherification, degree of substitution (DS) analysis, film formation, and photoresponsive behaviour assessment.

Chapter 4 overviews the development and characterization of bio-nanocomposites made from starch and either sepiolite or silica nanoparticles. The aim is to create stimuli-responsive materials capable of assembling and disassembling under light, making them suitable for sustainable packaging applications. The first part (developed in collaboration with University of Trento) focuses

on preparing and characterizing of films composed of bare yuca starch and bare sepiolite to evaluate the interaction between these components. Based on this work, the second part presents a preliminary demonstration of the preparation of photoresponsive nanocomposites using silica nanoparticles functionalized with cinnamic units and yuca starch modified with cinnamic groups.

Chapter 5 focuses on the preparation and characterization of solvent-free nanofluids, developed during the research secondment at the Charles Gerhardt Institute in Montpellier (ICGM-CNRS). A guanidinium-based alkoxysilane was synthesized to functionalize silica nanoparticles and sepiolite nanofibers. Functionalized fillers are then incorporated into sulfonated low-molecular-weight polyethylene glycol (sulfo-PEG) at various loadings. The guanidinium-sulfonate ionic interaction plays a crucial role in enhancing the composite properties.

Chapter 6 provides a comprehensive and final summary of the thesis, reviewing all the key findings and results achieved throughout the research. Additionally, it discusses future perspectives, highlighting areas where further optimization is needed to enhance the material properties and performance, and outlines potential directions for continuing the research and development.

References

(1) Kickelbick, G. Hybrid Materials - Past, Present and Future. *Hybrid Materials* **2014**, *1*, DOI: 10.2478/hyma-2014-0001.

(2) Gu, H.; Liu, C.; Zhu, J.; Gu, J.; Wujcik, E. K.; Shao, L.; Wang, N.; Wei, H.; Scaffaro, R.; Zhang, J.; Guo, Z. Introducing advanced composites and hybrid materials. *Advanced Composites and Hybrid Materials* **2018**, *1*, 1–5, DOI: 10.1007/s42114-017-0017-y.

(3) Sanchez, C.; Belleville, P.; Popall, M.; Nicole, L. Applications of advanced hybrid organic-inorganic nanomaterials: from laboratory to market. *Chemical Society Reviews* **2011**, *40*, 696–753, DOI: 10.1039/C0CS00136H.

(4) Lakkad, S.; Patel, J. Mechanical properties of bamboo, a natural composite. *Fibre Science and Technology* **1981**, *14*, 319–322, DOI: 10.1016/0015-0568(81)90023-3.

(5) Ahmad, Z.; Mark, J. E. Biomimetic materials: recent developments in organic-inorganic hybrids. *Materials Science and Engineering: C* **1998**, *6*, 183–196, DOI: 10.1016/S0928-4931(98)00044-7.

(6) Rosa, N.; Moura, M. F. S. F.; Olhero, S.; Simoes, R.; Magalhães, F. D.; Marques, A. T.; Ferreira, J. P. S.; Reis, A. R.; Carvalho, M.; Parente, M. Bone: An Outstanding Composite Material. *Applied Sciences* **2022**, *12*, 3381, DOI: 10.3390/app12073381.

(7) Jose-Yacaman, M.; Rendon, L.; Arenas, J.; Serra Puche MC, n. Maya Blue Paint: An Ancient Nanostructured Material. *Science (New York, N.Y.)* **1996**, *273*, 223–225, DOI: 10.1126/science.273.5272.223.

(8) Van Olphen, H. Maya blue: a clay-organic pigment? *Science (New York, N.Y.)* **1966**, *154*, 645–646, DOI: 10.1126/science.154.3749.645.

(9) Gómez-Romero, P.; Sanchez, C. Hybrid materials. Functional properties. From Maya Blue to 21st century materials. *New Journal of Chemistry* **2005**, *29*, 57–58, DOI: 10.1039/B416075B.

(10) Kickelbick, G. In *Hybrid Materials*; John Wiley & Sons, Ltd: 2006, pp 1–48, DOI: 10.1002/9783527610495.ch1.

(11) Judeinstein, P.; Sanchez, C. Hybrid organic-inorganic materials: a land of multidisciplinarity. *Journal of Materials Chemistry* **1996**, *6*, 511–525, DOI: 10.1039/JM9960600511.

(12) Luna, J.; Vílchez, A. In *Emerging Nanotchnologies in Food Science*, Busquets, R., Ed.; Micro and Nano Technologies; Elsevier: Boston, 2017, pp 119–147, DOI: 10.1016/B978-0-323-42980-1.00007-8.

(13) Akpan, E. I.; Shen, X.; Wetzel, B.; Friedrich, K. In *Polymer Composites with Functionalized Nanoparticles*, Pielichowski, K., Majka, T. M., Eds.; Micro and Nano Technologies; Elsevier: 2019, pp 47–83, DOI: 10.1016/B978-0-12-814064-2.00002-0.

(14) Caseri, W. In *Hybrid Materials*; John Wiley & Sons, Ltd: 2006, pp 49–86, DOI: 10.1002/9783527610495.ch2.

(15) Cui, Y.; Kundalwal, S. I.; Kumar, S. Gas barrier performance of graphene/polymer nanocomposites. *Carbon* **2016**, *98*, 313–333, DOI: 10.1016/j.carbon.2015.11.018.

(16) D'Arienzo, M.; Diré, S.; Masneri, V.; Rovera, D.; Di Credico, B.; Callone, E.; Mascotto, S.; Pegoretti, A.; Ziarelli, F.; Scotti, R. Tailoring the Dielectric and Mechanical Properties of Polybutadiene Nanocomposites by Using Designed Ladder-like Polysilsesquioxanes. *ACS Applied Nano Materials* **2018**, *1*, 3817–3828, DOI: 10.1021/acsanm.8b00558.

(17) D'Arienzo, M.; Dirè, S.; Cobani, E.; Orsini, S.; Di Credico, B.; Antonini, C.; Callone, E.; Parrino, F.; Dalle Vacche, S.; Trusiano, G.; Bongiovanni, R.; Scotti, R. SiO2/Ladder-Like Polysilsesquioxanes Nanocomposite Coatings: Playing with the Hybrid Interface for Tuning Thermal Properties and Wettability. *Coatings* **2020**, *10*, 913, DOI: 10.3390/coatings10100913.

(18) Rajesh; Ahuja, T.; Kumar, D. Recent progress in the development of nano-structured conducting polymers/nanocomposites for sensor applications. *Sensors and Actuators B: Chemical* **2009**, *136*, 275–286, DOI: 10.1016/j.snb.2008.09.014.

(19) Chow, W. S.; Mohd Ishak, Z. A. Smart polymer nanocomposites: A review. | EBSCOhost.

(20) Vengatesan, M. R.; Mittal, V. In *Spherical and Fibrous Filler Composites*; John Wiley & Sons, Ltd: 2016, pp 1–38, DOI: 10.1002/9783527670222.ch1.

(21) Bhattacharya, M. Polymer Nanocomposites—A Comparison between Carbon Nanotubes, Graphene, and Clay as Nanofillers. *Materials* **2016**, *9*, 262, DOI: 10.3390/ma9040262.

(22) Oliveira, A. D. d.; Beatrice, C. A. G.; Oliveira, A. D. d.; Beatrice, C. A. G. In *Nanocomposites - Recent Evolutions*; IntechOpen: 2018, DOI: 10.5772/intechopen.81329.

(23) Isitman, N. A.; Dogan, M.; Bayramli, E.; Kaynak, C. The role of nanoparticle geometry in flame retardancy of polylactide nanocomposites containing aluminium phosphinate. *Polymer Degradation and Stability* **2012**, *97*, 1285–1296, DOI: 10.1016/j.polymdegradstab.2012.05.028.

(24) Ijaz, I.; Gilani, E.; Nazir, A.; Bukhari, A. Detail review on chemical, physical and green synthesis, classification, characterizations and applications of nanoparticles. *Green Chemistry Letters and Reviews* **2020**, *13*, 223–245, DOI: 10.1080/17518253.2020.1802517.

(25) Fambri, L.; Dabrowska, I.; Ceccato, R.; Pegoretti, A. Effects of Fumed Silica and Draw Ratio on Nanocomposite Polypropylene Fibers. *Polymers* **2017**, *9*, 41, DOI: 10.3390/polym9020041.

(26) Ślosarczyk, A.; Barełkowski, M.; Niemier, S.; Jakubowska, P. Synthesis and characterisation of silica aerogel/carbon microfibers nanocomposites dried in supercritical and ambient pressure conditions. *Journal of Sol-Gel Science and Technology* **2015**, *76*, 227–232, DOI: 10.1007/s10971-015-3798-x.

(27) D'Amato, M.; Dorigato, A.; Fambri, L.; Pegoretti, A. High performance polyethylene nanocomposite fibers. *Express Polymer Letters* **2012**, *6*, 954–964, DOI: 10.3144/expresspolymlett.2012.101.

(28) Gupta, P.; Bera, M.; Maji, P. K. Nanotailoring of sepiolite clay with poly [styrene-b-(ethylene-co-butylene)-b-styrene]: structure-property

correlation. *Polymers for Advanced Technologies* **2017**, *28*, 1428–1437, DOI: 10.1002/pat.4019.

(29) Bilotti, E.; Fischer, H. R.; Peijs, T. Polymer nanocomposites based on needle-like sepiolite clays: Effect of functionalized polymers on the dispersion of nanofiller, crystallinity, and mechanical properties. *Journal of Applied Polymer Science* **2008**, *107*, 1116–1123, DOI: 10.1002/app.25395.

(30) Lu, J.; Yan, S.; Song, W.; Jacob, K. I.; Xiao, R. Construction and characterization of versatile flexible composite nanofibrous aerogels based on thermoplastic polymeric nanofibers. *Journal of Materials Science* **2020**, *55*, 8155–8169, DOI: 10.1007/s10853-020-04400-4.

(31) Messersmith, P. B.; Giannelis, E. P. Synthesis and barrier properties of poly(ε-caprolactone)-layered silicate nanocomposites. *Journal of Polymer Science Part A: Polymer Chemistry* **1995**, *33*, 1047–1057, DOI: 10.1002/pola.1995.080330707.

(32) Sonnier, R.; Saout, G. L.; Otazaghine, B.; Vahabi, H.; Lopez-Cuesta, J.-M. Nanocomposites of polypropylene/polyamide 6 blends based on three different nanoclays: thermal stability and flame retardancy. *International Journal of Advanced and Integrated Medical Sciences* **2012**, *T. 58, nr 5*, DOI: 10.14314/polimery.2013.350.

(33) Gun'ko, V. M. In *Polymer Composites with Functionalized Nanoparticles*, Pielichowski, K., Majka, T. M., Eds.; Micro and Nano Technologies; Elsevier: 2019, pp 119–148, DOI: 10.1016/B978-0-12-814064-2.00004-4.

(34) Majka, T. M.; Pielichowski, K. In *Polymer Composites with Functionalized Nanoparticles*, Pielichowski, K., Majka, T. M., Eds.; Micro and Nano Technologies; Elsevier: 2019, pp 149–178, DOI: 10.1016/B978-0-12-814064-2.00005-6.

(35) Rahman, I. A.; Padavettan, V. Synthesis of Silica Nanoparticles by Sol-Gel: Size-Dependent Properties, Surface Modification, and Applications in Silica-Polymer Nanocomposites—A Review. *Journal of Nanomaterials* **2012**, *2012*, 132424, DOI: 10.1155/2012/132424.

(36) Vansant, E. F.; Voort, P. V. D.; Vrancken, K. C., *Characterization and Chemical Modification of the Silica Surface*; Elsevier: 1995; 573 pp.

(37) Navrotsky, A. In *Silica*, Heaney, P. J., Prewitt, C. T., Gibbs, G. V., Eds.; De Gruyter: 1994, pp 309–330, DOI: 10.1515/9781501509698-014.

(38) Stöber, W.; Fink, A.; Bohn, E. Controlled growth of monodisperse silica spheres in the micron size range. *Journal of Colloid and Interface Science* **1968**, *26*, 62–69, DOI: 10.1016/0021-9797(68)90272-5.

(39) Lee, D. W.; Yoo, B. R. Advanced silica/polymer composites: Materials and applications. *Journal of Industrial and Engineering Chemistry* **2016**, *38*, 1–12, DOI: 10.1016/j.jiec.2016.04.016.

(40) Okada, A.; Kawasumi, M.; Usuki, A.; Kojima, Y.; Kurauchi, T.; Kamigaito, O. Nylon 6-Clay Hybrid. *MRS Online Proceedings Library* **1989**, *171*, 45–50, DOI: 10.1557/PROC-171-45.

(41) Ahmadi, S. J.; Huang, Y. D.; Li, W. Synthetic routes, properties and future applications of polymer-layered silicate nanocomposites. *Jour-*

nal of Materials Science **2004**, *39*, 1919–1925, DOI: 10.1023/B:JMSC.0000017753.90222.96.

(42) Giannelis, E. P. Polymer-layered silicate nanocomposites: Synthesis, properties and applications. *Applied Organometallic Chemistry* **1998**, *12*, 675–680, DOI: 10.1002/(SICI)1099-0739(199810/11)12:10/11<675::AID-AOC779>3.0.CO;2-V.

(43) Uddin, F. Clays, Nanoclays, and Montmorillonite Minerals. *Metallurgical and Materials Transactions A* **2008**, *39*, 2804–2814, DOI: 10.1007/s11661-008-9603-5.

(44) Rao; Pochan, J. M. Mechanics of Polymer-Clay Nanocomposites. *Macromolecules* **2007**, *40*, 290–296, DOI: 10.1021/ma061445w.

(45) Leszczyńska, A.; Njuguna, J.; Pielichowski, K.; Banerjee, J. R. Polymer/montmorillonite nanocomposites with improved thermal properties: Part I. Factors influencing thermal stability and mechanisms of thermal stability improvement. *Thermochimica Acta* **2007**, *453*, 75–96, DOI: 10.1016/j.tca.2006.11.002.

(46) Cui, Y.; Kumar, S.; Rao Kona, B.; Van Houcke, D. Gas barrier properties of polymer/clay nanocomposites. *RSC Advances* **2015**, *5*, 63669–63690, DOI: 10.1039/C5RA10333A.

(47) Avella, M.; De Vlieger, J. J.; Errico, M. E.; Fischer, S.; Vacca, P.; Volpe, M. G. Biodegradable starch/clay nanocomposite films for food packaging applications. *Food Chemistry* **2005**, *93*, 467–474, DOI: 10.1016/j.foodchem.2004.10.024.

(48) Kotal, M.; Bhowmick, A. K. Polymer nanocomposites from modified clays: Recent advances and challenges. *Progress in Polymer Science* **2015**, *51*, 127–187, DOI: 10.1016/j.progpolymsci.2015.10.001.

(49) Alvarez, A. In *Developments in Sedimentology*; Elsevier: 1984; Vol. 37, pp 253–287, DOI: 10.1016/S0070-4571(08)70044-X.

(50) Walczyk, A.; Karcz, R.; KryŚciak-Czerwenka, J.; Napruszewska, B. D.; Duraczyńska, D.; Michalik, A.; Olejniczak, Z.; Tomczyk, A.; Klimek, A.; Bahranowski, K.; Serwicka, E. M. Influence of Dry Milling on Phase Transformation of Sepiolite upon Alkali Activation: Implications for Textural, Catalytic and Sorptive Properties. *Materials* **2020**, *13*, 3936, DOI: 10.3390/ma13183936.

(51) Takei, T.; Oda, R.; Miura, A.; Kumada, N.; Kinomura, N.; Ohki, R.; Koshiyama, H. Effect of dispersion of sepiolite in sepiolite-NBR composite on the tensile strength. *Composites Part B: Engineering* **2013**, *44*, 260–265, DOI: 10.1016/j.compositesb.2012.05.034.

(52) Di Credico, B.; Cobani, E.; Callone, E.; Conzatti, L.; Cristofori, D.; D'Arienzo, M.; Dirè, S.; Giannini, L.; Hanel, T.; Scotti, R.; Stagnaro, P.; Tadiello, L.; Morazzoni, F. Size-controlled self-assembly of anisotropic sepiolite fibers in rubber nanocomposites. *Applied Clay Science* **2018**, *152*, 51–64, DOI: 10.1016/j.clay.2017.10.032.

(53) Olivato, J. B.; Marini, J.; Yamashita, F.; Pollet, E.; Grossmann, M. V. E.; Avérous, L. Sepiolite as a promising nanoclay for nano-biocomposites based on starch and biodegradable polyester. *Materials Science and Engineering: C* **2017**, *70*, 296–302, DOI: 10.1016/j.msec.2016.08.077.

(54) De la Caillerie, J. B. d.; Fripiat, J. J. AL modified sepiolite as catalyst or catalyst support. *Catalysis Today* **1992**, *14*, 125–140, DOI: 10.1016/0920-5861(92)80017-H.

(55) Song, N.; Hursthouse, A.; McLellan, I.; Wang, Z. Treatment of environmental contamination using sepiolite: current approaches and future potential. *Environmental Geochemistry and Health* **2021**, *43*, 2679–2697, DOI: 10.1007/s10653-020-00705-0.

(56) Pujari, S. P.; Scheres, L.; Marcelis, A. T. M.; Zuilhof, H. Covalent Surface Modification of Oxide Surfaces. *Angewandte Chemie International Edition* **2014**, *53*, 6322–6356, DOI: 10.1002/anie.201306709.

(57) Dhaffouli, A.; Salazar-Carballo, P. A.; Carinelli, S.; Holzinger, M.; Barhoumi, H. Improved electrochemical sensor using functionalized silica nanoparticles (SiO2-APTES) for high selectivity detection of lead ions. *Materials Chemistry and Physics* **2024**, *318*, 129253, DOI: 10.1016/j.matchemphys.2024.129253.

(58) D'Arienzo, M.; Redaelli, M.; Callone, E.; Conzatti, L.; Di Credico, B.; Dirè, S.; Giannini, L.; Polizzi, S.; Schizzi, I.; Scotti, R.; Tadiello, L.; Franca, M. Hybrid SiO2@POSS nanofiller: A promising reinforcing system for rubber nanocomposites. *Mater. Chem. Front.* **2017**, *1*, DOI: 10.1039/C7QM00045F.

(59) Salgado, C.; Arrieta, M. P.; Peponi, L.; López, D.; Fernández-García, M. Photo-crosslinkable polyurethanes reinforced with coumarin modified silica nanoparticles for photo-responsive coatings. *Progress in Organic Coatings* **2018**, *123*, 63–74, DOI: 10.1016/j.porgcoat.2018.06.019.

(60) Jr, W. B. S.; Sirkis, J. S.; Gardiner, P. T. Smart materials and structures: what are they? *Smart Materials and Structures* **1996**, *5*, 247, DOI: 10.1088/0964-1726/5/3/002.

(61) Rogers, C. A. Intelligent Material Systems — The Dawn of a New Materials Age. *Journal of Intelligent Material Systems and Structures* **1993**, *4*, 4–12, DOI: 10.1177/1045389X9300400102.

(62) Kaushal, A.; Vardhan, A.; Rawat, R. Intelligent Material For Modern Age : A Review.

(63) *Mechanical engineers' handbook*, 3rd ed; Kutz, M., Ed.; Wiley: Hoboken, N.J, 2006, 4 pp.

(64) Sauchelli, M. Smart materials explained, Ongreening - Green Building made easier and more accessible to all. https://ongreening.com/smart-materials-explained/.

(65) Ercole, F.; Davis, T. P.; Evans, R. A. Photo-responsive systems and biomaterials: photochromic polymers, light-triggered self-assembly, surface modification, fluorescence modulation and beyond. *Polymer Chemistry* **2010**, *1*, 37–54, DOI: 10.1039/B9PY00300B.

(66) Bongiovanni, R.; Vacche, S. D.; Vitale, A. Photoinduced Processes as a Way to Sustainable Polymers and Innovation in Polymeric Materials. *Polymers* **2021**, *13*, 2293, DOI: 10.3390/polym13142293.

(67) Liu, N.; Chen, Z.; Dunphy, D. R.; Jiang, Y.-B.; Assink, R. A.; Brinker, C. J. Photoresponsive Nanocomposite Formed by Self-Assembly of an Azobenzene-Modified Silane. *Angewandte Chemie International Edition* **2003**, *42*, 1731–1734, DOI: 10.1002/anie.200250189.

(68) Abdallh, M.; Yoshikawa, C.; Hearn, M. T. W.; Simon, G. P.; Saito, K. Photoreversible Smart Polymers Based on $2\pi + 2\pi$ Cycloaddition Reactions: Nanofilms to Self-Healing Films. *Macromolecules* **2019**, *52*, 2446–2455, DOI: 10.1021/acs.macromol.8b01729.

(69) Bazin, A.; Duval, A.; Avérous, L.; Pollet, E. Synthesis of Bio-Based Photo-Cross-Linkable Polyesters Based on Caffeic Acid through Selective Lipase-Catalyzed Polymerization. *Macromolecules* **2022**, *55*, 4256–4267, DOI: 10.1021/acs.macromol.2c00499.

(70) Zhang, Z.; Sèbe, G.; Wang, X.; Tam, K. C. UV-Absorbing Cellulose Nanocrystals as Functional Reinforcing Fillers in Poly(vinyl chloride) Films. *ACS Applied Nano Materials* **2018**, *1*, 632–641, DOI: 10.1021/acsanm.7b00126.

(71) Roy, P. S.; Mention, M. M.; Turner, M. A. P.; Brunissen, F.; Stavros, V. G.; Garnier, G.; Allais, F.; Saito, K. Bio-based photo-reversible self-healing polymer designed from lignin. *Green Chemistry* **2021**, *23*, 10050–10061, DOI: 10.1039/D1GC02957F.

(72) Kaur, G.; Johnston, P.; Saito, K. Photo-reversible dimerisation reactions and their applications in polymeric systems. *Polymer Chemistry* **2014**, *5*, 2171–2186, DOI: 10.1039/C3PY01234D.

(73) Abdallh, M.; He, P.; Hearn, M. T. W.; Simon, G. P.; Saito, K. Light-Switchable Self-Healing Dynamic Linear Polymers: Reversible Cycloaddition Reactions of Thymine-Containing Units. *ChemPlusChem* **2019**, *84*, 333–337, DOI: 10.1002/cplu.201900079.

(74) Sova, M. Antioxidant and Antimicrobial Activities of Cinnamic Acid Derivatives. *Mini-Reviews in Medicinal Chemistry* **2012**, *12*, 749–767, DOI: 10.2174/138955712801264792.

(75) Jain, P. K.; Joshi, H. Coumarin: Chemical and Pharmacological Profile. *Journal of Applied Pharmaceutical Science*.

(76) Mal, N. K.; Fujiwara, M.; Tanaka, Y.; Taguchi, T.; Matsukata, M. Photo-Switched Storage and Release of Guest Molecules in the Pore Void of Coumarin-Modified MCM-41. *Chemistry of Materials* **2003**, *15*, 3385–3394, DOI: 10.1021/cm0343296.

(77) Yudeng, W.; Yao, D.; Zheng, Y. A review on synthesis and application of solvent-free nanofluids. *Advanced Composites and Hybrid Materials* **2019**, *2*, DOI: 10.1007/s42114-019-00125-4.

(78) Liu, J.; Wang, X.; Liu, Y.; Liu, X.; Fan, K. Bioinspired three-dimensional and multiple adsorption effects toward high lubricity of solvent-free graphene-based nanofluid. *Carbon* **2021**, *188*, DOI: 10.1016/j.carbon.2021.11.065.

(79) Liu, M.; Qin, H.; Chen, Y.; Lu, Y.; Song, Y.; Gao, Z.; Xiong, C.; Liu, F. Recent Progress of Functional Solvent-free Nanofluids: A Review. *ACS Applied Materials & Interfaces* **2024**, *16*, 41766–41787, DOI: 10.1021/acsami.4c08256.

(80) Bourlinos, A. B.; Herrera, R.; Chalkias, N.; Jiang, D. D.; Zhang, Q.; Archer, L. A.; Giannelis, E. P. Surface-Functionalized Nanoparticles with Liquid-Like Behavior. *Advanced Materials* **2005**, *17*, 234–237, DOI: 10.1002/adma.200401060.

(81) Bourlinos, A. B.; Giannelis, E. P.; Zhang, Q.; Archer, L. A.; Floudas, G.; Fytas, G. Surface-functionalized nanoparticles with liquid-like behavior: The role of the constituent components. *The European Physical Journal E* **2006**, *20*, 109–117, DOI: 10.1140/epje/i2006-10007-3.

(82) Zaibudeen, A. W.; Philip, J. Multi-stimuli responsive nanofluid with easy-to-visualize structural color patterns. *Colloids and Surfaces A: Physicochemical and Engineering Aspects* **2017**, *518*, 98–108, DOI: 10.1016/j.colsurfa.2017.01.015.

(83) Erdemir, A.; Ramirez, G.; Eryilmaz, O. L.; Narayanan, B.; Liao, Y.; Kamath, G.; Sankaranarayanan, S. K. R. S. Carbon-based tribofilms from lubricating oils. *Nature* **2016**, *536*, 67–71, DOI: 10.1038/nature18948.

(84) Qu, J.; Barnhill, W. C.; Luo, H.; Meyer III, H. M.; Leonard, D. N.; Landauer, A. K.; Kheireddin, B.; Gao, H.; Papke, B. L.; Dai, S. Synergistic Effects Between Phosphonium-Alkylphosphate Ionic Liquids and Zinc Dialkyldithiophosphate (ZDDP) as Lubricant Additives. *Advanced Materials* **2015**, *27*, 4767–4774, DOI: 10.1002/adma.201502037.

(85) Guo, Y.; Zhang, L.; Zhao, F.; Li, G.; Zhang, G. Tribological behaviors of novel epoxy nanocomposites filled with solvent-free ionic SiO2 nanofluids. *Composites Part B: Engineering* **2021**, *215*, 108751, DOI: 10.1016/j.compositesb.2021.108751.

(86) Guo, Y.; Liu, G.; Li, G.; Zhao, F.; Zhang, L.; Guo, F.; Zhang, G. Solvent-free ionic silica nanofluids: Smart lubrication materials ex-

hibiting remarkable responsiveness to weak electrical stimuli. *Chemical Engineering Journal* **2020**, *383*, 123202, DOI: 10.1016/j.cej.2019.123202.

(87) Moghaddam, S. Z.; Thormann, E. Surface forces and friction tuned by thermo-responsive polymer films. *Current Opinion in Colloid & Interface Science* **2020**, *47*, 27–45, DOI: 10.1016/j.cocis.2019.12.002.

Chapter 2

Preparation of light-responsive fillers

This chapter provides a comprehensively overviews of the materials, synthesis procedures, and characterization techniques used to develop novel light-responsive fillers with potential eco-friendly applications. The goal is to utilize natural clays, specifically sepiolite nanofibers (Sep NFs), as sustainable fillers to minimize environmental impact. Given their wide use as reinforcement materials in various applications, a model system involving silica nanoparticles (SiO_2 NPs) was also examined, as a preliminary step.

The chapter is divided into four sections. **Section 2.1** presents the synthesis of SiO_2 NPs using the Stöber method, known for producing well-defined and uniform silica spheres, as well as the basic pretreatment of Sep NFs to enhance surface hydroxyl groups and disaggregate the nanofibers. **Section 2.2** details the synthesis of a novel cinnamyl alkoxysilane (CINN-APTES) using carbodiimide chemistry, which allows the covalent attachment of cinnamic acid units to the fillers, thereby introducing photo-responsive functionalities. **Section 2.3** focuses on the surface functionalization of SiO_2 NPs and Sep NFs to achieve photo-responsive fillers. Two different strategies were employed: a one-step functionalization using CINN-APTES and a double-step method involving modification of pre-grafted APTES groups on the filler surface using cinnamic derivatives (CINN-NHS or CNCOCl). The advantages and disadvantages of both strategies are discussed, with an emphasis on their effectiveness. Additionally, the DRS characterization of the functionalized fillers is described, highlighting their photoreversible properties upon UV irradiation. Finally, **section 2.4** presents a preliminary attempt to explore using another type of photoresponsive unit: the coumarin moiety. Cinnamic acid has an absorption maximum of around 277 nm, whereas coumarin absorbs at approximately 330 nm. This difference in absorption

wavelengths provides different control over the direct reactions in coumarin-based systems. In both cases, the cleavage of the cyclobutane bond occurs at 254 nm. This section investigates the initial functionalization of silica nanoparticles with the coumarin unit.

2.1 Preparation of naked fillers

2.1.1 Synthesis Stöber of SiO_2 NPs

Stöber's method[1] is a well-known technique for synthesizing colloidal silica particles, notable for its ability to produce well-defined, monodisperse, and uniform silica spheres. The method is highly versatile, allowing for easy adjustment of reaction parameters, such as reagent concentration and temperature, to control particle properties. The process is an ammonia-catalyzed sol-gel reaction in which tetraethylorthosilicate (TEOS) undergoes hydrolysis in the presence of water and low molecular weight alcohols, like ethanol, followed by condensation to form silica particles.[2, 3]

2.1.1.1 Experimental Procedure of SiO_2 NPs

Materials

Tetraethyl orthosilicate ≥99% (TEOS), Ammonia solution 25 wt.% (NH_3) and aqueous hydrochloric acid 37 wt.% (HCl) were purchased from Sigma-Aldrich. Ethanol ≥99.8% (EtOH) was purchased from Carlo Erba.

Synthesis

A two-neck round-bottom flask was charged with 50.0 mL of a 25 wt.% NH_3 solution and 1 L of EtOH. The solution was stirred magnetically at 300 rpm and heated to 60°C. Once the temperature reached 60°C, a solution of 25.0 mL of TEOS and 28.0 mL of EtOH was added dropwise to the reaction flask via a dropping funnel at approximately 1 mL/min. The reaction mixture was then stirred at 60°C for 20 hours. Following this, 20 mL of 2 M HCl was

added. The resulting product was isolated by centrifugation at 9000 rpm for 10 minutes and washed four times with EtOH. The final product was dried overnight in an oven at 80°C.

2.1.1.2 Characterization of SiO_2 NPs

TEM analysis

The morphological features of the SiO_2 NPs were examined using TEM microscopy. As shown in Figure 2.1, the TEM micrographs reveal nanospheres with a homogeneously distributed size. Specifically, the average diameter of the NPs is 30 ± 3 nm.

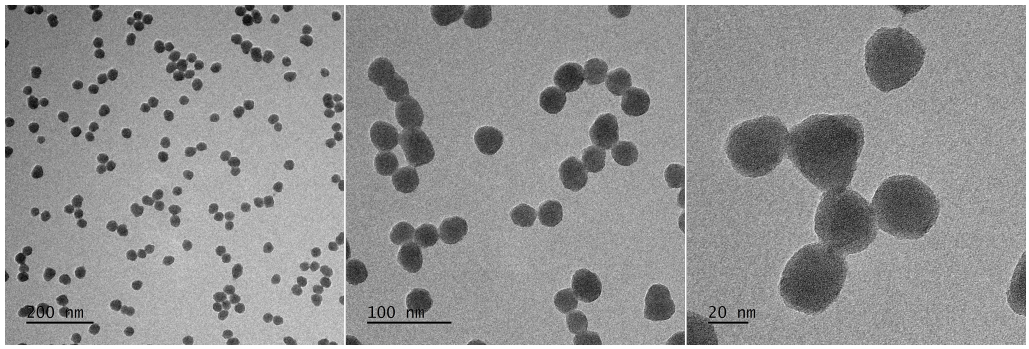

Figure 2.1: TEM micrographs of pristine SiO_2 NPs

Nitrogen physisorption

The nitrogen adsorption-desorption (77 K) isotherm was measured for SiO_2 nanoparticles (NPs). The isotherm (see Figure 2.2) is classified as a combination of type I and type IV (according to the IUPAC classification), indicating a microporous and mesoporous structure.[4] Consistent with the type I isotherm, the pore size distribution derived from the NLDFT model

(Figure 2.3) shows two main distributions characterized by mean half-pore widths of approximately 0.45 nm and 1.1 nm, both within the micropore range.

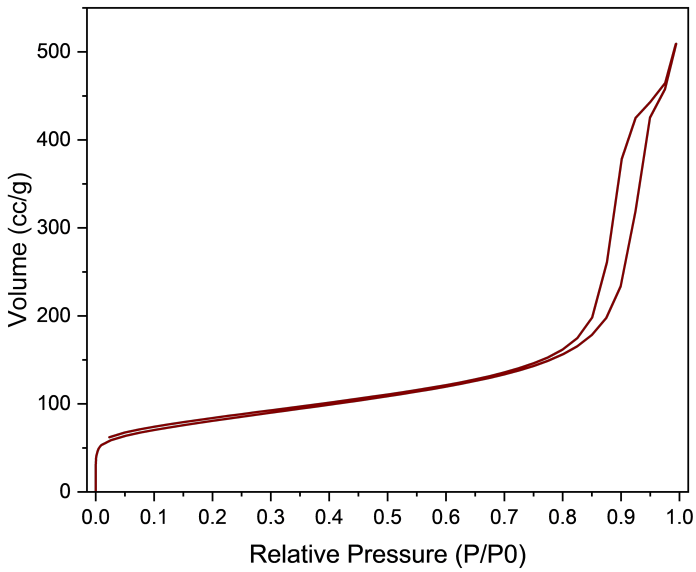

Figure 2.2: Nitrogen adsorption-desorption (77 K) isotherm of SiO_2 NPs

In the case of the type IV isotherm component, the pore size distribution derived from the BJH model, applied solely to the desorption curve, reveals a distribution centred around 9.6 nm in half-pore width (Figure 2.4). Given that TEM analysis shows the nanoparticles have a diameter of about 30 nm and no visible porous structure, it is unlikely that they contain pores measuring approximately 19.2 nm. This observation, along with the dramatic increase in adsorption volume at high relative pressures ($P/P0 > 0.8$), could be attributed to the filling of interparticle pores by nitrogen molecules, which is significant for samples with nanoscale external diameters.

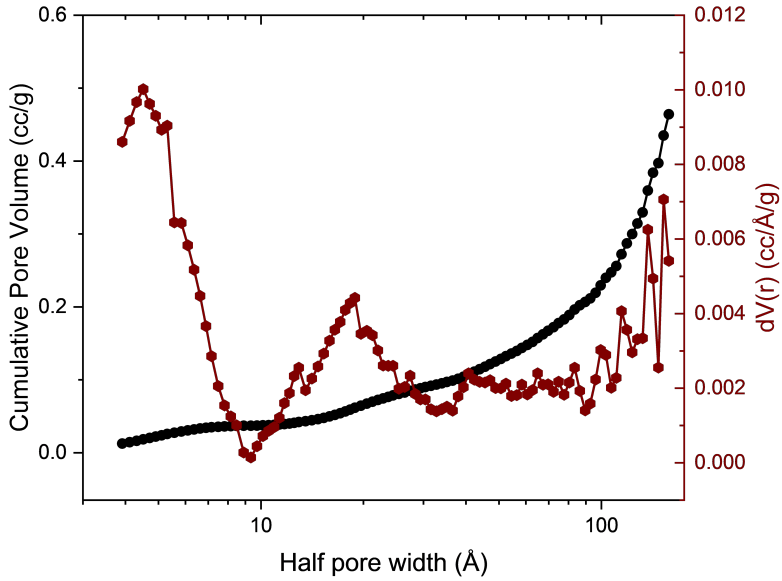

Figure 2.3: Cumulative pore volume and pore size distribution curves of SiO_2 NPs calculated by NLDFT model for microporous analysis

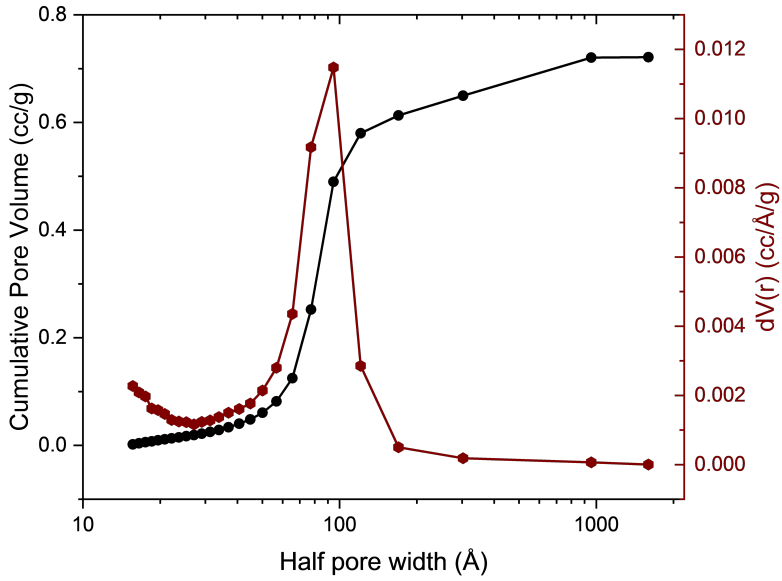

Figure 2.4: Cumulative pore volume and pore size distribution curves of SiO_2 NPs calculated by BJH model for mesoporous analysis

In other words, the mesoporous behavior observed in the type IV isotherm could be due to interparticle spaces formed by aggregation, suggesting that the nanoparticles may be present in aggregated form. The results of the gas adsorption analysis (based on BET and NLDFT models) indicate a BET surface area of 284.9 ± 0.6 m^2/g and a pore volume of 0.464 cc/g.

In other words, the mesoporous behavior observed in the type IV isotherm could be due to interparticle spaces formed by aggregation, suggesting that the nanoparticles may be present in aggregated form. The results of the gas adsorption analysis (based on BET and NLDFT models) indicate a BET surface area of 284.9 ± 0.6 m^2/g and a pore volume of 0.464 cc/g.

TGA

Thermogravimetric analysis (TGA) was employed to estimate the number of surface hydroxyl (OH_{sup}) groups on bare nanoparticles. The analysis specifically focused on the mass loss observed between 150°C and 1000°C, associated with the decomposition or desorption of surface-bound hydroxyl groups. The equations used to calculate the OH_{sup} content are provided in the appendix (Equation A.1 and Equation A.2) and considers the mass loss measured during the TGA and correlates it with the number of hydroxyl groups per unit area on the nanoparticle surface. The number of OH_{sup} groups was determined to be 13.67 n./nm^2.

2.1.2 Basic pretreatment of Sep NFs

Sepiolite, a naturally occurring fibrous magnesium silicate, is widely used across various industries due to its unique structural and surface properties.

Its microfibrous morphology, high surface area, and excellent adsorption capacity make it ideal for applications in fields such as water purification, environmental remediation, construction, and pharmaceuticals. Sepiolite is also highly valued in manufacturing adsorbents, catalysts, and nanocomposites. Key advantages of sepiolite include its low cost, environmental friendliness, and versatility in chemical modifications, allowing it to be tailored for specific uses.[5]

Basic pre-treatment of sepiolite using NaOH is necessary to increase surface hydroxyl groups and to disaggregate nanofibers without significantly damaging their structure. Sepiolite shows strong resistance to degradation during base treatment at room temperature, maintaining its shape and aspect ratio, making it a more effective and stable process compared to acid treatments.[6]

2.1.2.1 Experimental Procedure of SepOH NFs

Materials

Pristine Sepiolite (Sep), namely sepiolite Pangel S9, is a commercially available clay and, in particular, Sep used in this thesis was extracted from the landfill of Vallecas (Spain). Sodium hydroxide 98% (NaOH) was purchased from Thermo Fisher Scientific.

Synthesis

10.0 g of Sep was dispersed in 500 mL of 0.01 M NaOH, and the suspension was vigorously stirred at room temperature for 24 hours. The mixture was then centrifuged at 9000 rpm for 15 minutes, and the resulting product (SepOH NFs) was washed several times with deionized water until the pH of

the supernatant reached 7. The SepOH NFs were then dispersed in 100 mL of deionized water, and subsequently freeze-dried. The product yield was approximately 40%.

2.1.2.2 Characterization of SepOH NFs

TEM analysis

TEM analysis was conducted to study the morphology of Sepiolite. As shown in Fig.Figure 2.5, the TEM micrographs display the characteristic fibrous morphology of the phyllosilicate, with fibers slightly interconnected, forming small bundle-like aggregates. In detail, the fibers exhibit a needle-like structure with an average diameter of 23 $\pm$ 5 nm and a length ranging from 0.7 to 2.5 μm, consistent with the literature data.[7]

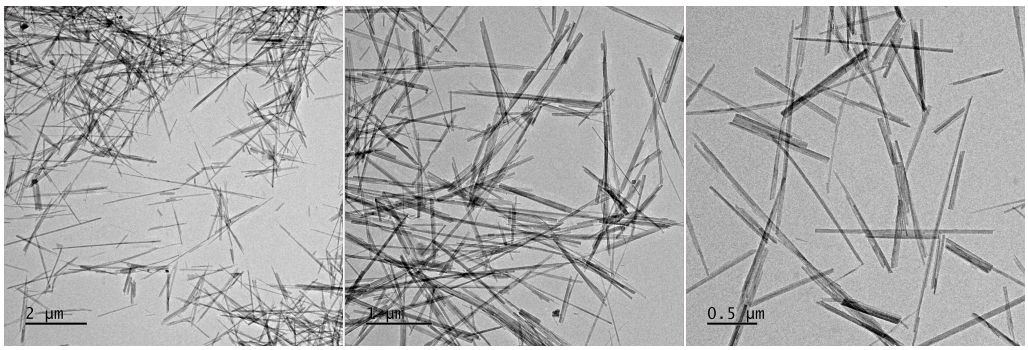

Figure 2.5: TEM micrographs of pristine SepOH NFs

Nitrogen physisorption

For SepOH nanofibers, the nitrogen adsorption-desorption isotherm measured at 77K (Figure 2.6) is classified as a combination of type I and type IV, according to IUPAC standards, indicating the presence of both microp-

orous and mesoporous structures.[4] The pore size distribution, derived from the NLDFT model, reveals two main pore sizes with mean half-pore widths of approximately 0.43 nm and 0.72 nm, both within the micropore range (Figure 2.7).

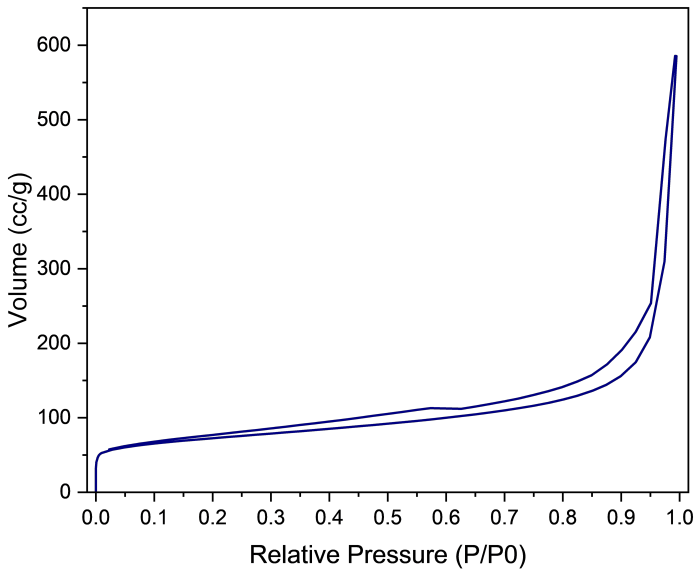

Figure 2.6: Nitrogen adsorption-desorption (77 K) isotherm of SepOH NFs

When considering the type IV component and using the BJH method to derive the pore size distribution, a decreasing trend is observed with increasing half-pore width (Figure 2.8). This suggests that SepOH nanofibers are primarily characterized by micropores rather than mesopores. The mesoporous component likely arises solely from the aggregation of nanofibers, which, as shown by TEM, tend to align into needle-like bundles even after pretreatment. For values of P/P0 $>$ 0.8, there is a significant increase in adsorbed volume ascribable to the filling of interparticle spaces. Gas adsorption analysis, based on BET and NLDFT models, indicates a BET surface area of 259 $\pm$ 1 m^2/g and a pore volume of 0.262 cc/g.

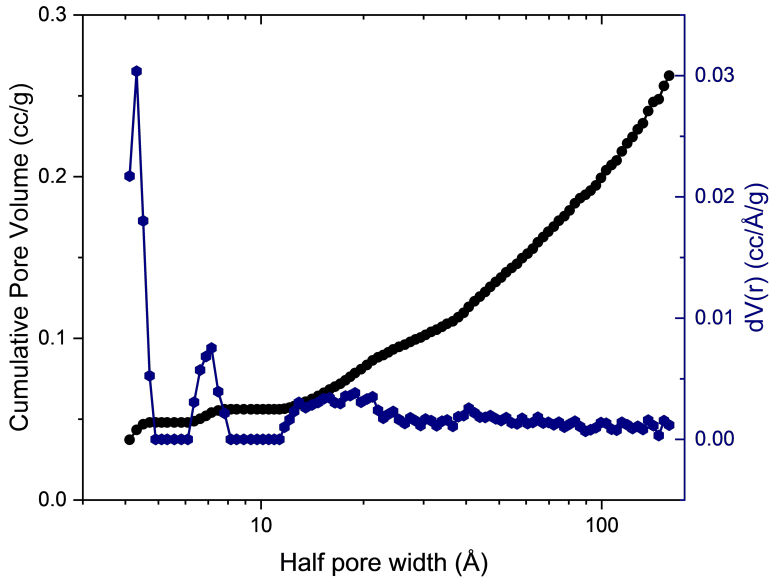

Figure 2.7: Cumulative pore volume and pore size distribution curves of SepOH NFs calculated by NLDFT model for microporous analysis

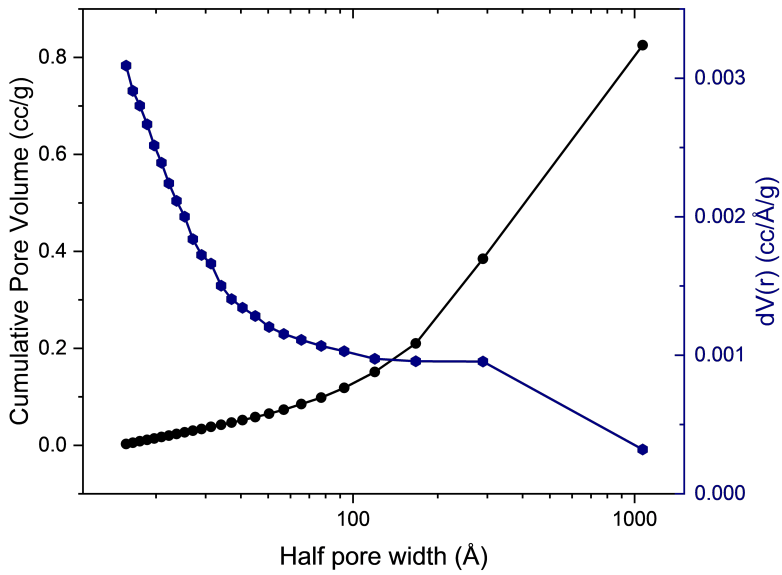

Figure 2.8: Cumulative pore volume and pore size distribution curves of SepOH NFs calculated by BJH model for mesoporous analysis

TGA

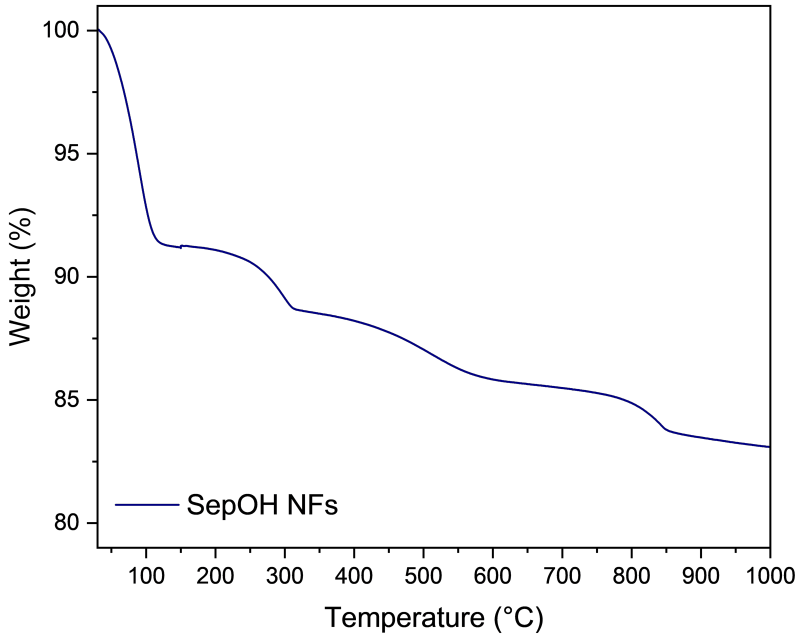

Figure 2.9: TGA curve of SepOH NFs

In this case, TGA cannot be used to estimate the amount of surface hydroxyl groups. Due to the structure of the material, the mass loss observed above 150°C cannot be solely attributed to the decomposition of surface hydroxyl groups. The thermogravimetric curve (Figure 2.9) shows several steps, each corresponding to different types of mass loss:

- up to 200°C, the mass loss is primarily due to the evaporation of hygroscopic and zeolitic water, which consists of water molecules adsorbed both on the external surface and within the channels of the sepiolite;
- between 200°C and 350°C, the loss of two of the four crystallization water molecules, which are weaklier bound, occurs;

- between 400°C and 600°C, the remaining two crystallization water molecules are lost;

- above 600°C, the loss is attributed to the release of constitutional water or hydroxyl groups.

In view of the above results, the loss of hydroxyl groups cannot be unambiguously identified within a specific temperature range. However, this analysis will be useful for estimating the degree of functionalization.[8]

2.2 Synthesis of the cinnamyl alkoxysilane

As described in the introduction, cinnamic acid is a naturally occurring carboxylic acid found in plant kingdom and is known for its photoresponsive properties, undergoing reversible photodimerization upon irradiation at specific wavelengths. To anchor cinnamic acid onto the surface of fillers, a new alkoxysilane was developed that covalently binds the cinnamic unit. Alkoxysilanes are commonly used compatibilizing agents for modifying oxide nanoparticle surfaces by reacting with surface hydroxyl groups.

Among these, 3-aminopropyltriethoxysilane (APTES) is particularly important due to its terminal amine group, which could interact with polymer matrices and coordinate with metal ions, providing enhanced properties for several applications. In this case, the carboxyl group of cinnamic acid and the amine group of APTES were used to create a new alkoxysilane, named CINN-APTES.

To synthesize this silane, cinnamic acid was first activated using carbodiimide chemistry to form the N-hydroxysuccinimide ester of cinnamic acid (CINN-NHS), according to a previous work.[9] This intermediate facilitated the reaction with APTES under mild conditions, preventing self-condensation of the silane.

2.2.1 Experimental Procedure of CINN-APTES

Materials

N-Hydroxysuccinimide 98% (NHS) and N,N'-dicyclohexylcarbodiimide 99% (DCC) were purchased from Sigma-Aldrich and used as received. APTES

98% was purchased from abcr. trans-Cinnamic acid (CINN) was purchased from Merck-Millipore. Anhydrous THF 99.8+% and Acetonitrile HPLC grade (MeCN) were purchased from VWR; Methanol HPLC grade was purchased from Thermo Fisher Scientific.

Synthesis of CINN-NHS

In a one-neck round-bottom-flask, 1.00 g of cinnamic acid (6.75 mmol) was dissolved in 14 mL of solution of MeCN and anhydrous THF (1:1). 1.809 g of DCC (8.77 mmol) and 0.854 g of NHS (7.42 mmol) were then added to the mixture, which was stirred at room temperature for 24 hours. The suspension was subsequently filtered, discarding the solid organic phase, while the liquid organic phase was concentrated. The resulting white residue was resuspended in 10 mL of MeOH and stirred for 30 minutes at room temperature. The precipitate was filtered, washed with MeOH (4 × 10 mL), and dried under vacuum overnight (Scheme 2.1). The crude product yielded approximately 55%. ^{1}H NMR (400.13 MHz, CDCl3): δ 7.98 (d, J = 16.05 Hz, ^{1}H), 7.63 (dd, J = 7.66, 1.62 Hz, 2H), 7.50–7.37 (m, 3H), 6.65 (d, J = 16.05 Hz, ^{1}H), 2.88 (s, 4H). NMR data are consistent with the literature data.[9]

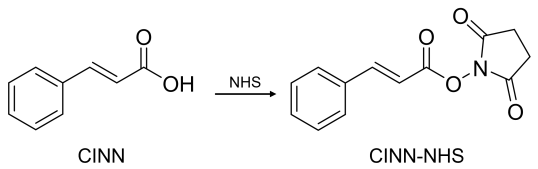

Scheme 2.1: Preparation of CINN-NHS

Synthesis of CINN-APTES

100 mg of previously synthesized CINN-NHS (0.41 mmol) was dissolved in 4.1 mL of anhydrous THF. APTES (96 μL, 0.41 mmol) was added dropwise, and the reaction mixture was stirred at room temperature for 1 hour (Scheme 2.2). The solvent was then evaporated, yielding a colorless oil identified as CINN-APTES. Due to the high reactivity of this organosilane, purification was not feasible, and the product was used directly for the functionalization of the filler surface. The yield of CINN-APTES, calculated using ^{1}H-NMR, was approximately 90% (see paragraph 2.2.2).

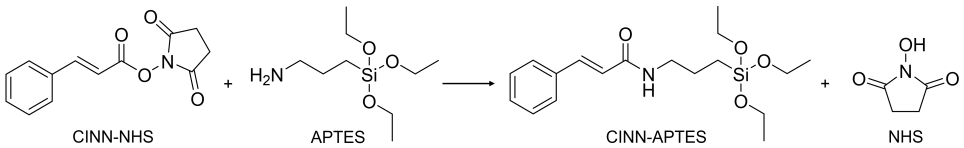

Scheme 2.2: Preparation of CINN-APTES

2.2.2 Characterization of CINN-APTES

NMR Spectroscopy

The structure of the newly synthesized organosilane was characterized using ^{1}H-NMR, ^{13}C-NMR and ^{1}H-^{13}C HSQC NMR spectroscopy. For thorough analysis, the spectrum of the organosilane was compared with those of two reference compounds, CINN-NHS and APTES (Figure 2.10).

The ^{1}H-NMR spectrum of CINN-APTES was analyzed by assigning the signals of the cinnamic unit, APTES unit, and NHS byproduct based on literature data.[9, 10] Signals between 8.0 and 6.5 ppm correspond to the protons

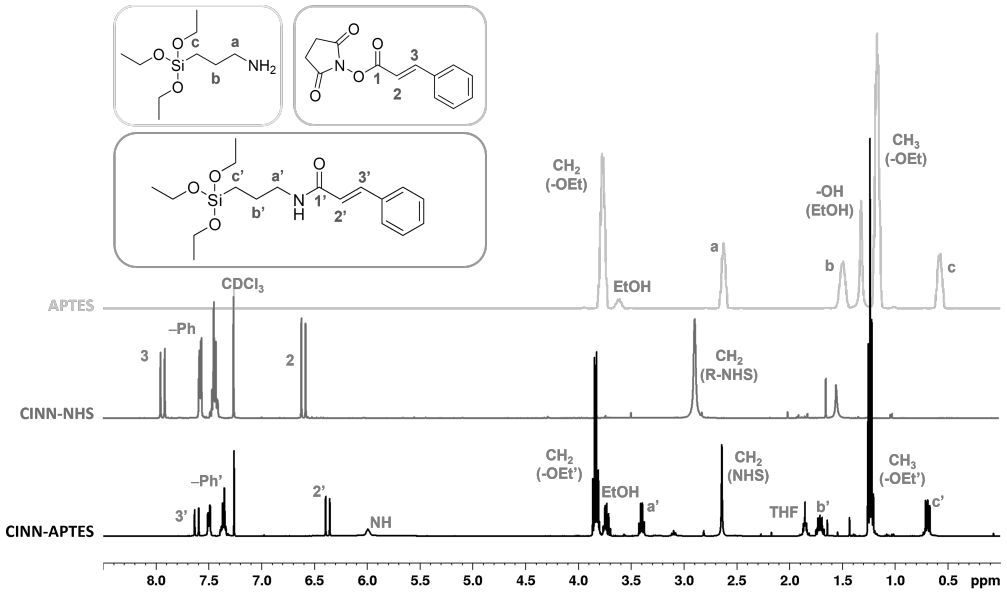

Figure 2.10: ^{1}H NMR spectra of APTES, CINN–NHS, and the novel CINN-APTES organosilane

of the benzene ring and the carbon-carbon double bond. Typically, alkene protons resonate between 6.0 and 4.5 ppm, but due to conjugation with the benzene ring, these protons are deshielded, causing a shift to higher chemical shifts. The two double bond protons (H-2', H-3') appear as doublets with the same coupling constant (J), each integrating for 1. The least shielded protons, around 0.7 ppm, correspond to the methylene group (-CH_2-) of APTES bonded to silicon. This occurs because silicon is more electropositive than carbon, shifting the electron cloud toward the carbon atom. The most deshielded protons below 5.0 ppm are from the -CH_2- groups of the ethoxy groups, due to oxygen's higher electronegativity. The -CH_2- protons bonded to the nitrogen of the amide group, less electronegative than oxygen, resonate slightly lower at 3.4 ppm.

The ^{1}H-NMR spectrum of CINN-APTES shows an upfield shift of the peaks

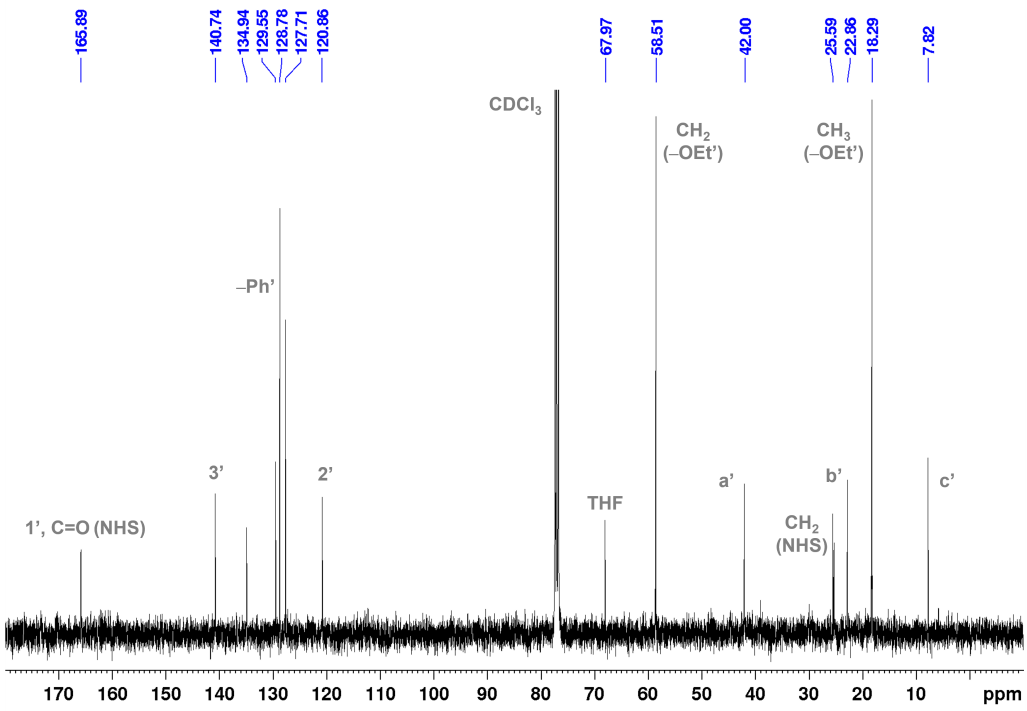

Figure 2.11: ^{13}C-NMR spectrum of CINN-APTES

in the region between 8.0 and 6.0 ppm compared to CINN-NHS, indicating a change in the chemical environment of the vinyl aryl protons. Additionally, the disappearance of the peak at 2.6 ppm (H-a in APTES) and the appearance of a new peak at 3.4 ppm (H-a' in CINN-APTES) indicate the loss of the amine group and the formation of an amide group. Further confirmation comes from the integration of the signals: the ratio of H-3' (-CH- attached to the benzene ring) to the two protons (H-a') of -CH_2- attached to nitrogen is 1:2, consistent with the molecular structure. The NHS byproduct protons resonate at 2.6 ppm, as noted in the literature[11], while in CINN-NHS, they resonate at 2.9 ppm. The upfield shift for the CH_2(NHS) resonance indicates the presence of free NHS as a side-reaction product. Finally, a signal at 6.0 ppm confirms the presence of a hydrogen atom bonded to the amide

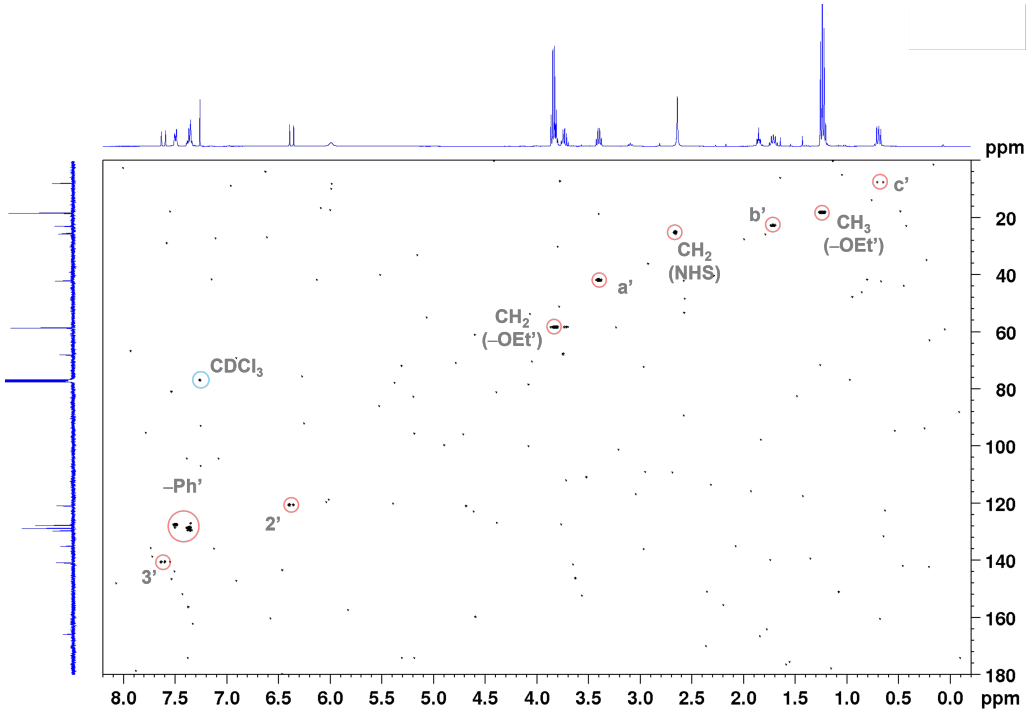

Figure 2.12: ^{1}H-^{13}C HSQC NMR spectrum of CINN-APTES

nitrogen. These combined observations confirm the successful synthesis of a new trialkoxysilane containing a light-responsive cinnamyl group.

The reaction yield, approximately 90%, was calculated as the average of the ratios of the integrals of the 3' to 3 signals and the 2' to 2 signals. The respective signals of reagents 3 and 2 were present in minimal amounts and were only visible upon closer examination in the CINN-APTES ^{1}H-NMR spectrum.

The ^{13}C-NMR spectrum of CINN-APTES (Figure 2.11) was analyzed using the same methodology applied to ^{1}H-NMR spectrum. The most deshielded carbon atoms correspond to the carbonyl groups, while carbon signals above 100 ppm are associated with the double bond and benzene ring. Exact as-

signments were confirmed by heteronuclear 2D NMR (Figure 2.12). Carbon signals from the APTES unit below 100 ppm were assigned based on deshielding effects similar to those observed in the ^{1}H-NMR spectrum.

UV-Vis Spectroscopy

The UV-Vis spectrum of CINN-APTES was obtained to confirm the absorption features of the newly synthesized molecule. A maximum absorption wavelength was detected at 277 nm (shown as the darker curve in the Figure 2.13).

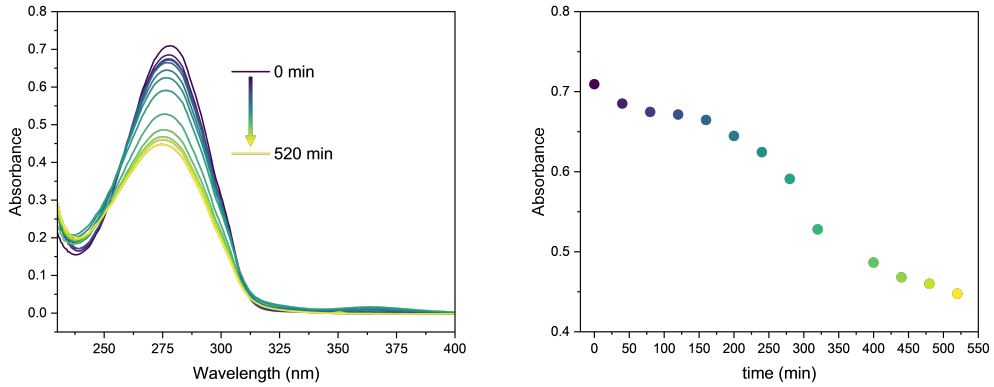

Figure 2.13: 13 UV-Vis spectra of CINN-APTES sample after exposure at $\lambda \sim$ 365 nm; (right) maximum absorption plotted against UV irradiation time at $\lambda =$ 365 nm

To preliminarily assess the photoresponsive properties of the new molecule, a 10^{-4} M solution of CINN-APTES in DCM was prepared. The solution was placed in a quartz cuvette and irradiated with a 365 nm lamp at various intervals. As shown in Figure 2.13, a gradual decrease in the absorbance at the maximum absorption peak was observed. According to the Lambert-Beer

law, this decrease is directly proportional to the reduction of the molecule's concentration. As reported in the literature[12], this depletion indicates of the occurrence of the cinnamyl units photodimerization reaction.

2.3 Preparation of cinnamyl functionalized fillers

As outlined in the introduction, this section presents two different strategies for preparing functionalized cinnamyl fillers. The first strategy involves the use of the previously described CINN-APTES for direct surface functionalization of the fillers in a single-step procedure (Scheme 2.3).

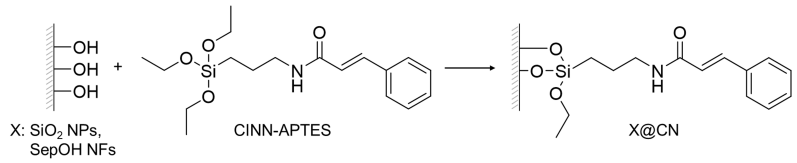

Scheme 2.3: One-step functionalization reaction of both SiO_2 NPs and SepOH NFs

The second strategy follows a more conventional approach, in which the cinnamyl functionalization is applied after the compatibilizing agent, APTES, has been pre-anchored to the filler surface (see Scheme 2.4). Two different cinnamyl derivatives are used in this method: the previously synthesized cinnamic acid N-hydroxysuccinimide ester (CINN-NHS) and the commercially available derivative cinnamoyl chloride (CNCOCl).

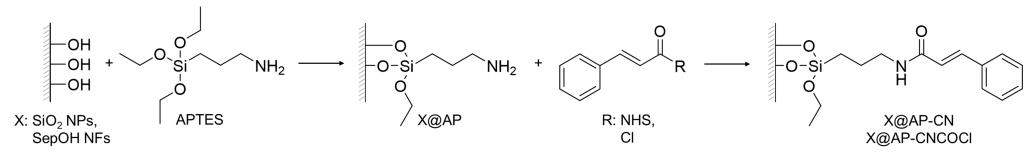

Scheme 2.4: Double-step functionalization reaction of both SiO_2 NPs and SepOH NFs

The advantages and disadvantages of both strategies will be thoroughly discussed. In each case, for the surface functionalization reactions, the amount

of silane used was calculated based on the number of surface hydroxyl groups on the fillers, assuming that typically only two of the ethoxy groups of the alkoxysilane react with these surface hydroxyl groups.

Materials

APTES 98% was purchased from abcr. Ammonia solution 25 wt.% (NH_3) for analysis and Cinnamoyl Chloride (CNCOCl) were purchased from Merck-Millipore. Tetrahydrofuran 99% (THF), anhydrous THF 99.8+%, Toluene (99%) and Dichloromethane (DCM) were purchased from Alfa Aesar. Absolute anhydrous Ethanol was purchased from VWR; Methanol HPLC grade, and sodium hydroxide 98% (NaOH) were purchased from Thermo Fisher Scientific.

2.3.1 Synthesis of SiO_2@CN NPs

2.3.1.1 Experimental Procedure of SiO_2@CN NPs

In a two-neck round-bottom flask, 100 mg of SiO_2 NPs were dispersed in 3.0 mL of ethanol using an ultrasonic bath for 2 minutes, and the mixture was brought to reflux. A solution of 25 wt.% NH_3 (10 μL) and the appropriate amount of previously synthesized CINN-APTES, dissolved in 2.0 mL of ethanol, were added dropwise to the dispersion. The reaction mixture was kept under reflux with vigorous stirring for 12 hours. Afterward, the mixture was centrifuged at 9000 rpm for 15 minutes and washed several times with ethanol to remove excess CINN-APTES and the NHS by-product from the CINN-APTES synthesis. Finally, the functionalized SiO_2 NPs (SiO_2@CN NPs) were dried under vacuum for 3 hours.

2.3.1.2 Characterization of SiO_2@CN NPs

SEM-EDX

SEM-EDX analysis was used to verify initially the grafting of CINN-APTES onto the silica surface. In particular, Figure 2.14 shows SEM and SEM-EDX micrographs of the same SiO_2@CN nanoparticle agglomerate, respectively. The carbon atom distribution (marked by pink dots in Figure 2.14) is uniform and located on the surface, indicating the presence of carbonaceous residues likely associated with the CINN-APTES units.

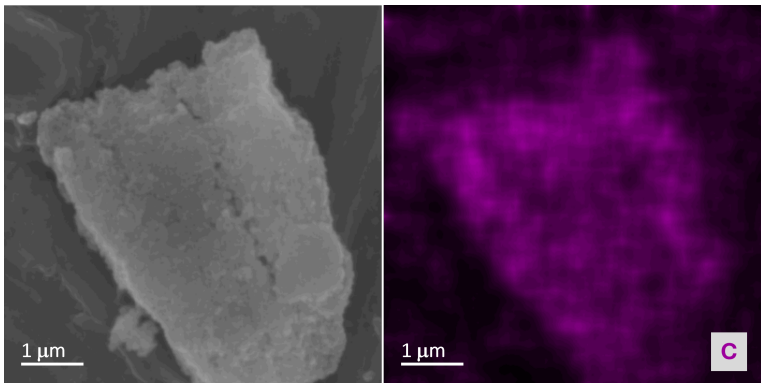

Figure 2.14: SEM and SEM-EDX micrographs of the same SiO_2@CN nanoparticle agglomerate

ATR-FTIR

The presence of CINN-APTES on the NPs surface was further assessed by ATR-FTIR (Figure 2.15). The infrared spectrum of SiO_2 NPs exhibits several key bands. The stretching and bending vibrational modes of OH groups from physically adsorbed water are observed in the region between 3700 and 3200 cm^{-1} and at 1633 cm^{-1}, respectively. The Si-O-Si stretching vibrations appear at 1060 cm^{-1}, while the Si-OH stretching is evident

at 954 cm^{-1}. In the case of SiO_2@CINN-APTES, the peaks around 3000 cm^{-1} correspond to asymmetrical C-H stretching, which arises from both the aliphatic chain and the aromatic ring of CINN-APTES. The characteristic vibrational bands of C=O stretching (1680 cm^{-1}) from the amide group and C=C stretching (1630 cm^{-1}) conjugated to the aromatic ring confirm the presence of CINN-APTES on the silica surface. Additionally, the peak at 1582 cm^{-1} is attributed to N-H bending of the amide group and C=C stretching of the aromatic ring, while the bands between 1550 and 1350 cm^{-1} are associated with the C=C stretching vibrations of the aromatic ring in CINN-APTES. Finally, the depletion of the Si-OH stretching band at 954 cm^{-1} indicates a reduction in Si-OH groups, suggesting their involvement in the grafting process. These findings qualitatively confirm the presence of CINN-APTES on the silica surface.

Solid state NMR

The ^{29}Si-NMR spectrum of SiO_2 NPs (Figure 2.17) shows features similar to those observed for Rhodia SiO_2 NPs, with Q^4, Q^3, and Q^2 units appearing at -110, -100, and -92 ppm, respectively.[13]

The spectrum of SiO_2@CN NPs displays the same Q signals, along with additional T^3 and T^2 (Figure 2.16) resonances at -66 and -57 ppm, attributed to the presence of organic chains covalently bonded to the surface of the nanoparticles, CINN-APTES. Moreover, from a qualitative perspective, the functionalization leads to a reduction in the Q^3 and Q^2 units due to the replacement of surface -OH groups on the silica with CINN-APTES, providing further confirmation of the successful surface functionalization of the SiO_2

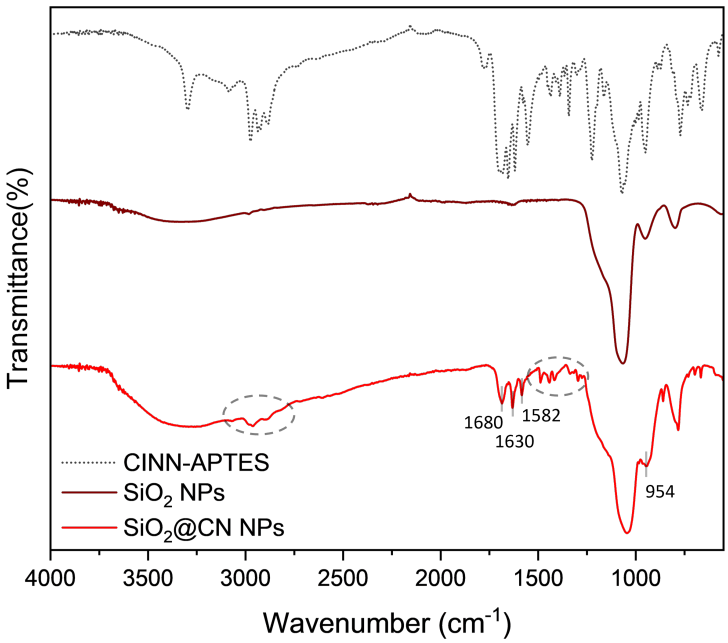

Figure 2.15: ATR-FTIR-normalized spectra of pristine SiO_2 NPs, CINN-APTES novel and SiO_2@CN NPs

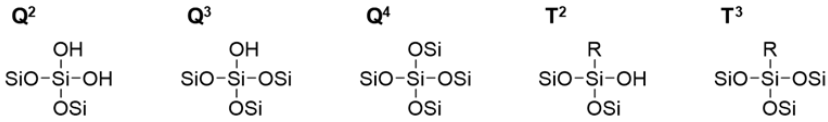

Figure 2.16: Representation of Q^n an T^n units

NPs. Quantitative Magic Angle Spinning (MAS) experiments indicate that for every 100 Q units, there are at least 6 T units, which is evidence of a significant presence of silane on the surface of the SiO_2 NPs. Furthermore, the silica exhibits a good degree of condensation (DOC), which increases with subsequent functionalization. The results are presented in Table 2.1.

The ^{13}C spectrum from Cross Polarization Magic Angle Spinning (CPMAS) of SiO_2@CN NPs, shown in Figure 2.18, displays all the characteristic peaks

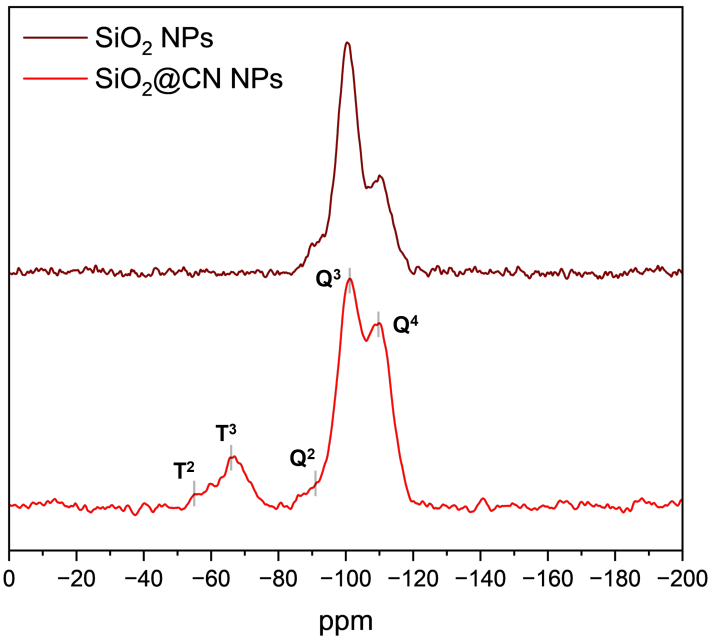

Figure 2.17: ^{29}Si MAS spectra of SiO_2 and SiO_2@CN NPs

Table 2.1: Quantitative Magic Angle Spinning (MAS) results of SiO_2 and SiO_2@CN NPs

	T^2	T^3	Q^2	Q^3	Q^4	DOC
δ (ppm)	-57.0	-66.3	-90.4	-100.4	-110.0	
SiO_2 NPs (%)	-	-	3.8	30.4	65.8	90.5
SiO_2@CN NPs (%)	1.3	4.6	0.8	17.5	75.8	94.8
			(0.9)*	(18.6)*	(80.5)*	(94.9)*

*DOC calculated for the SiO_2@CN NPs sample, considering only the Q^n units

of CINN-APTES. Notably, the peaks at 58 and 17 ppm indicate a significant presence of ethoxy groups, with the splitting of the 58 ppm signal into two components suggesting the presence of both -OEt and residual EtOH groups. However, the downfield shift of the C-c' peak reflects the condensation of the inorganic silane head, confirming its successful grafting onto the

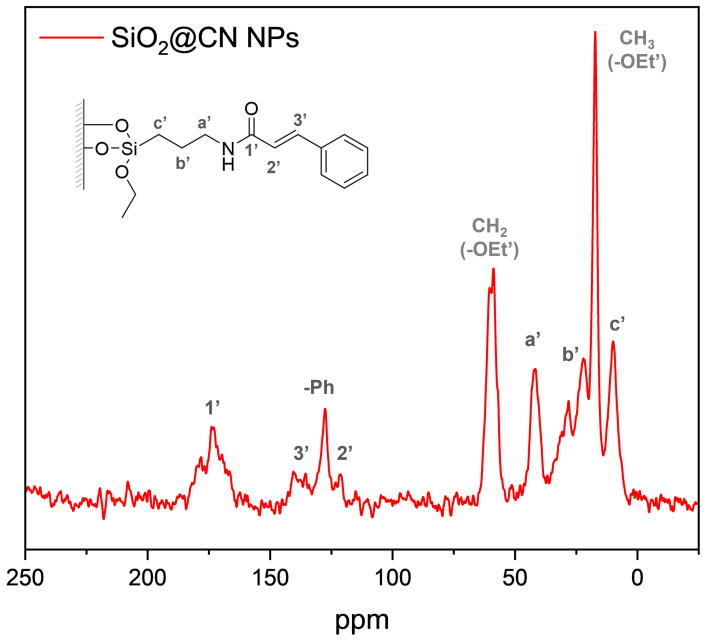

Figure 2.18: ^{13}C CPMAS spectrum of SiO_2@CN NPs

silica surface. Moreover, the signal corresponding to the carbon at position b' is split into two components at 28.1 and 22.1 ppm, attributed to its sensitivity to the electronic environment of the nitrogen. This interaction leads to structural rearrangements and a change in the orientation of the propyl chain, consistent with the γ-gauche effect.[13, 14] Furthermore, the lineshape of the C-1' signal, associated with the amide bond, is asymmetric, with at least two components. This asymmetry may reflect different conformations, as suggested by the splitting of the C-b' resonance.

TGA

To estimate the amount of CINN-APTES covalently bound to the surface of SiO_2@CN NPs, TGA was performed, and the thermogram was compared

to that of bare SiO_2 NPs (Figure 2.19). The greater weight loss observed for SiO_2@CN NPs between 150°C and 1000°C is attributed to the higher percentage of organic content likely associated with CINN-APTES, as confirmed by previous results. Assuming the increased weight loss in this temperature range is solely due to the molecular fraction of CINN-APTES, the degree of functionalization, expressed both as a mass percentage and as σ (number of molecules per unit area), was calculated using Equation A.3 and Equation A.4 (provided in the appendix) and shown in the Table 2.2.

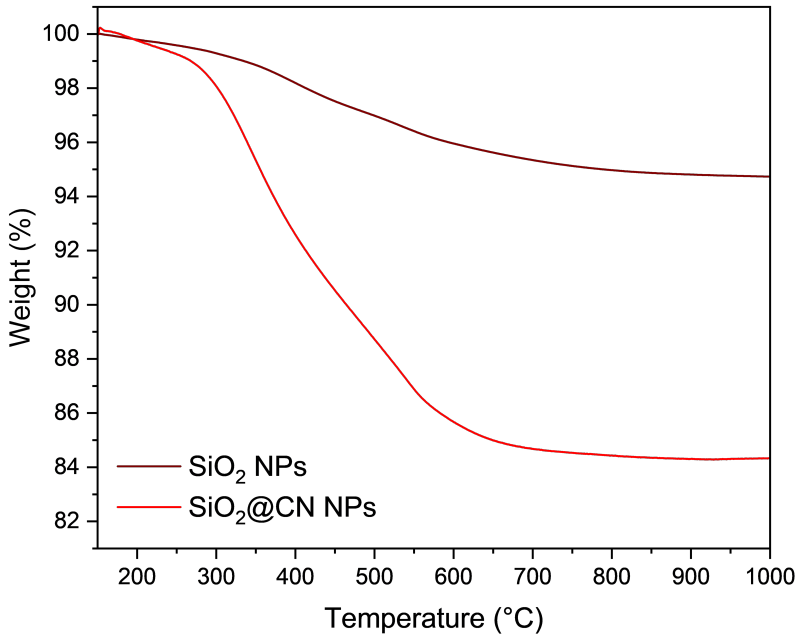

Figure 2.19: TGA curve of SiO_2 and SiO_2@CN NPs

Table 2.2: Functionalization degree (both wt.% and σ) of SiO_2@CN NPs

	wt%(Y)	**σ (n./nm^2)**
SiO_2@CN NPs	12.85	1.83

CHNS

Table 2.3 presents the results of elemental analysis for both functionalized and unfunctionalized silica samples.

Table 2.3: CHNS elemental analysis results of SiO_2 and SiO_2@CN NPs

Sample	C (wt.%)	H (wt.%)	N (wt.%)	S (wt.%)
SiO_2 NPs	1.18	1.284	0	0.299
SiO_2@CN NPs	8.60	1.596	1.55	0.135

As expected, the mass percentage of carbon and nitrogen atoms increases in the functionalized sample due to the presence of CINN-APTES. Using Equation A.4, as explained in the appendix, the sigma value for the SiO_2@CN sample was estimated to be 1.86 n./nm^2, which is in close agreement with the value obtained from thermogravimetric analysis. This consistency highlights both the accuracy of the estimation and the effectiveness of the functionalization reaction.

2.3.2 Synthesis of SepOH@CN NFs

2.3.2.1 Experimental Procedure of SepOH@CN NFs

In a single-neck round-bottom flask, 100 mg of CINN-NHS (0.41 mmol) was dissolved in 4.1 mL of anhydrous THF. APTES (96 μL, 0.41 mmol) was added dropwise, and the reaction mixture was stirred at room temperature for 1 hour to form CINN-APTES silane. Afterward, 55 mg of SepOH nanofibers were added, and the mixture was refluxed with vigorous stirring for 24 hours. The product (SepOH@CN NFs) was recovered by centrifugation, washed with THF, and dried under vacuum for 3 hours.

2.3.2.2 Characterization of SepOH@CN NFs

SEM-EDX

As with silica nanoparticles, SEM-EDX analysis was employed to preliminarily assess the presence of carbon chains on the functionalized sepiolite nanofibers. Figure 2.20 shows that the red dots indicate a higher concentration of carbon atoms along the nanofiber boundaries, providing initial evidence of the potential presence of CINN-APTES on the surface.

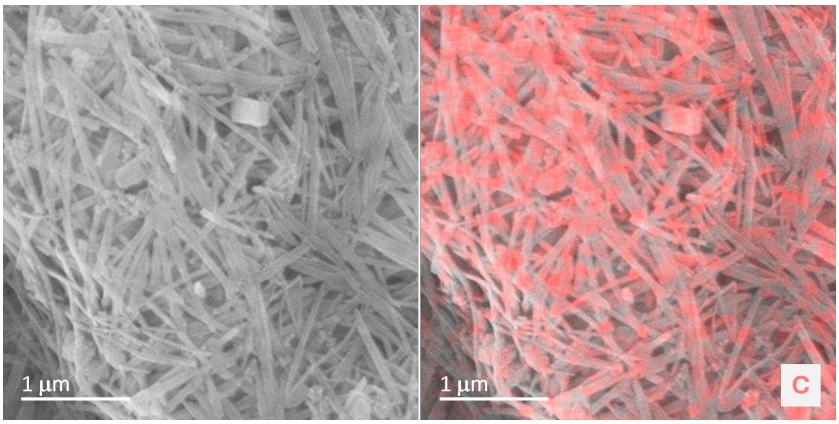

Figure 2.20: SEM and SEM-EDX micrographs of the same SepOH@CN NFs

ATR-FTIR

ATR-FTIR analysis was performed on SepOH, SepOH@CN, and pure CINN-APTES to preliminarily verify the functionalization of sepiolite nanofibers. The spectra of both SepOH and SepOH@CN NFs, shown in Figure 2.21, exhibited characteristic signals, including bands at 3560 cm^{-1}, corresponding to Al-OH and Mg-OH groups, and a band in the range of 3400–3200 cm^{-1}, attributed to adsorbed water and hydroxyl groups within the sepiolite structure. A prominent band at 1657 cm^{-1}, observed in both samples,

was linked to the bending vibrational mode of water but may also be attributed to the C=O stretching of the amide group in SepOH@CN NFs, as indicated by a significant increase in intensity and a change in the lineshape.

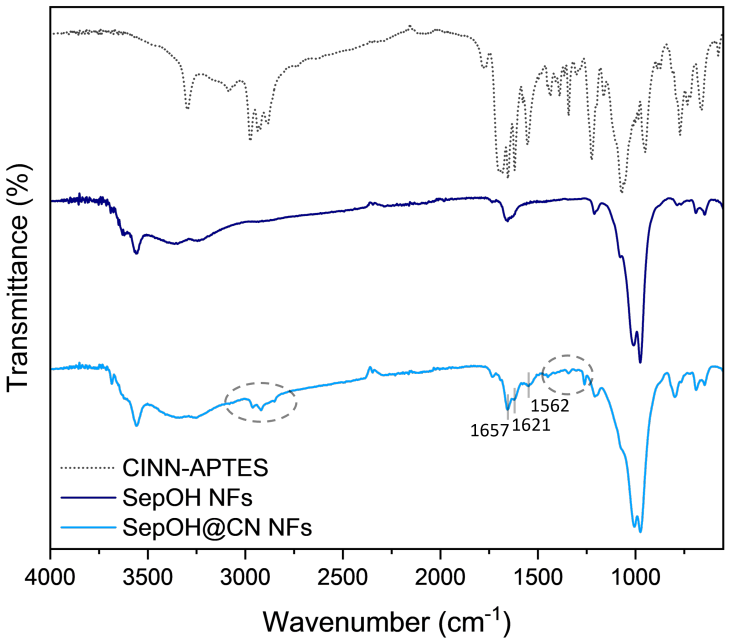

Figure 2.21: ATR-FTIR-normalized spectra of pristine SepOH NFs, CINN-APTES novel and SepOH@CN NFs

Additionally, bands at 1211 cm^{-1}, 786 cm^{-1}, and 690 cm^{-1} were assigned to the characteristic Si-O-Si and O-Si-O bonds linking the tetrahedral units, while the two signals at 1009 cm^{-1} and 976 cm^{-1} were associated with the stretching vibrations of $[SiO_4]$ tetrahedral units. A band at 645 cm^{-1} was attributed to the characteristic signal of the Mg_3OH unit, while a feature at 1734 cm^{-1}, likely due to acetone impurities, was also detected.

In SepOH@CN NFs, additional unique signals were observed, confirming the

presence of CINN-APTES on the sepiolite surface. These included bands between 2970 cm^{-1} and 2920 cm^{-1}, corresponding to alkyl groups, and a signal at 1621 cm^{-1}, which, although partially masked by water, was attributed to the C=C conjugated bond. Furthermore, a band at 1562 cm^{-1}, corresponding to the N-H bending mode of the amide group, and peaks between 1550 cm^{-1} and 1350 cm^{-1}, associated with the C-C stretching vibrations of the aromatic ring in CINN-APTES, were clearly detectable.

ss-NMR

The ^{29}Si CPMAS NMR spectra of SepOH and SepOH@CN NFs are presented in Figure 2.22. In all cases, three well-resolved resonances are observed at chemical shifts of 90, 93, and 96 ppm. These peaks correspond to Q^3 silicon environments,[15] representing the three distinct positions of silicon atoms within the sepiolite microstructure, as identified in Figure 2.23. The functionalization of the sample with CINN-APTES is clearly evident, as shown by the additional resonances corresponding to T^3 and T^2 units at approximately 65 and 56 ppm, respectively. These signals indicate the formation of organosilane bonds resulting from the surface modification with CINN-APTES. Quantitative analysis shows a ratio of approximately 100:10 between Q units and T units, highlighting the dominance of the native silicon environments over the functionalized sites.

The successful grafting of CINN-APTES onto the sepiolite surface was confirmed by ^{13}C solid-state NMR (Figure 2.24). Characteristic peaks corresponding to the newly formed silane chain were observed at 11 ppm (C-c'), 22 ppm (C-b'), and 43 ppm (C-a'). Additionally, a peak at 167 ppm was

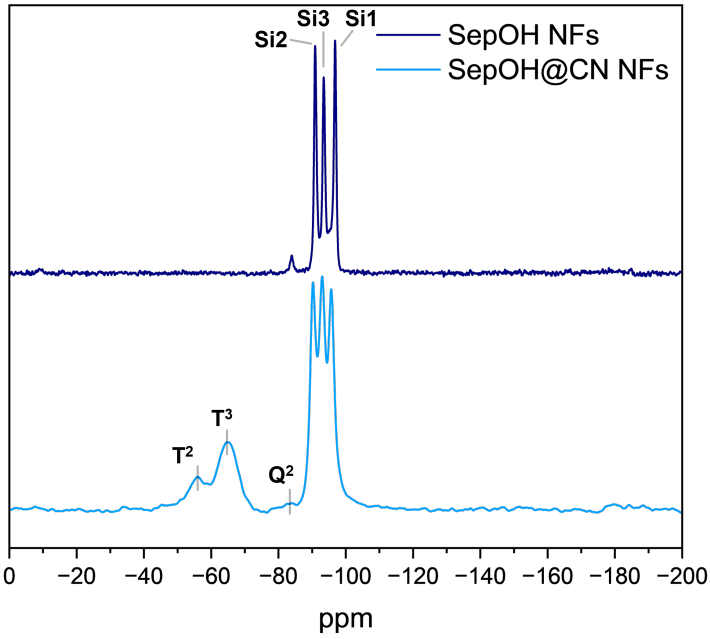

Figure 2.22: ^{29}Si MAS spectra of SepOH and SepOH@CN NFs

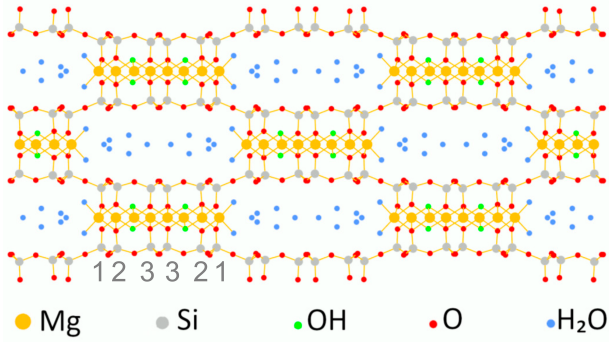

Figure 2.23: Ball and stick model of sepiolite structure with identification of Si1, Si2 and Si3 units[16]

assigned to the carbonyl group (C-1'), while the vinyl carbons were observed at approximately 140 and 122 ppm (C-3' and C-2', respectively). A distinct aromatic ring resonance was centered around 128 ppm, indicating the presence of the cinnamyl moiety.

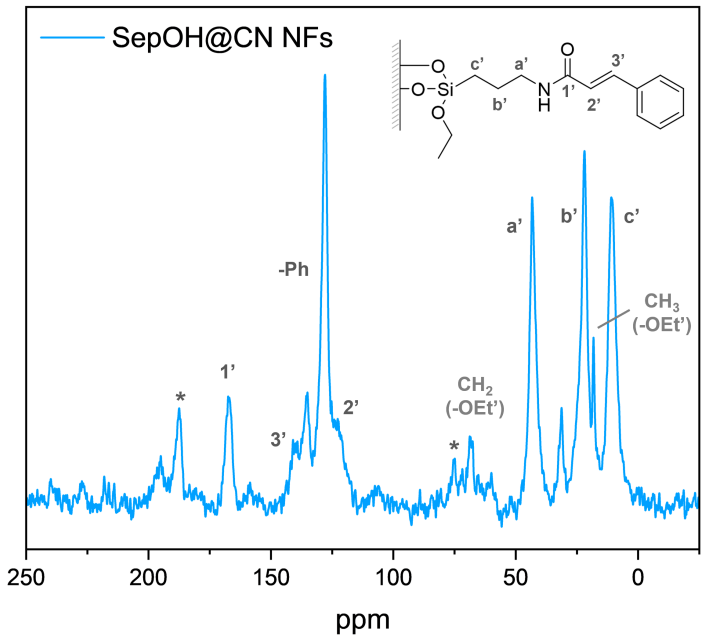

Figure 2.24: ^{13}C CPMAS NMR spectrum of SepOH@CN NFs

Further signals at 18 ppm and 60 ppm, corresponding to CH_3 and CH_2 groups, respectively, were attributed to residual, non-hydrolyzed ethoxy groups from CINN-APTES. These peaks suggest an incomplete condensation of the silanol groups, indicating that some unreacted ethoxy groups remained attached to the silane structure. Moreover, two additional signals detected at approximately 31 and 129 ppm are likely linked to residual acetone and toluene, respectively, from the reaction or purification steps. [13, 14, 17, 18]

TGA

After evaluating the success of the functionalization reaction, thermogravimetric analysis (TGA) was performed to estimate the amount of function-

alizing agent grafted onto the nanofiber surfaces (Figure 2.25). In this case, the mass loss between 150°C and 1000°C cannot be solely attributed to the decomposition of the functionalizing agent, as other factors must also be considered.

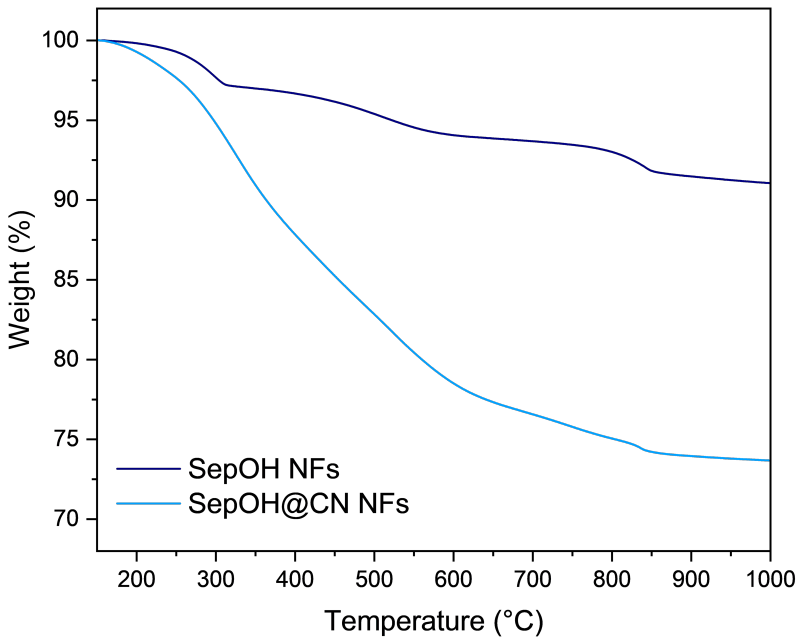

Figure 2.25: TGA curves of SepOH and SepOH@CN NFs

First, the microporous structure of the fibers traps water molecules that are not fully eliminated at 150°C. Even at higher temperatures, adsorbed water continues to be released, as indicated by multiple steps in the thermogram (curve dark blue Fig.), where both adsorbed water and surface-bound hydroxyl groups are lost simultaneously.

Additionally, during the functionalization process, silane may become intercalated and adsorbed within the sepiolite pores. The purification steps

(ultrasonication and centrifugation) may not be sufficient to remove all the adsorbed material, some of which may only be released above 150°C.

Since silane decomposition (the primary focus of the calculation) occurs simultaneously with these processes, it is impossible to isolate and quantify their individual contributions. In order to estimate the degree of functionalization, the same calculation method used for silica is applied here, with the understanding that the aforementioned contributions are neglected. Table 2.4 contains the degree of functionalization, expressed as both a mass percentage and as σ (the number of molecules per unit area), calculated using Equation A.3 and Equation A.4 (provided in the appendix).

Table 2.4: Functionalization degree (wt.% and σ) of SepOH@CN NFs

	wt%(Y)	**σ (n./nm^2)**
SepOH@CN NFs	18.23	3.13

CHNS

The elemental analysis conducted on the SepOH and SepOH@CN samples yielded the results presented in the Table 2.5. As anticipated, functionalization of the sepiolite nanofibers with CINN-APTES resulted in an increased percentage of carbon and nitrogen atoms in the sample. Using Equation A.4, detailed in the appendix, the sigma value for the SepOH@CN sample was estimated to be 2.99 n./nm^2. It is important to note that this result likely overestimates the true value, as the calculation does not account for any uncondensed ethoxy groups from the silane. Nevertheless, the CHNS analysis results align closely with those obtained from the TGA analysis,

confirming the reliability of the data.

Table 2.5: CHNS elemental analysis results of SepOH and SepOH@CN NFs

Sample	C (wt.%)	H (wt.%)	N (wt.%)	S (wt.%)
SepOH NFs	0.33	1.747	0.51	0.223
SepOH@CN NFs	13.13	2.588	0.76	0.042

2.3.3 Double-step preparation of cinnamyl functionalized SiO_2 NPs using CINN-NHS

To assess the effectiveness of the one-step strategy, where the filler is directly functionalized with silane covalently binding the cinnamic unit, the N-hydroxysuccinimide ester of cinnamic acid (CINN-NHS) was used to modify the amine groups of APTES that had already been grafted onto the surface of silica nanoparticles (as illustrated in Scheme 2.5).

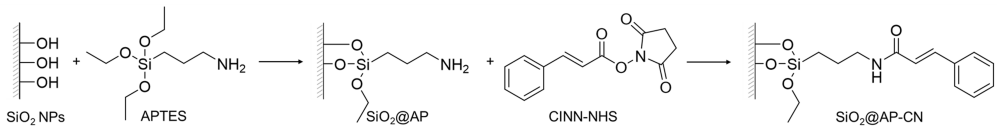

Scheme 2.5: Double-step functionalization reaction of SiO_2 NPs using CINN-NHS

Silica nanoparticles were selected as the model system due to their well-defined surface chemistry and ease of functionalization. The amount of APTES required was calculated based on the assumption that typically only two ethoxy groups of the alkoxysilane react with the surface hydroxyl groups of silica.

The quantity of CINN-NHS to be utilized in the reaction was determined from the results of thermogravimetric analysis (TGA), which provided an estimation of the number of APTES units successfully grafted onto the silica surface. Based on this evaluation, 1.5 equivalents of CINN-NHS per mole of surface-bound amine groups were added to ensure a slight excess of the cinnamic units, optimizing the conditions for providing complete functionalization and sufficient availability of the CINN-NHS for covalent attachment to the amine groups.

2.3.3.1 Experimental procedure of SiO_2@AP-CN

Step 1: Functionalization of SiO_2 NPs with APTES

200 mg of SiO_2 NPs were dispersed in 10.0 mL of ethanol. Once the suspension reached reflux conditions, a solution of 25 wt.% NH_3 (20 μL) and APTES (218 μL) were added dropwise, and the reaction mixture was stirred under reflux for 12 hours. After centrifugation at 9000 rpm for 15 minutes and several ethanol washes, the SiO_2@AP NPs were dried under vacuum for 3 hours.

Step 2: Derivatization of the Amino Group of SiO_2@AP NPs

100 mg of SiO_2@AP NPs (0.053 mmol of NH_2, calculated by TGA analysis, see 1.3.3.2, were dispersed in 5.0 mL of THF in a two-neck round bottom flask by ultrasonication (2 min). Then, 20 mg of CINN-NHS (0.082 mmol) was added to the dispersion, and the reaction was stirred at room temperature for 1 hour. The product (SiO_2@AP-CN NPs) was recovered by centrifugation, washed with THF, and dried under vacuum for 3 hours.

2.3.3.2 Characterization of SiO_2@AP-CN

ATR-FTIR

Figure 2.26 shows the ATR-FTIR spectra of SiO_2, SiO_2@AP, and SiO_2@AP-CN NPs. Functionalization with APTES alone does not result in notable changes in the spectrum of SiO_2@AP, which closely resembles that of bare SiO_2. This is likely due to the low intensity of the characteristic vibrational modes associated with the APTES unit. However, a reduction in the signal at 954 cm^{-1}, attributed to the vibration of the Si-OH bond, can be observed, indicating that this hydroxyl group has been utilized by the functionalizing agent.

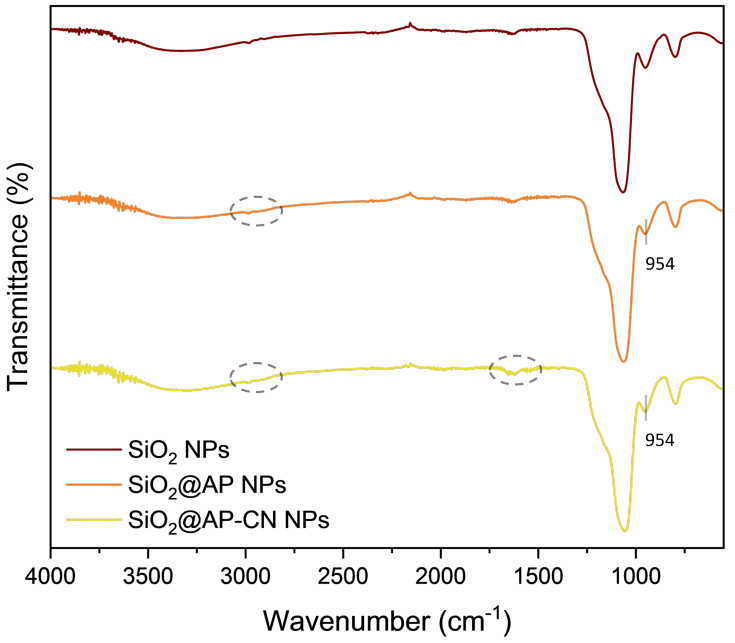

Figure 2.26: ATR-FTIR specta of SiO_2, SiO_2@AP and SiO_2@AP-CN NPs

In contrast, after the derivatization of SiO_2@AP with CINN-NHS, new sig-

nals emerge in the 1700 cm^{-1} to 1630 cm^{-1} region. These are likely associated with the stretching vibrations of the C=O bond in the newly formed amide group and the C=C bond of the cinnamic unit. In both the SiO_2@AP and SiO_2@AP-CN spectra, no significant changes are observed in the stretching vibrations of aliphatic and aromatic C-H bonds around 3000 cm^{-1}, possibly due to a low degree of functionalization.

TGA

To highlight the efficacy of the one-step strategy in comparison to the double-step procedure, the degree of functionalization of the SiO_2@AP-CN NPs was determined using thermogravimetric analysis, following the procedure outlined in the appendix. The thermograms of bare SiO_2, SiO_2@AP, and SiO_2@AP-CN NPs in the temperature range of 150–1000°C are reported in Figure 2.27. It is assumed that the mass loss observed for SiO_2@AP corresponds to the presence of the APTES unit, while for SiO_2@AP-CN, the additional mass loss relative to SiO_2@AP is attributed solely to the cinnamic unit.

The weight losses and corresponding degrees of functionalization for both samples are summarized in the Table 2.6. Notably, the one-step strategy achieves a degree of functionalization of approximately 1.8 n./nm^2 (as discussed in the paragraph), which is roughly six times higher than the value obtained through the two-step approach. This clearly highlights the superior efficiency of the one-step procedure.

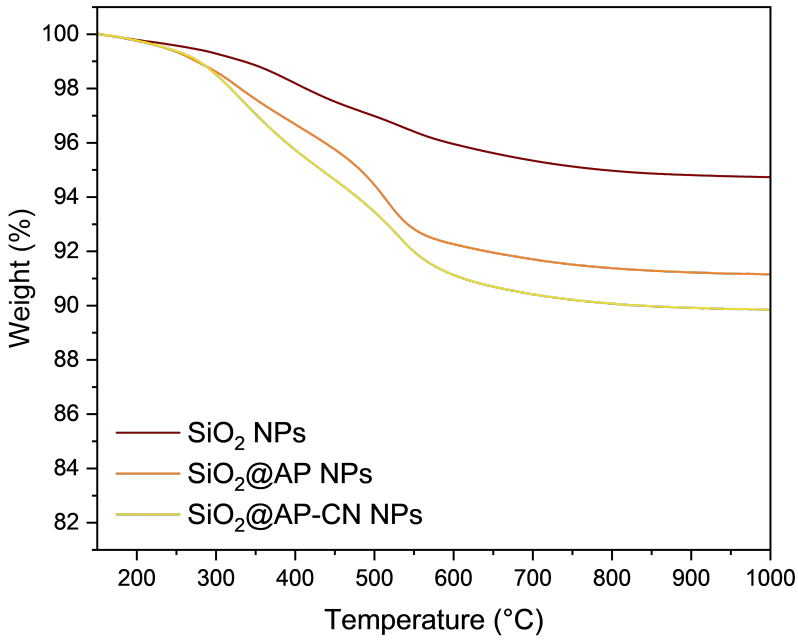

Figure 2.27: TGA curves of SiO_2, SiO_2@AP and SiO_2@AP-CN NPs

Table 2.6: Functionalization degree (both wt.% and σ) of SiO_2@AP and SiO_2@AP-CN NPs

	wt%(Y)	**σ (n./nm^2)**
SiO_2@AP NPs	4.24	1.77
SiO_2@AP-CN NPs	1.30	0.24

CHNS

The CHNS analysis, as shown in Table 2.7, confirmed an increase in the percentage of carbon as the two-step synthesis progressed, consistent with expectations and previous observations in the one-step synthesis. Using Equation A.4 (appendix), the surface coverage (σ) was calculated to be 1.44 n.(APTES)/nm^2 in the SiO_2@AP sample, and 0.42 n.(CN)/nm^2 in the SiO_2@AP-CN sample. These results are in line with those obtained from thermogravimetric analysis, further validating the reliability of the data and

supporting the better efficacy of the one-step strategy.

Table 2.7: CHNS elemental analysis results of SiO_2, SiO_2@AP and SiO_2@AP-CN NPs

Sample	C (wt.%)	H (wt.%)	N (wt.%)	S (wt.%)
SiO_2 NPs	1.18	1.284	0	0.299
SiO_2@AP NPs	3.24	1.465	0.64	0.118
SiO_2@AP-CN NPs	5.02	1.583	0.63	0.163

Additionally, Table 2.7 shows an increase in the percentage of nitrogen atoms from the SiO_2 sample to the SiO_2@AP sample, which is attributed to the functionalization reaction conditions (NH_3) and the amine group in APTES. As expected, subsequent derivatization with CINN-NHS does not significantly affect the nitrogen content on the nanoparticle surface.

2.3.4 Double-step preparation of cinnamyl functionalized fillers using cinnamoyl chloride

The previous sections detailed the development of a new alkoxysilane and its application in the one-step functionalization of two different types of fillers, SiO_2 NPs and Sep NFs. Additionally, the results obtained from the model system, SiO_2 NPs, were compared with a two-step procedure using the same reagents, APTES and CINN-NHS. This comparison clearly demonstrated that the one-step procedure offers a significantly higher yield than the two-step approach, while also preventing the presence of unreacted amine groups, which could pose issues in final applications.

However, the synthesis of CINN-APTES is highly sensitive to environmental

conditions, with even minor contamination from water or moisture causing self-condensation of the silane, thereby rendering it unusable for nanoparticle functionalization. As extensively documented in the literature, an alternative approach would be to employ the two-step procedure. However, as discussed in paragraph 2.3.3, the reaction yield for the method exploiting CINN-NHS derivatives appears very low.

To address this issue, cinnamoyl chloride, a more reactive derivative of cinnamic acid, was selected as an alternative grafting group for modifying the amine groups of APTES that have already anchored onto the filler surface (Scheme 2.6).

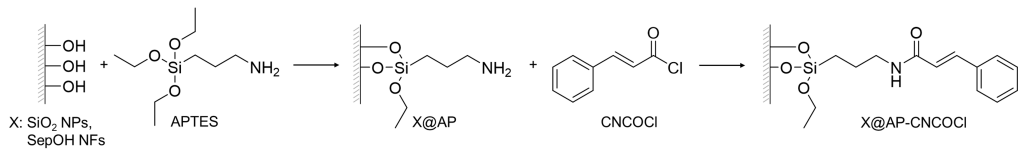

Scheme 2.6: Double-step functionalization reaction of both SiO_2 NPs and SepOH NFs using CNCOCl

2.3.4.1 Experimental Procedure of X@AP-CNCOCl

Step 1: Functionalization of fillers with APTES

–***Silica***

SiO_2 nanoparticles were functionalized with APTES, as outlined in the paragraph 2.3.3, to obtain SiO_2@AP nanoparticles.

–***Sepiolite***

500 mg of SepOH NFs were dispersed in 25 mL of toluene, and the suspension was heated to 130°C under mechanical stirring. Subsequently, 527

μL of APTES was added to the reaction mixture, which was maintained at 130°C for 24 hours. The product was then centrifuged, washed several times with toluene, followed by a final wash with acetone, and dried overnight in an oven at 80°C.[19]

Step 2: Derivatization of the Amino Group of X@AP using cinnamoyl chloride

The nanofiller was dispersed in DCM in a two-neck round-bottom flask using ultrasonication for 2 minutes. Cinnamoyl chloride (CNCOCl was then added to the dispersion, and the reaction mixture was stirred at room temperature for 21 hours. The product (X@AP-CNCOCl) was recovered by centrifugation, washed with DCM, and dried under vacuum for 3 hours. The quantities of the reactants are provided in Table 2.8.

Table 2.8: Quantities of reactants used fot the derivatization of the amino group of X@AP fillers

	SiO_2 NPs		**SepOH NFs**	
X@AP	100.0 mg	0.053 mmol ($R\text{-}NH_2$)	250.0 mg	0.448 mmol ($R\text{-}NH_2$)
CNCOCl	22 mg	0.132 mmol	167.0 mg	1.0 mmol
DCM	10.0 mL		41.0 mL	

2.3.4.2 Characterization of SiO_2@AP-CNCOCl NPs

ATR-FTIR

As in previous cases, the infrared spectrum of the final product was acquired and compared with that of the respective starting materials (Figure

2.28). The starting samples have been thoroughly described in the previous section. For the final sample, new signals appeared in the region between 1700 and 1300 cm^{-1}, likely attributable to the presence of the cinnamic unit.

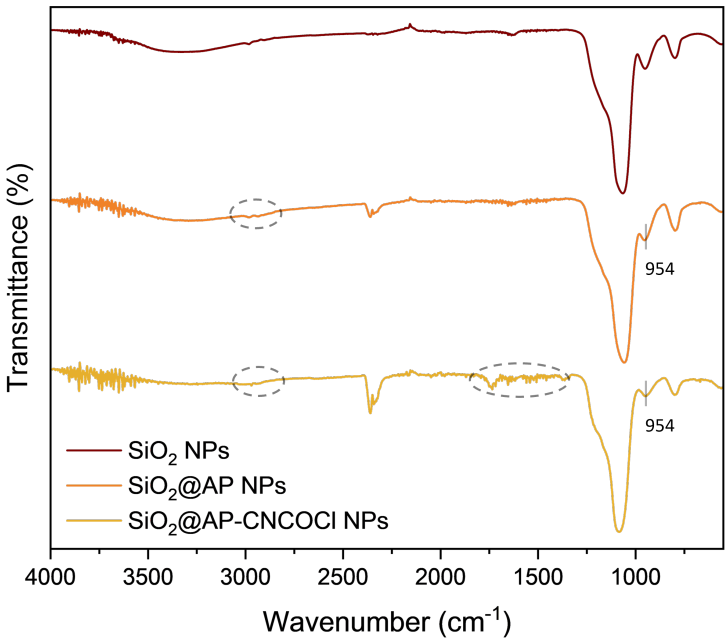

Figure 2.28: ATR-FTIR spectra of SiO_2, SiO_2@AP and SiO_2@AP-CNCOCl NPs

ss-NMR

The ^{29}Si CPMAS NMR spectra of the analyzed samples are shown in the Figure 2.29. The bare silica sample exhibited three resonances corresponding to Q^2, Q^3, and Q^4 units at approximately -90, -99.8, and -108.6 ppm, respectively. After functionalization, T units were observed in both the SiO_2@AP and SiO_2@AP-CNCOCl samples, with T^3 and T^2 units resonating at approximately -65.2 and -59 ppm, respectively, confirming successful

silane anchoring to the silica surface.[13]

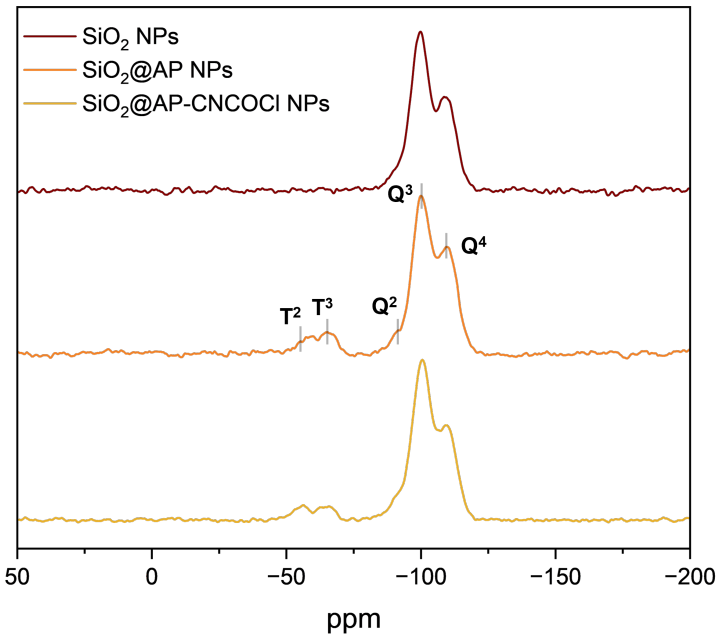

Figure 2.29: ^{29}Si MAS NMR spectra of SiO_2, SiO_2@AP and SiO_2@AP-CNCOCl NPs

The spectra were normalized to the Q^4 signal, revealing a decrease in the intensity of the Q^3 and Q^2 units in SiO_2@AP, which is attributed to APTES grafting. Integration analysis showed that for every 100 Q units, there are 12 T units. Interestingly, in the SiO_2@AP-CNCOCl sample, the Q unit intensities were comparable to those of bare silica. Integration showed that for every 100 Q units, only 9 T units were present, fewer than in the SiO_2@AP sample. This could indicate that during the amine group modification reaction, a small portion of APTES may have been lost.

Figure 2.30 presents the ^{13}C CPMAS NMR spectra of the SiO_2@AP and

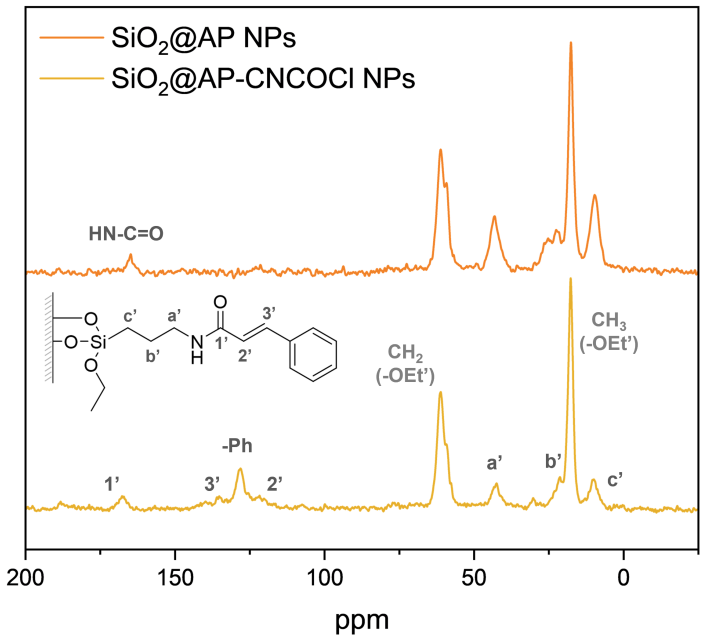

Figure 2.30: ^{13}C CPMAS NMR spectra of SiO_2@AP and SiO_2@AP-CNCOCl NPs

SiO_2@AP-CNCOCl samples. The SiO_2@AP spectrum confirms the successful functionalization of the nanoparticles surface with APTES. Specifically, the silane signals are evident at 9.7 ppm (C-c), 22.6 ppm (C-b), and 43 ppm (C-a). The C-b signal is split into two components at approximately 22.6 and 25.4 ppm, due to its sensitivity to the electronic environment of the terminal nitrogen, which causes a rearrangement in the orientation of the propyl chain (γ-gauche effect).[13, 14] Two additional signals at 17.6 and 61.2 ppm correspond to the non-hydrolyzed ethoxy groups. The peak at 164.8 ppm indicates a reaction between the amine group of APTES and CO_2, a behaviour previously reported in the literature and noted as a reversible phenomenon after heat treatment. Further functionalization with CNCOCl is clearly visible in the spectrum of the SiO_2@AP-CNCOCl sample. The

signal at 168 ppm corresponds to C-1', while the vinyl carbons (C-3' and C-2') are observed at approximately 140 and 121 ppm, respectively. The quaternary carbon and the remaining carbons of the benzene ring resonate at 135 and 128 ppm, respectively.

The carbon at position C-c' experiences a 10 ppm high-field shift, making it the most sensitive to grafting with APTES. Additionally, the C-b' signal is no longer split into two components, indicating the absence of the γ-gauche effect. This behaviour can be explained considering that the terminal nitrogen is now bonded to the cinnamic unit, preventing the rearrangement of the propyl chain.

TGA

Figure 2.31 summarize the thermograms acquired for SiO_2, SiO_2@AP, and SiO_2@AP-CNCOCl NPs. The mass percentage and degree of functionalization of APTES for SiO_2@AP, and the cinnamic units for SiO_2@AP-CNCOCl, were calculated as previously described (Table 2.9).

A key observation is that the degree of functionalization for SiO_2@AP NPs is consistent across both synthesis batches, confirming the reproducibility of the reaction.

In contrast, the degree of functionalization achieved by the two-step procedure using CNCOCl is notably higher than that obtained with CINN-NHS (0.24 n.(CINN)/nm^2). However, when compared to the one-step procedure, it is evident that this strategy remains the most efficient (1.8 n.(CINN)/nm^2).

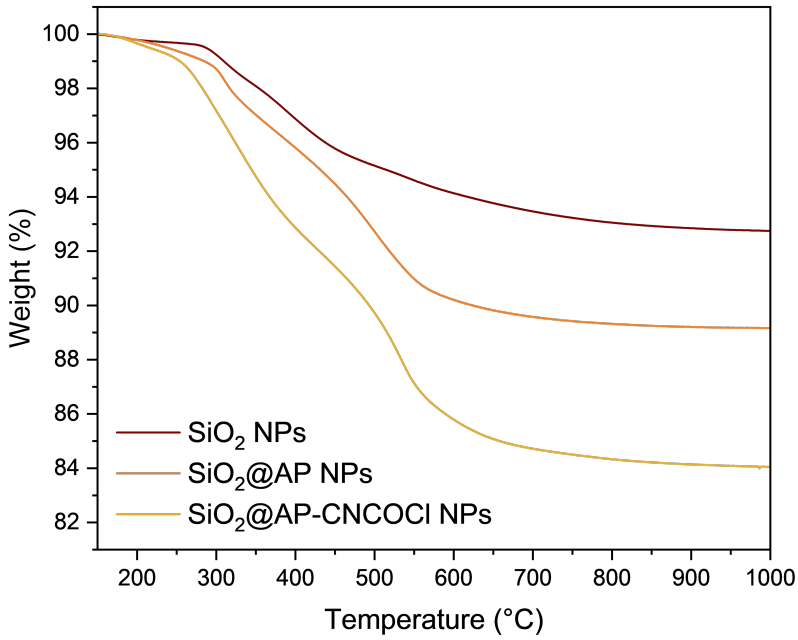

Figure 2.31: TGA curves of of SiO_2, SiO_2@AP and SiO_2@AP-CNCOCl NPs

Table 2.9: Functionalization degree (both wt.% and σ) of SiO_2@AP and SiO_2@AP-CNCOCl NPs

	wt%(Y)	σ **(n./nm²)**
SiO_2@AP NPs	4.21	1.79
SiO_2@AP-CNCOCl NPs	5.14	1.03

CHNS

Elemental analysis shows a clear increase in the relative percentage of carbon atoms as the functionalization steps progress, as expected (Table 2.10). In contrast, the percentage of nitrogen atoms rises in the case of SiO_2@AP, due to the presence of the amine group in APTES and the use of NH_3 during the functionalization process. However, the nitrogen content remains nearly constant in the sample functionalized with the cinnamic unit, since this reaction does not introduce additional N atoms. Using the equations

provided in the appendix, the degree of functionalization was calculated and resulted 1.52 n.(APTES)/nm^2 for SiO_2@AP and 1.14 n.(CNCOCl)/nm^2 for SiO_2@AP-CNCOCl, in line with the results obtained from thermogravimetric analysis.

Table 2.10: CHNS elemental analysis results of SiO_2, SiO_2@AP and SiO_2@AP-CNCOCl NPs

Sample	C (wt.%)	H (wt.%)	N (wt.%)	S (wt.%)
SiO_2	1.52	1.531	0.63	0.085
SiO_2@AP	3.66	1.631	1.75	0.266
SiO_2@AP-CNCOCl	8.26	1.855	1.8	0.294

2.3.4.3 Characterization of SepOH@AP-CNCOCl NFs

ATR-FTIR

The infrared spectra of SepOH, SepOH@AP, and SepOH@AP-CNCOCl nanoparticles are presented in Figure 2.32. The detailed description of the SepOH spectrum can be found in Section 2.3.2.2. Notably, similar to the silica nanoparticles functionalized via the two-step method with CNCOCl, both functionalized sepiolite fibers exhibit weak signals around 3000 cm^{-1}, attributed to the C-H stretching vibrations of alkyl chains or the aromatic ring. Of particular importance are the peaks observed at 1658 and 1619 cm^{-1} in the sample functionalized with the cinnamic unit, corresponding to the stretching of the C=O and conjugated C=C bonds, respectively. Additionally, overlapping in this region is the bending mode of water molecules, which are abundantly present within the channels of the sepiolite structure.

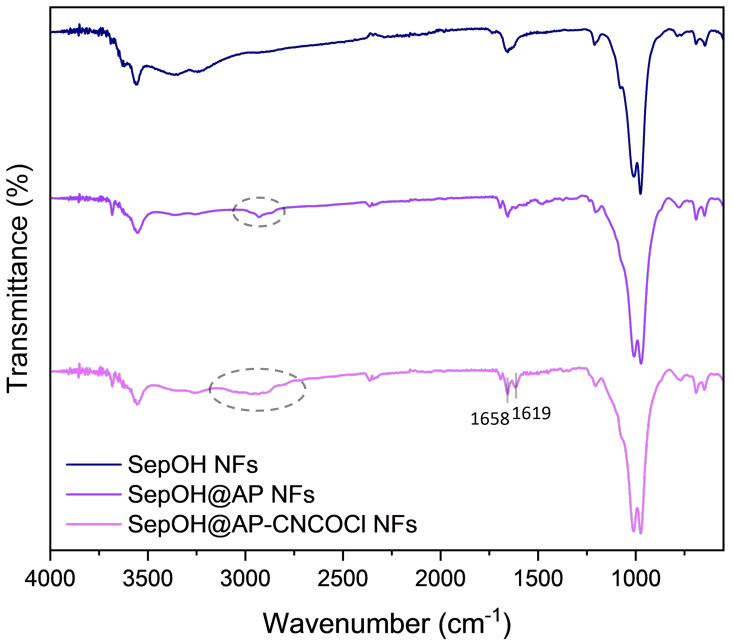

Figure 2.32: ATR-FTIR spectra of SepOH, SepOH@AP and SepOH@AP-CNCOCl NFs

ss-NMR

Figure 2.33 presents the ^{29}Si CPMAS NMR spectra of the samples. All spectra display three distinct resonances at 90, 93, and 96 ppm, corresponding to Q^3 units, which represent the three different Si atom positions in the sepiolite structure (Figure 2. 23).[15] The presence of APTES functionalization is evident in both samples, indicated by the T^3 and T^2 units appearing at approximately 65 and 56 ppm, respectively. Integration analysis revealed a ratio of Q units to T units of around 100:10.

Figure 2.34 displays the ^{13}C CPMAS NMR spectra of SepOH@AP and SepOH@AP-CNCOCl samples. In the SepOH@AP sample, the successful grafting of APTES onto the sepiolite surface is confirmed by peaks at 11

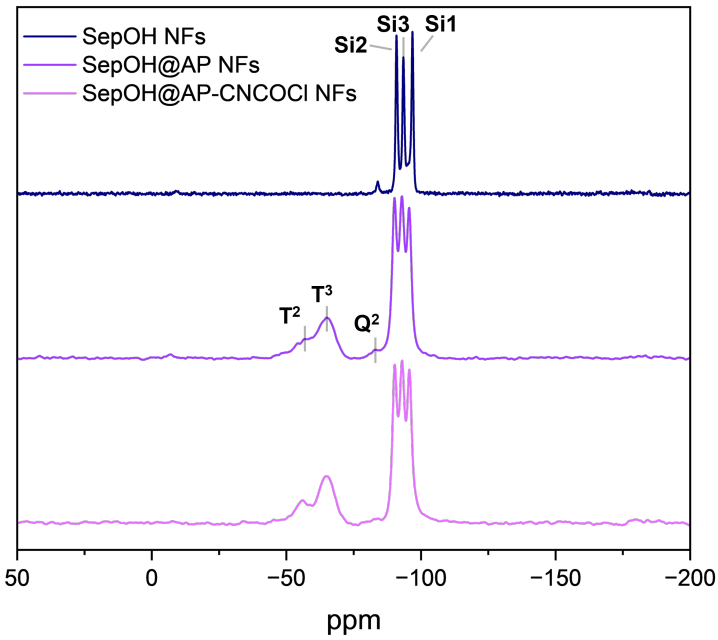

Figure 2.33: ^{29}Si MAS NMR spectra of SepOH, SepOH@AP and SepOH@AP-CNCOCl NFs

ppm (C-c), 22 ppm (C-b), and 43 ppm (C-a), with the C-b peak split due to the γ-gauche effect.[13, 14] Additionally, residual non-hydrolyzed ethoxy groups were observed, along with a peak at 165 ppm, indicating the reaction of APTES with CO_2.[17, 18]

For the SepOH@AP-CNCOCl sample, the further functionalization with cinnamoyl chloride was successful, as evidenced by signals corresponding to the cinnamoyl unit: 167 ppm (C-1'), 140 ppm (C-2'), 122 ppm (C-3'), and 135 ppm (C-Ph). The disappearance of the splitting in the C-b' signal suggests that the NH_2 groups no longer interact with surface silanols after the second functionalization step, eliminating the γ-gauche effect.

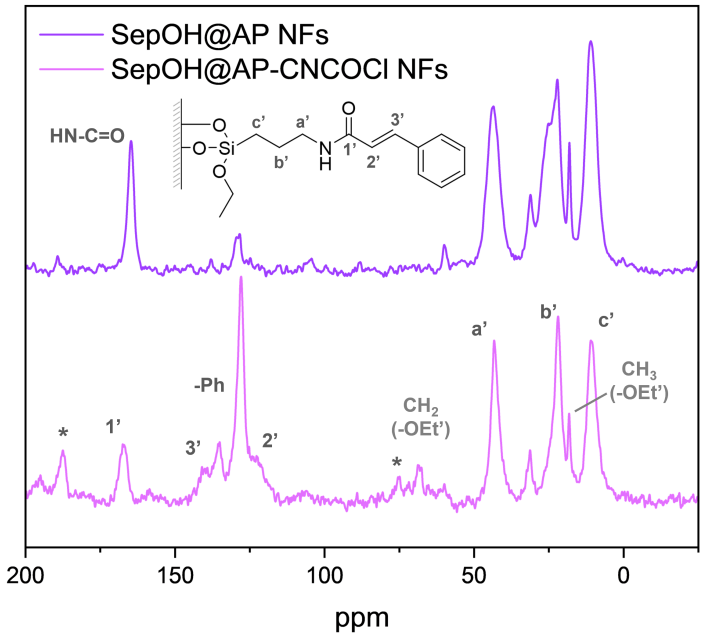

Figure 2.34: ^{13}C CPMAS NMR spectra of SepOH@AP and SepOH@AP-CNCOCl NFs

TGA

The thermograms of SepOH, SepOH@AP, and SepOH@AP-CNCOCl NFs samples are reported in Figure 2.35. TGA was performed to estimate the amount of functionalizing agent grafted onto the nanofiber surfaces after confirming the success of the functionalization reaction. As described earlier for SepOH@CN, the mass loss between 150°C and 1000°C cannot be solely attributed to the decomposition of the functionalizing agent. Nonetheless, an estimation of the degree of functionalization is provided in Table 2.11.

A key remark is that the estimated degree of functionalization for SepOH@AP is significantly higher than that of SepOH@CN (from the one-step procedure). One possible explanation is that the shorter APTES unit may more

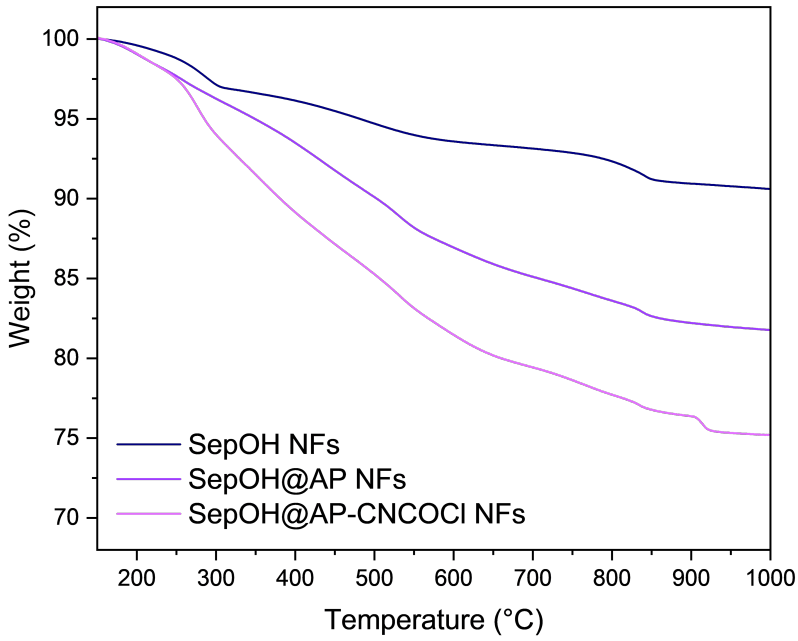

Figure 2.35: TGA curves of SepOH, SepOH@AP and SepOH@AP-CNCOCl NFs

easily penetrate the sepiolite channels, becoming adsorbed or even covalently bound within the porous internal structure.

Table 2.11: Functionalization degree (both wt.% and σ) of SepOH@AP and SepOH@AP-CNCOCl NFs

	wt%(Y)	σ **(n./nm^2)**
SepOH@AP NFs	10.41	5.23
SepOH@AP-CNCOCl NFs	6.53	1.58

CHNS

Elemental analysis once again reveals a progressive increase in the percentage of carbon atoms as the reaction steps advance (Table 2.12). As expected, the percentage of nitrogen atoms increases during the first step, due to the

amine group of APTES, and remains almost unchanged after the attachment of the cinnamic unit. Using the equations provided in the appendix, the degrees of functionalization were calculated as 7.60 n.(APTES)/nm^2 for SepOH@AP NFs and 2.59 n.(CNCOCl)/nm^2 for SepOH@AP-CNCOCl NFs. In this case, unlike the previous results, the TGA and CHNS measurements show some discrepancies. This difference could be attributed to the fact that the degree of functionalization calculated by TGA is based on data obtained at temperatures above 150°C, whereas in the case of CHNS, the mass loss over the entire temperature range is considered. Given the porous structure of the material, it is possible that solvent and adsorbed substances on the surface are accounted in the CHNS analysis, leading to an overestimation of the results.

Table 2.12: CHNS elemental analysis results of SepOH, SepOH@AP and SepOH@AP-CNCOCl NFs

Sample	C (wt.%)	H (wt.%)	N (wt.%)	S (wt.%)
SepOH	0.48	1.722	0.66	0.198
SepOH@AP	9.47	2.184	1.36	0
SepOH@AP-CNCOCl	11.52	2.354	1.21	0

DRS – Photoresponsive properties

DRS spectra of both cinnamic-functionalized fillers were acquired to assess the absorption properties of the samples (Figure 2.36, Figure 2.37). Additionally, both powders were irradiated at 365 nm for 24 hours, followed by exposure to 254 nm for another 24 hours, to evaluate their photoresponsive behavior.

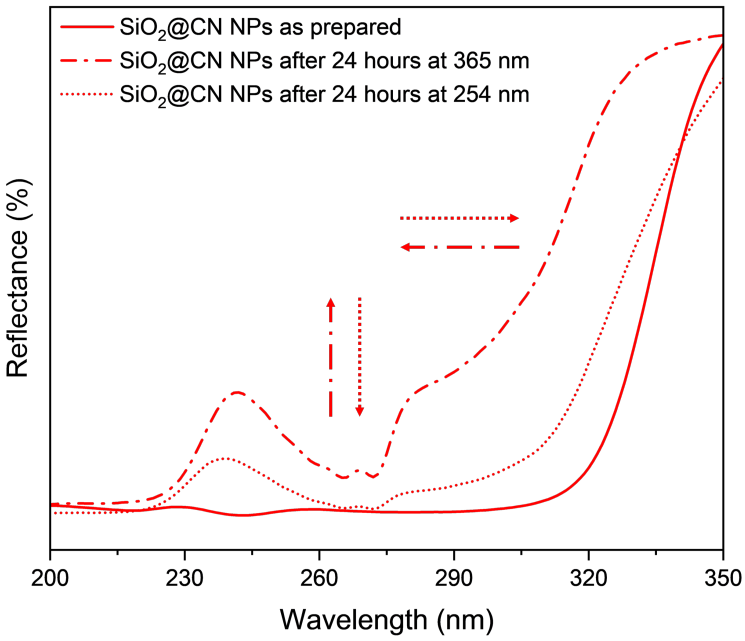

Figure 2.36: DRS spectra of SiO_2@CN NPs in three conditions: as-prepared, after 24 hours of irradiation at 365 nm, and following an additional 24 hours of irradiation at 254 nm

Both SiO_2@CN and SepOH@CN functionalized fillers exhibited similar photoreversible characteristics. Upon UV irradiation at $\lambda \geq 365$ nm, corresponding to the photodimerization step, an increase in reflectance intensity was observed. Since transmittance is assumed to be zero, an increase in reflectance corresponds to a decrease in absorbance. This change is attributed to the conversion of the vinyl aryl groups in the cinnamic units into cyclobutane structures, disrupting the π-conjugation (Scheme 2.7).

After irradiation at $\lambda = 254$ nm, photocleavage occurs, partially reversing the changes. The reflectance intensity decreases, indicating a partial recovery of the original absorption properties and a return to the cinnamic structure.

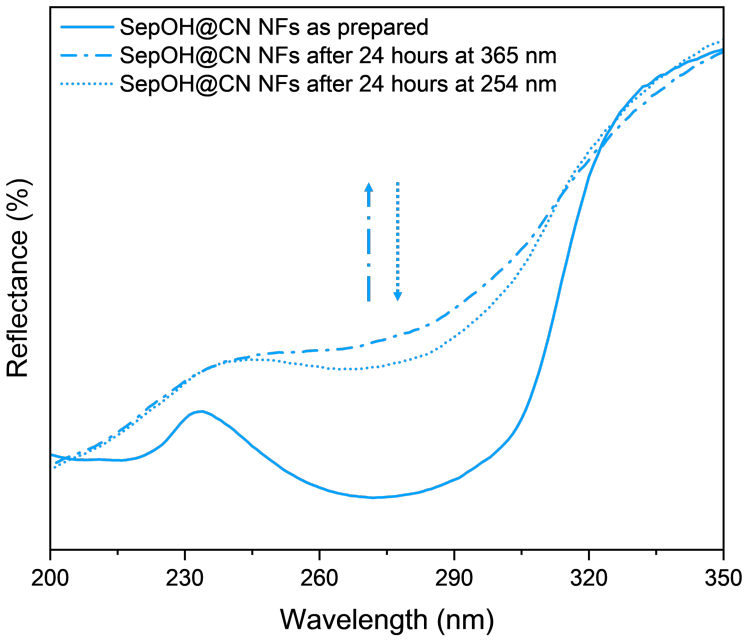

Figure 2.37: DRS spectra of SepOH@CN NFs in three conditions: as-prepared, after 24 hours of irradiation at 365 nm, and following an additional 24 hours of irradiation at 254 nm

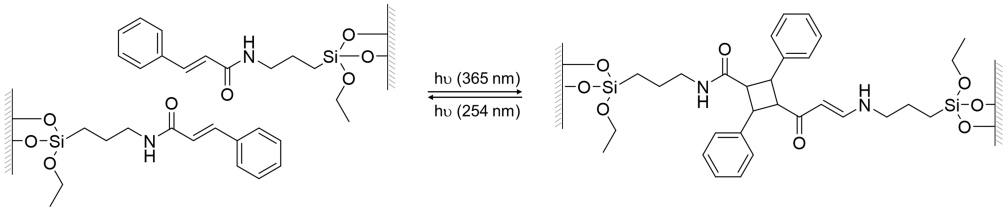

Scheme 2.7: Photoreversible dimeriation scheme of CINN-APTES grafted on filler surface

However, as observed in both SiO_2@CN and SepOH@CN, this recovery is incomplete, with the initial spectral features only partially restored. This incomplete regeneration is likely due to an equilibrium between photodimerization and photocleavage processes occurring on the nanoparticle surfaces. Furthermore, photoinduced cluster formation may occur, especially within

the cross-linked cinnamic units between nanoparticles, creating shielding effects that prevent full UV light exposure and limit the reversal of cyclobutane back to the vinyl aryl state.[20, 21]

2.4 Exploitation of another light-responsive unit: coumarin

This paragraph focuses on the functionalization of silica nanoparticles with coumarin, a well-known chromophore that undergoes photoreactions, making it an ideal candidate for developing light-responsive materials. The process begins with the synthesis of acrylic coumarin (AC), which is then attached to silica nanoparticles in a multi-step procedure using MPTMS.[22] The approach involves a radical reaction between the acrylic group of the coumarin and the methacrylic group of MPTMS, enabling the covalent attachment of coumarin units onto the silica surface. The successful grafting of coumarin is confirmed through solid-state NMR (ss-NMR) and DRS spectroscopy, which show enhanced light absorption in the UV-visible range, consistent with coumarin's known photoreactivity. The characterization results highlight the potential of this functionalized filler for light-induced applications, such as responsive coatings and other smart material technologies.

2.4.1 Preparation of Coumarine functionalized SiO_2 NPs

Materials

7-Hydroxy-4-methylcoumarin 98% (HMC) and Toluene (99%) was purchased from Alfa Aesar. Acryloyl Chloride 97% and Dicumyl Peroxide 98% (DCP) were purchased from Sigma-Aldrich and used as received. MPTMS 97% was purchased from abcr. Sodium hydroxide 98% (NaOH) was purchased from Thermo Fisher Scientific. Absolute anhydrous Ethanol was purchased from VWR.

2.4.1.1 Experimental Procedure of SiO_2@MP-AC

Step 1: Synthesis of Acrylic Coumarine

Acrylic coumarin (AC) was synthesized using a method reported in the literature (Scheme 2.8). Specifically, 2.17 g of 7-hydroxy-4-methylcoumarin and 0.5 g of NaOH were placed in a round-bottom flask containing 100 mL of ethanol. The mixture was heated to 70°C and stirred for 30 minutes. Subsequently, the reaction was cooled to 0-5°C, and 1.12 mL of acryloyl chloride was slowly added dropwise, allowing the reaction to proceed for an additional 60 minutes at 0-5°C. The reaction mixture was then poured into a beaker containing 200 mL of cold distilled water, and the precipitated product was filtered, washed with cold distilled water, and dried in a vacuum oven at 50°C. ^{1}H NMR (400.13 MHz, DMSO-d6): δ 7.85 (d, J = 8.64 Hz, ^{1}H), 7.35 (d, J = 2.28 Hz, ^{1}H), 7.25 (dd, J = 8.64, 2.28 Hz, ^{1}H), 6.58 (dd, J = 17.24, 1.24 Hz, ^{1}H), 6.43 (m, 2H), 6.20 (dd, J = 10.32, 1.24 Hz, ^{1}H); 2.44 (d, J = 1.12 Hz, 3H). NMR data are consistent with the literature data.[23]

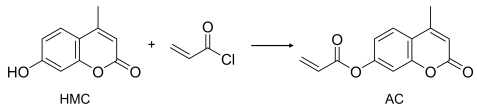

Scheme 2.8: Preparation of AC

Step 2: Functionalization of silica with MPTMS

In a 50 mL round-bottom flask 1.0 g of SiO_2 was dispersed in 24 mL of toluene, and the resulting suspension was heated to 130°C under mechanical stirring. After reaching the desired temperature, 1.12 mL of MPTMS was added to the reaction mixture, which was then kept at 130°C for 24

hours. The product was isolated by centrifugation, washed multiple times with toluene, followed by a final wash with ethanol, and then dried overnight in an oven at 80°C (Scheme 2.9).

Step 3: Modification of SiO_2@MP with AC

20 mg of AC was dissolved in 10 mL of toluene, and 500 mg of the previously synthesized SiO_2@MP NPs were dispersed in the solution. The mixture was heated to 170°C, and upon reaching the target temperature, a solution of 20 mg of DCP (4 wt.% with respect to SiO_2) in 2 mL of toluene was added. The reaction was stirred at 170°C overnight. The product was then centrifuged and washed three times with toluene, followed by a final wash with ethanol. The powder was dried overnight in an oven at 80°C (Scheme 2.9).

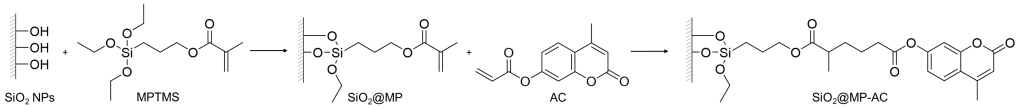

Scheme 2.9: Double-step functionalization reaction of SiO_2 NPs using AC

2.4.1.2 Characterization of SiO_2@MP-AC

UV-Vis

To verify the chromophore properties of the acrylic coumarin sample, its UV-Vis spectrum was recorded with the molecule dissolved in DCM. The spectrum, shown in the Figure 2.38, reveals two main absorption peaks at 275 nm and 315 nm, confirming the molecule's strong absorption in the UV-Vis range.[12] These peaks demonstrate the characteristic light absorption properties of acrylic coumarin, which are essential for its functionality in

light-responsive applications.

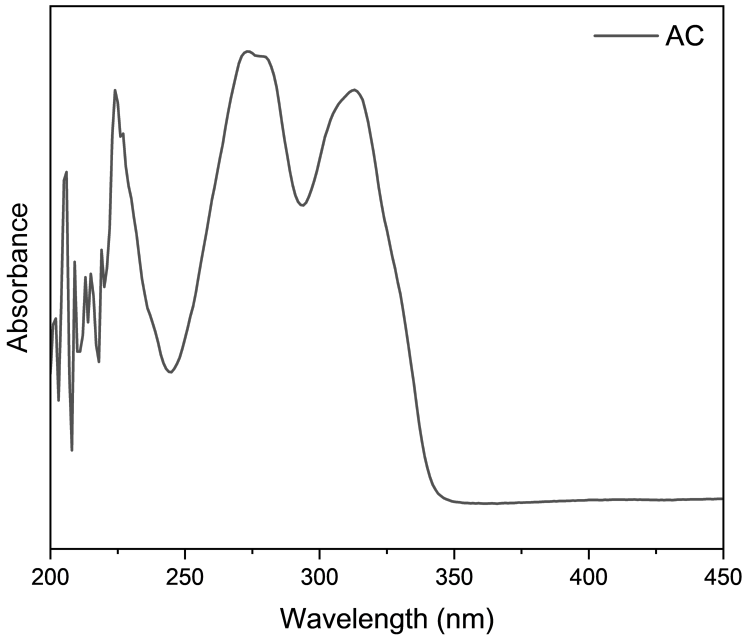

Figure 2.38: UV-Vis spectrum of AC

ss-NMR

Figure 2.39 shows the ^{29}Si NMR CPMAS spectra of the SiO_2, SiO_2@MP, and SiO_2@MP-AC NPs samples. The spectrum of SiO_2 exhibits the characteristic asymmetric line shape resulting from three components assigned to the structural units Q^2, Q^3, and Q^4. These units are present in all samples, although the functionalized samples show a slightly lower amount of Q^4. The spectra of functionalized SiO_2 display T^1 and T^2 units at 46 and 55 ppm, respectively, indicating silane grafting. The absence of T^3 units suggests a very low degree of condensation of MPTMS.

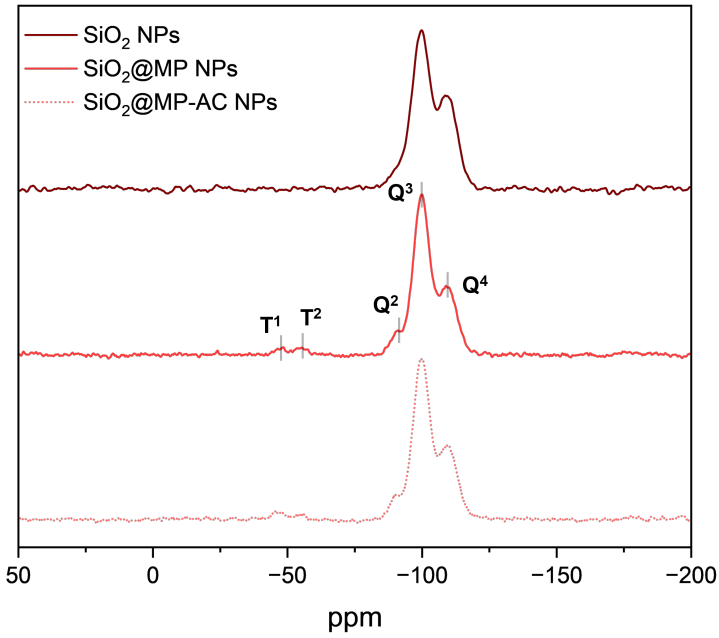

Figure 2.39: ^{29}Si NMR CPMAS spectra of the SiO_2, SiO_2@MP, and SiO_2@MP-AC NPs

Figure 2.40 presents the ^{13}C CPMAS spectra of silica functionalized first with MPTMS and subsequently with AC molecules.

In the spectrum of the SiO_2@MP sample, the organic chain is represented by three resonances corresponding to the methylene carbon atoms of the propyl chain (C-1, C-2, C-3) and three resonances of the methacrylate tail: the carbonyl (C-4 at 169 ppm), vinyl (C-5 and C-6 at 137 and 124 ppm, respectively), and methyl (C-7) carbon atoms.[24] The peak at 50 ppm can be attributed to unhydrolyzed -OCH_3 groups, while the signal at 55 ppm is assigned to a CH_2 carbon involved in an ethoxy group, according to the literature. Since the particles were washed with ethanol, it is possible that some solvent molecules remain adsorbed on the sample surface. Additionally, the

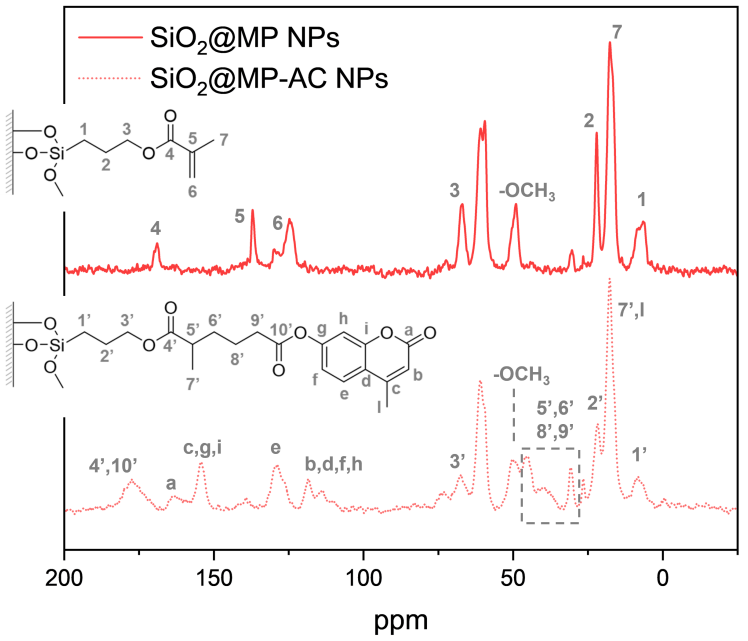

Figure 2.40: ^{13}C CPMAS NMR spectra of SiO_2@MP and SiO_2@MP-AC NPs

shape and chemical shift from 1 to about 6 ppm suggest a low degree of condensation.

The spectrum of the SiO_2@MP-AC sample shows signals corresponding to both the MPTMS and AC components, with the AC resonances visible in the 100-160 ppm region. The binding between the two components is evidenced by the appearance of new resonances in the methylene region at 30-50 ppm, as well as the disappearance of the vinyl peaks (C-5, C-6) and the broadening and downfield shift of C-4.[22, 25] These results confirm the successful functionalization of silica nanoparticles with coumarin units.

TGA

Thermogravimetric analysis was employed to estimate the degree of func-

tionalization. As in previous cases, the equations provided in the appendix were used to obtain the results presented in the Table 2.13.

Table 2.13: Functionalization degree (both wt.% and σ) of SiO_2@MP and SiO_2@MP-AC NPs

	wt%(Y)	σ **(n./nm^2)**
SiO_2@MP NPs	2.90	0.56
SiO_2@MP-AC NPs	3.29	0.36

It can be observed that, consistent with the ss-NMR analysis, the degree of functionalization with MPTMS is relatively low. However, the subsequent reaction with AC successfully functionalized more than 50% of the available methacrylate groups. It is evident that the functionalization reaction with MPTMS requires optimization. Additionally, it must be noted that the chemistry involved in this process relies on radical reactions. Therefore, the structure depicted in the diagram may be a simplified representation of the actual situation. It is possible that methacrylate groups of MPTMS could react with each other, or that coumarin units may also react among themselves, forming oligomeric chains of coumarin units, which are subsequently bound to the nanoparticle surface.

DRS

DRS analysis was conducted as a preliminary step to assess the absorption properties of nanoparticles functionalized with coumarin units. The spectra of SiO_2@MP and SiO_2@MP-AC nanoparticles are presented in Figure 2.41. The methacrylate group exhibits weak absorption around 270 nm. However, the addition of the coumarin unit, even with a relatively low degree of

functionalization, significantly enhances the absorption, displaying a band starting at 330 nm and a second peak at 275 nm, consistent with the UV-Vis absorption of the coumarin unit (Figure 2.38). Ongoing irradiation measurements will further evaluate the material's photoresponsive behaviour, which could lead to the development of a new reactive filler. Once optimized, this approach will also be applied to sepiolite nanofibers, as previously explored with cinnamic-functionalized systems.

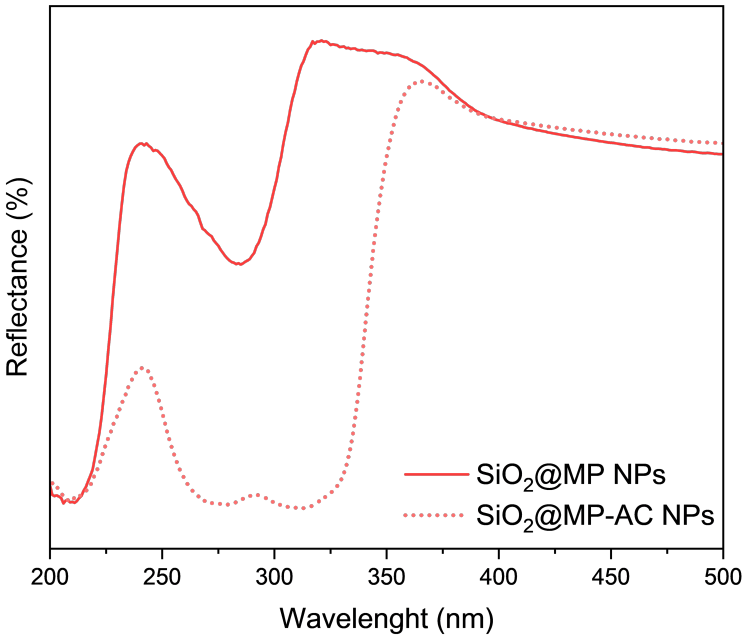

Figure 2.41: DRS spectra of SiO_2@MP and SiO_2@MP-AC NPs

References

(1) Stöber, W.; Fink, A.; Bohn, E. Controlled growth of monodisperse silica spheres in the micron size range. *Journal of Colloid and Interface Science* **1968**, *26*, 62–69, DOI: 10.1016/0021-9797(68)90272-5.

(2) Ciriminna, R.; Fidalgo, A.; Pandarus, V.; Béland, F.; Ilharco, L. M.; Pagliaro, M. The Sol-Gel Route to Advanced Silica-Based Materials and Recent Applications. *Chemical Reviews* **2013**, *113*, 6592–6620, DOI: 10.1021/cr300399c.

(3) Tripaldi, L.; Callone, E.; D'Arienzo, M.; Dirè, S.; Giannini, L.; Mascotto, S.; Meyer, A.; Scotti, R.; Tadiello, L.; Credico, B. D. Silica hairy nanoparticles: a promising material for self-assembling processes. *Soft Matter* **2021**, *17*, 9434–9446, DOI: 10.1039/D1SM01085A.

(4) Thommes, M.; Kaneko, K.; Neimark, A. V.; Olivier, J. P.; Rodriguez-Reinoso, F.; Rouquerol, J.; Sing, K. S. W. Physisorption of gases, with special reference to the evaluation of surface area and pore size distribution (IUPAC Technical Report). *Pure and Applied Chemistry* **2015**, *87*, 1051–1069, DOI: 10.1515/pac-2014-1117.

(5) Ruiz, A. I.; Ruiz-García, C.; Ruiz-Hitzky, E. From old to new inorganic materials for advanced applications: The paradigmatic example of the sepiolite clay mineral. *Applied Clay Science* **2023**, *235*, 106874, DOI: 10.1016/j.clay.2023.106874.

(6) Miura, A.; Nakazawa, K.; Takei, T.; Kumada, N.; Kinomura, N.; Ohki, R.; Koshiyama, H. Acid-, base-, and heat-induced degradation behavior of Chinese sepiolite. *Ceramics International* **2012**, *38*, 4677–4684, DOI: 10.1016/j.ceramint.2012.02.050.

(7) Galan, E. Properties and applications of palygorskite-sepiolite clays. *Clay Minerals* **1996**, *31*, 443–453, DOI: 10.1180/claymin.1996.031.4.01.

(8) Alvarez, A. In *Developments in Sedimentology*; Elsevier: 1984; Vol. 37, pp 253–287, DOI: 10.1016/S0070-4571(08)70044-X.

(9) Kozlov, M. V.; Konduktorov, K. A.; Shcherbakova, A. S.; Kochetkov, S. N. Synthesis of *N*'-propylhydrazide analogs of hydroxamic inhibitors of histone deacetylases (HDACs) and evaluation of their impact on activities of HDACs and replication of hepatitis C virus (HCV). *Bioorganic & Medicinal Chemistry Letters* **2019**, *29*, 2369–2374, DOI: 10.1016/j.bmcl.2019.06.006.

(10) (3-Aminopropyl)triethoxysilane - Optional[1H NMR] - Spectrum - SpectraBase https://spectrabase.com/spectrum/KqRif55XR4b.

(11) N-hydroxysuccinimide - Optional[1H NMR] - Spectrum - SpectraBase https://spectrabase.com/spectrum/K7yFKTKEAfy.

(12) Jellali, R.; Bertrand, V.; Alexandre, M.; Rosière, N.; Grauwels, M.; De Pauw-Gillet, M.-C.; Jérôme, C. Photoreversibility and Biocompatibility of Polydimethylsiloxane-Coumarin as Adjustable Intraocular Lens Material. *Macromolecular Bioscience* **2017**, *17*, 1600495, DOI: 10.1002/mabi.201600495.

(13) Mostoni, S.; D'Arienzo, M.; Di Credico, B.; Armelao, L.; Rancan, M.; Dirè, S.; Callone, E.; Donetti, R.; Susanna, A.; Scotti, R. Design of a Zn Single-Site Curing Activator for a More Sustainable Sulfur Cross-Link Formation in Rubber. *Industrial & Engineering Chemistry Research* **2021**, *60*, 10180–10192, DOI: 10.1021/acs.iecr.1c01580.

(14) Calovi, M.; Callone, E.; Ceccato, R.; Deflorian, F.; Rossi, S.; Dirè, S. Effect of the Organic Functional Group on the Grafting Ability of Trialkoxysilanes onto Graphene Oxide: A Combined NMR, XRD, and ESR Study. *Materials (Basel, Switzerland)* **2019**, *12*, 3828, DOI: 10.3390/ma12233828.

(15) Bugnotti, D.; Dalle Vacche, S.; Esposito, L. H.; Callone, E.; Orsini, S. F.; Ceccato, R.; D'Arienzo, M.; Bongiovanni, R.; Dirè, S.; Vitale, A. Structure of Starch-Sepiolite Bio-Nanocomposites: Effect of Processing and Matrix-Filler Interactions. *Polymers* **2023**, *15*, 1207, DOI: 10.3390/polym15051207.

(16) Walczyk, A.; Karcz, R.; KryŚciak-Czerwenka, J.; Napruszewska, B. D.; Duraczyńska, D.; Michalik, A.; Olejniczak, Z.; Tomczyk, A.; Klimek, A.; Bahranowski, K.; Serwicka, E. M. Influence of Dry Milling on Phase Transformation of Sepiolite upon Alkali Activation: Implications for Textural, Catalytic and Sorptive Properties. *Materials* **2020**, *13*, 3936, DOI: 10.3390/ma13183936.

(17) Vilarrasa-García, E.; Cecilia, J.; Moura, P. A.; Azevedo, D.; Rodriguez-Castellon, E. Assessing CO2 Adsorption on Amino-Functionalized Mesocellular Foams Synthesized at Different Aging Temperatures. *Frontiers in Chemistry* **2020**, *8*, DOI: 10.3389/fchem.2020.591766.

(18) Cueto-Díaz, E. J.; Castro-Muñiz, A.; Suárez-García, F.; Gálvez-Martínez, S.; Torquemada-Vico, M. C.; Valles-González, M. P.; Mateo-Martí, E. APTES-Based Silica Nanoparticles as a Potential Modifier for the Selective Sequestration of CO2 Gas Molecules. *Nanomaterials* **2021**, *11*, 2893, DOI: 10.3390/nano11112893.

(19) Letaief, S.; Grant, S.; Detellier, C. Phenol acetylation under mild conditions catalyzed by gold nanoparticles supported on functional pre-acidified sepiolite. *Applied Clay Science* **2011**, *53*, 236–243, DOI: 10.1016/j.clay.2011.01.023.

(20) Jadhav, T.; Fang, Y.; Liu, C.-H.; Dadvand, A.; Hamzehpoor, E.; Patterson, W.; Jonderian, A.; Stein, R. S.; Perepichka, D. F. Transformation between 2D and 3D Covalent Organic Frameworks via Reversible [2 + 2] Cycloaddition. *Journal of the American Chemical Society* **2020**, *142*, 8862–8870, DOI: 10.1021/jacs.0c01990.

(21) Thipperudrappa, J.; Raghavendra, U. P.; Basanagouda, M. Photophysical characteristics of biologically active 4-aryloxymethyl coumarins 4PTMBC and 1IPMBC. *Spectrochimica Acta Part A: Molecular and Biomolecular Spectroscopy* **2015**, *136*, 1475–1483, DOI: 10.1016/j.saa.2014.10.039.

(22) Mirizzi, L.; D'Arienzo, M.; Nisticò, R.; Fredi, G.; Diré, S.; Callone, E.; Dorigato, A.; Giannini, L.; Guerra, S.; Mostoni, S.; Di Credico, B.; Scotti, R. Al2O3 decorated with polyhedral silsesquioxane units: An unconventional filler system for upgrading thermal conductivity and mechanical properties of rubber composites. *Composites Science and Technology* **2023**, *236*, 109977, DOI: 10.1016/j.compscitech.2023.109977.

(23) Patel, J. R.; Patel, K. H.; Patel, R. M. Reactivity ratio of novel acrylic copolymer by NMR spectroscopy. *Colloid and Polymer Science* **2009**, *287*, 89–95, DOI: 10.1007/s00396-008-1943-6.

(24) D'Arienzo, M.; Dirè, S.; Cobani, E.; Orsini, S.; Di Credico, B.; Antonini, C.; Callone, E.; Parrino, F.; Dalle Vacche, S.; Trusiano, G.; Bongiovanni, R.; Scotti, R. SiO2/Ladder-Like Polysilsesquioxanes Nanocomposite Coatings: Playing with the Hybrid Interface for Tuning Thermal Properties and Wettability. *Coatings* **2020**, *10*, 913, DOI: 10.3390/coatings10100913.

(25) 7-Hydroxy-4-methyl-coumarin - Optional[13C NMR] - Spectrum - SpectraBase https://spectrabase.com/spectrum/1GJm4JtTUIt.

Chapter 3

Preparation of light-responsive yuca starch

This chapter describes the synthesis, characterization, and evaluation of a novel photo-responsive etherified starch material derived from yuca starch This research was conducted in collaboration with Dr. Simona Petroni and Prof. Laura Cipolla, with whom the final results were shared.

The modification was carried out through an etherification reaction with cinnamyl chloride, aiming to improve the properties of native starch and introduce functional groups able to confer light-responsive behaviour. The chapter details the experimental procedures used for etherification, degree of substitution analysis, film formation, and characterization of the modified starch, as well as the evaluation of its thermal stability and photo-responsive properties.

The characterization of the modified starch was conducted using several analytical techniques. ATR-FTIR, solution-state, and solid-state NMR provided evidence for the formation of ether bonds between starch and cinnamyl chloride. Thermogravimetric analysis showed enhanced thermal stability with increasing Degree of Substitution (DS).

The photo-responsive properties of the modified starch were investigated using UV-Vis and ^{1}H-NMR spectroscopy. These analyses revealed partial photodimerization and isomerization of cinnamyl moieties in solution.

Overall, the chapter provides a comprehensive overview of the synthesis, characterization, and functional analysis of cinnamyl etherified yuca starch, emphasizing the material's photoresponsive properties.

3.1 Experimental Procedure

Starch is a biopolymer that stands out for its versatility, biodegradability, and abundance. Particularly when derived from organic waste or food industry surplus, starch supports the principles of the circular economy by reducing waste and encouraging the reuse of materials that contribute to environmental challenges.[1]

Chemically, starch is a polysaccharide composed of two main components: amylose and amylopectin. Amylose is a linear polymer made up of α-D-glucose units linked by $\alpha(1\rightarrow4)$ glycosidic bonds, which contributes to starch's film-forming abilities. Amylopectin, a highly branched polymer, contains $\alpha(1\rightarrow4)$ linked glucose units with $\alpha(1\rightarrow6)$ linkages at the branching points, contributing to its structure (Figure 3.1). The abundance of hydroxyl (-OH) groups in starch gives it a hydrophilic nature but also provides sites for chemical modifications, such as crosslinking or grafting, to improve its performance.[2]

Cassava (yuca) starch, in particular, has emerged as a promising raw material for bioplastic production due to the sustainable practices associated with its cultivation. Cassava is resilient in arid climates, requiring minimal agricultural inputs, making it an ecologically sound crop. Its high amylose content enhances its capacity to form strong, durable films, which is crucial for packaging applications. Additionally, cassava starch has a relatively low gelatinization temperature (55°C to 75°C), which reduces energy consumption during processing, making it more efficient for industrial-scale production.[3]

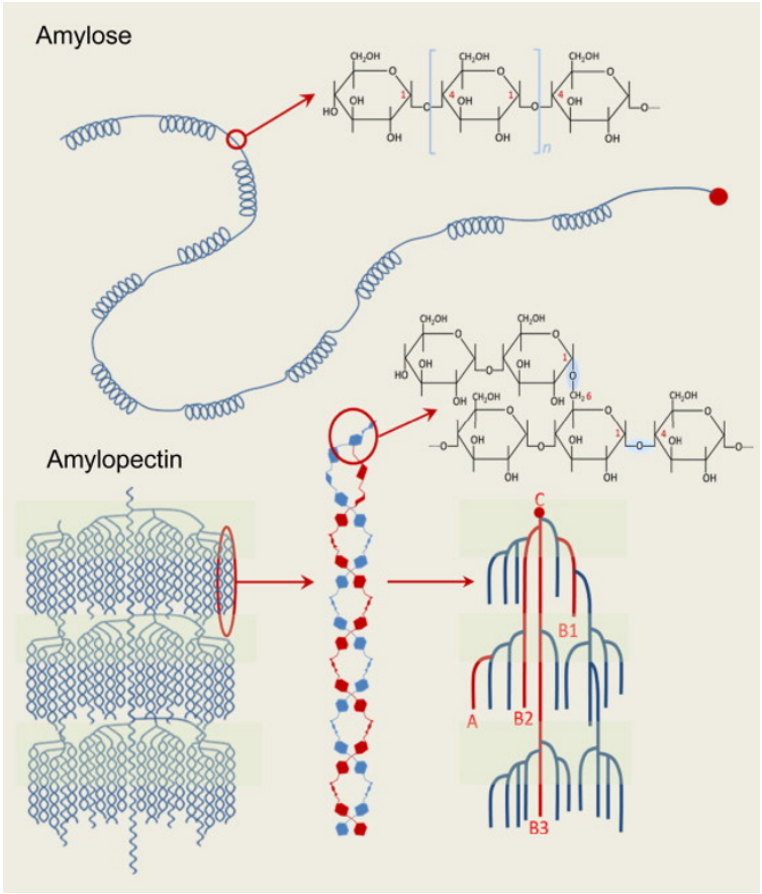

Figure 3.1: Amylose and amylopectin structures[2]

Despite these advantages, starch has inherent limitations, including high hydrophilicity, low thermal stability, and inadequate mechanical strength, which can limit its use in certain applications like food packaging. To overcome these challenges, two primary modification strategies are often employed. Crosslinking is an effective method for improving the mechanical strength, water resistance, and thermal stability of starch-based materials.[4–6] Incorporating natural nanofillers, such as silicates (e.g., sepiolite, palygorskite, montmorillonite, and kaolinite), into starch matrices can significantly create a tortuous path that impedes the diffusion of gases and

moisture, thereby improving the water resistance and overall strength of starch-based films.[1]

In conclusion, starch, particularly yuca starch, emerges as a promising biobased polymer for packaging applications due to its biodegradability, availability, and cost-effectiveness. Its properties can be improved through crosslinking and the incorporation of nanofillers. The development of starch-based nanocomposites aligns with global efforts to reduce environmental pollution and promote a circular economy.

Materials

Yuca (cassava) starch powder sourced from Colombia (Almidón de Yuca Dulce, produced by Cimpa s.a.s.) was previously dried in a static oven at 65°C for 48 hours. Cinnamyl chloride 95% (CINN-Cl), NaOH (pellets, purity $\geq$ 98%), and THF $\geq$ 99.9% were obtained from Sigma-Aldrich and used without further purification. Acetone 96.6% was sourced from Thermo Fisher Scientific. Anhydrous Dimethyl Sulfoxide (DMSO) was purchased from VWR International. DMSO-d6 (99.5% atom D) and trifluoroacetic acid-d (TFA-d, 99.5% atom D) for NMR spectroscopy were obtained from Acros Organics.

3.1.1 Etherification of yuca starch with cinnamyl chloride

Three different starch/NaOH/cinnamyl chloride ratios were used to obtain varying degrees of substitution (Table 3.1). The ratios were calculated based on the mmol of anhydroglucose units (AGU, MW = 162.14 g/mol).

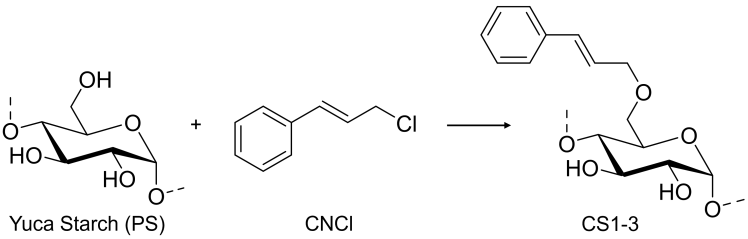

Scheme 3.1: Etherification of yuca starch with cinnamyl chloride

Yuca starch (1 g, 6.16 mmol AGU) was suspended in 16 mL of dry DMSO in a round-bottom flask and heated to 90°C with magnetic stirring until dissolved (approximately 3 hours). The solution was then cooled to room temperature, and a specific amount of previously powdered NaOH was added to the reaction mixture, which was then stirred vigorously for 1 hour. Subsequently, cinnamyl chloride was added dropwise, and the reaction mixture was stirred for 24 hours at room temperature. The solution was transferred to a beaker containing 30 mL of acetone, placed in an ice bath. The product precipitated as a white powder, which was then centrifuged and washed once with a cold solution of acetone and water (3:1), followed by several washes with fresh cold acetone. The powders were dried under vacuum overnight (Scheme 3.1).

3.1.2 Degree of substitution by NMR spectroscopy analysis

The degree of substitution (DS) represents the number of substituents attached to each anhydroglucose unit (AGU) and can range from 0 to 3, corresponding to the hydroxyl groups on carbons 2, 3, and 6. However, the

maximum DS of 3 is only achievable if the 6-OH group is not involved in α(1,6)-linkages. Given that starch includes α(1,6)-branched amylopectin, the DS cannot reach this maximum.[7]

Table 3.1: Reagent molar ratio used for the etherification reaction for each degree of substitution (DS)

Sample	NaOH/AGU	CNCl/AGU	DS
CS1	1	0.2	0.09
CS2	1	1	0.33
CS3	3	4.5	1.24

The DS is calculated, using ^{1}H-NMR spectroscopy, by the ratio of the normalized integration area of the aromatic protons ($A_{Ph}/5$) to the combined integration areas of the anomeric protons Aα(1,4) and Aα(1,6), as shown in Equation 3.1.

$$DS = \frac{A_{Ph}}{5 \cdot (A_{\alpha(1,4)} + A_{\alpha(1,6)})} \tag{3.1}$$

3.1.3 Film formation of etherified yuca starch

450 mg of cinnamyl-starch ether (DS 0.09, CS1) were dissolved in 10 mL of deionized water at 90°C under magnetic stirring for 1 hour. Once fully dissolved, the solution was cooled and poured onto a low-density polyethylene Petri dish. The formed film was then peeled off and left to air-dry at room temperature for 3 days.

3.2 Characterization

ATR-FTIR

ATR-FTIR analysis was employed to preliminary assess the effective derivatization of yuca starch. Specifically, Figure 3.2 shows the FTIR spectra of the native starch, three derivatized samples (CS1-3, with increasing DS), and cinnamyl chloride (CNCl). The region between 1200 and 800 cm^{-1} highlights the characteristic C-O bond bands of both C-OH and C-O-C groups, which are present in the anhydroglucose units of starch. A very broad band around 3400 cm^{-1} is observed, corresponding to the vibration of the -OH bond, which is prominent in the carbohydrate chain, while water bending is found at 1633 cm^{-1}.

The presence of the cinnamic unit modifies the starch spectrum. Specifically, distinct peaks at 1650, 966, and 691 cm^{-1} can be attributed to the stretching and bending of the C=C bond in the disubstituted alkene of the cinnamic unit. Additionally, especially in sample CS3, new signals appear around 3000 cm^{-1}, corresponding to the C-H bonds of both the disubstituted alkene and the aromatic ring. These diagnostic signals are clearly visible in sample CS3, which has a high degree of substitution, and appear weakly in the other two samples. This result indicates the presence of the cinnamic unit in the samples. However, since the bond formed between the cinnamic unit and the starch anhydroglucose unit is an ether bond, it overlaps with the C-O-C bond present in each anhydroglucose unit, making its identification challenging.

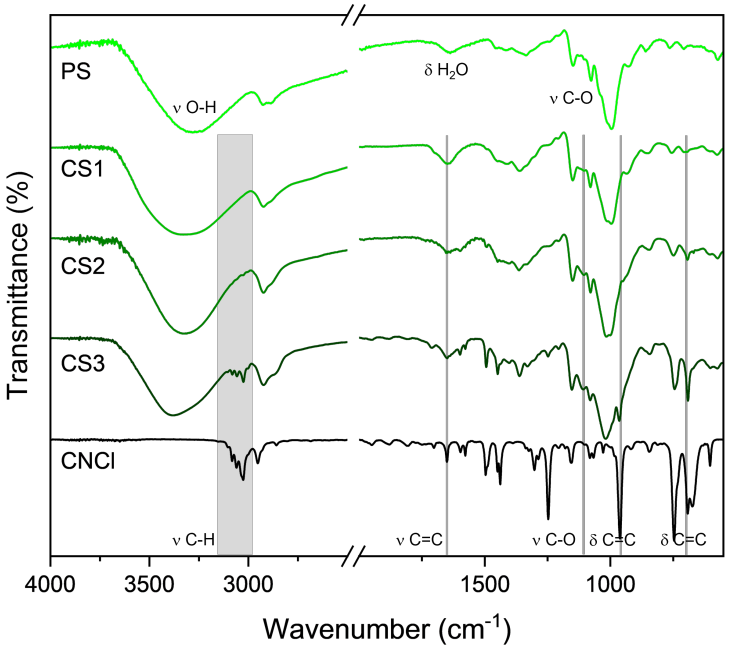

Figure 3.2: FTIR-ATR spectra of pristine yuca starch (PS), cinnamyl chloride (CINN-Cl), and cinnamyl starch samples (CS1-3)

NMR

To confirm the formation of the ether bond between the cinnamic unit and the anhydroglucose units of starch, ^{1}H-NMR spectra were acquired, as shown in the Figure 3.3 for the CS1 sample. The other two samples (CS2-3) exhibit the same diagnostic peaks but with different integration values, which were used to determine their respective degrees of substitution (DS). The spectra were recorded in the presence of deuterated trifluoroacetic acid (TFA-d), which rapidly exchanges the protons of unsubstituted hydroxyl groups with deuterium atoms, thereby eliminating interfering signals that overlap with the protonic peaks of the starch backbone, allowing for accurate DS quantification. The resulting non-deuterated trifluoroacetic acid gives rise to a broad signal centered around 7.5 ppm for unmodified starch and 8.7 ppm for

the CS1 sample, both of which fall outside the diagnostic region of interest.

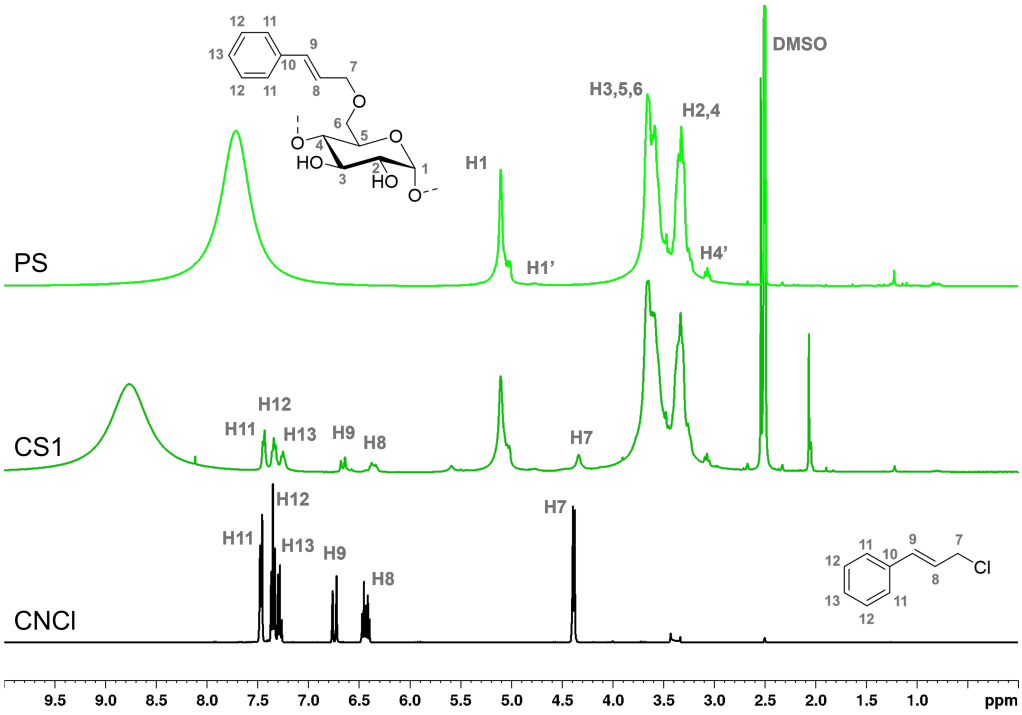

Figure 3.3: Comparison of ^{1}H-NMR spectra in DMSO-d6 for PS, CS1, and CNCl. H-1 indicates anomeric protons in the α(1,4) glycosidic linkage, H-1' for those in α(1,6), and H4' for non-reducing terminal glucose units.

In contrast to the results obtained from infrared spectroscopy, the ^{1}H-NMR spectrum of CS1 clearly shows signals corresponding to the cinnamic unit. Specifically, the aromatic protons (H-11, H-12, and H-13) resonate between 7.5 and 7.2 ppm, while the vinyl protons are observed at 6.65 ppm (H-9) and 6.35 ppm (H-8). The H-7 protons resonate at 4.26 ppm, slightly shifted compared to the corresponding signal in pure cinnamic chloride (CNCl), which appears at 4.34 ppm, suggesting the formation of the ether bond. Furthermore, the relative broadening of the cinnamic unit signals in the CS1 spectrum compared to those in pure CNCl provides additional evidence

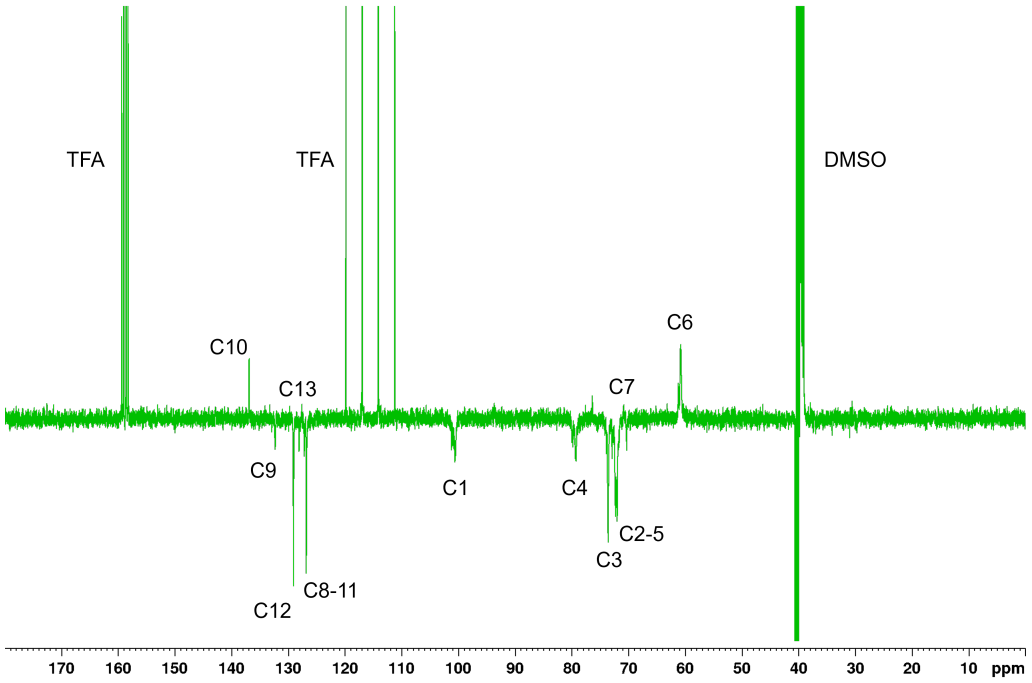

Figure 3.4: ^{13}C-NMR spectrum of CS1 in DMSO-d6

of modification, which can be attributed to the attachment of the cinnamic unit at three different positions (C-2, C-3, and C-6) on both amylopectin and amylose components. This results in the same bonds resonating at slightly different chemical shifts, leading to the formation of a broader signal.

The anomeric protons H-1 (α(1,4)) and H-1' (α(1,6)) resonate at 5.10 and 4.77 ppm, respectively, and the ratio between the integral of the anomeric proton and that of the cinnamic unit signals allows the DS to be calculated, as shown in the Table 3.1 using the previously reported equation.

Figure 3.4 presents the ^{13}C-NMR spectrum of sample CS1 as a representative example. The peaks were assigned following the same approach used for the ^{1}H-NMR spectrum, supported by relevant literature data.[7] This analysis

provides additional verification that the starch modification was successfully achieved.

ss-NMR

For a comprehensive characterization of the material, solid-state ^{13}C CP-MAS NMR spectra were acquired for all samples. In Figure 3.5 the spectra of the initial components, namely cinnamyl chloride (CNCl) and yuca starch, as well as the modified starch samples (CS1-3) are reported and compared. The resonances corresponding to the starch carbons are observed in the following regions: 94-105 ppm for C-1, 80-84 ppm for C-4, 68-77 ppm for C-2, C-3, and C-5, and 58-65 ppm for C-6.[8] In the cinnamyl chloride spectrum, the vinyl carbons resonate at 134 ppm (C-9) and 125 ppm (C-8), while the aromatic ring carbons resonate between 125-130 ppm (C11-13) and at 136 ppm (C-10). The corresponding peaks are also present, despite broader, in the substituted starch samples, further confirming the presence of the cinnamyl moiety.

The allylic carbon C-7 of cinnamyl chloride resonates at 46 ppm, but it is absent in the spectra of cinnamyl-starch samples. According to the literature data on cinnamyl ethers,[9] the etherification reaction causes a shift of the allylic carbon C-7 to approximately 70 ppm, placing it in the same spectral region as the starch carbon atoms. To identify the C-7 signal and confirm the formation of a covalent bond between starch and the cinnamyl moiety, a Cross Polarization with Polarization Inversion (CPPI) pulse sequence was applied to the solid-state NMR analysis of the CS2 sample (see Figure 3.5). The parameters were optimized to obtain ^{13}C-NMR spectra with

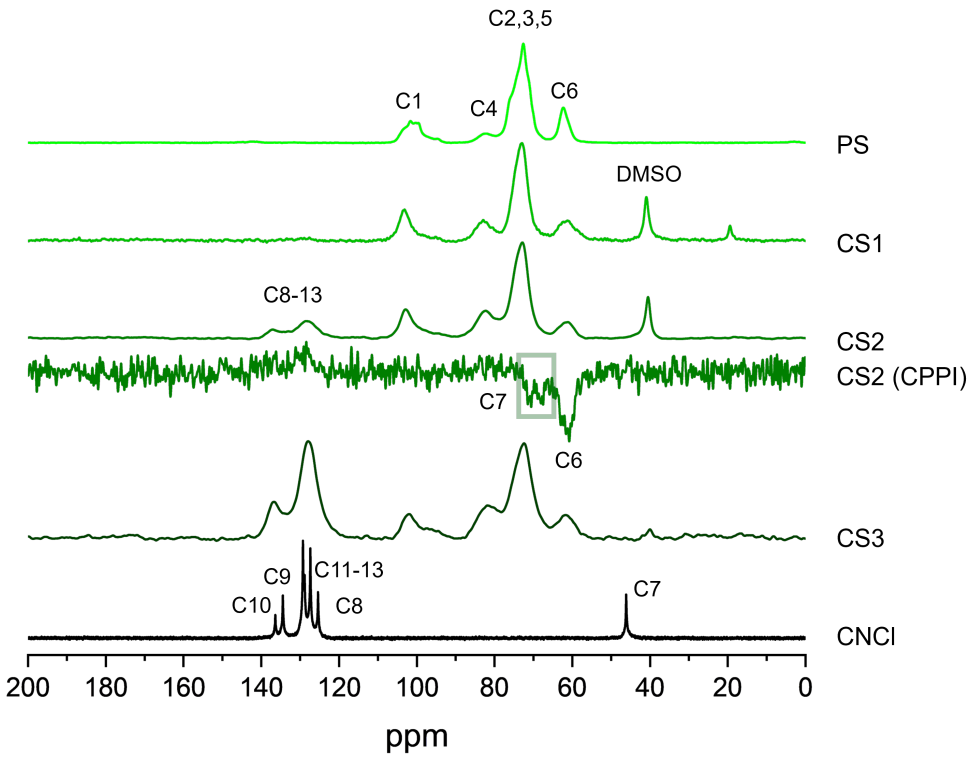

Figure 3.5: ^{13}C CPMAS NMR spectra of PS, CS1, CS2, CS3 and ^{13}C CPPI NMR spectrum of CS2 sample (cinnamyl methylene carbons involved in the ether linkage are highlighted)

CH_2 resonances appearing as negative peaks while suppressing all other carbon resonances (e.g., CH_3, CH, and quaternary carbons).[10] The ^{13}C CPPI NMR spectrum of CS2 reveals three signals: the first, centered at 61 ppm, corresponds to the C-6 carbon of the anhydroglucose units, while the other two, located at approximately 68 and 71 ppm, represent the cinnamyl allylic CH_2 involved in ether linkages (C-7), consistent with literature data.[9] The presence of two peaks may indicate different grafting sites on the starch chains. Moreover, the absence of the peak at 46 ppm associated with the allyl chloride further supports the successful covalent grafting of cinnamyl

moieties onto yuca starch.

It is also noteworthy that the C-1 carbon signal is sensitive to starch crystalline conformations. Specifically, the shape of the C-1 resonance in yuca starch is characteristic of crystalline starch, while the C-1 line shape of the derivatized samples (CS1-3) suggests amorphization resulting from the modification process.

Overall, the combined results from ATR-FTIR, solution, and solid-state NMR spectroscopy unequivocally demonstrate the formation of a covalent ether bond between yuca starch and the cinnamyl moiety.

Solubility Properties

The solubility of starch derivatives is influenced by their degree of substitution (DS), as the introduction of apolar groups modifies the polar hydroxy groups responsible for hydrogen bonding. The solubility of starch cinnamyl ethers (CS1-3) was analyzed. CS1 was soluble in demineralized water. CS2, on the other hand, dissolved in ethanol only after prolonged mixing at room temperature but remained insoluble in water. CS3 was insoluble in polar solvents like water, ethanol, and acetone, whether at room temperature or under reflux conditions. However, it dissolved in toluene when heated to 90°C. Therefore, adjusting the DS allows for control over the solubility: slight derivatization leads to water solubility by weakening the hydrogen bonding network, while higher DS enhances solubility in non-polar organic solvents, potentially broadening its practical applications.

TGA

Thermogravimetric analysis was conducted on the modified starch samples to evaluate the thermal stability of the material following chemical modification. Figure 3.6 shows the thermograms of both the unmodified starch and the modified samples (CS1-3), along with the derivative thermogravimetric (DTG) curves of each sample (inset). The unmodified starch exhibits two distinct degradation processes: the first, occurring up to 150°C, corresponds to the dehydration of the sample, while the second degradation step begins at 270°C, with a maximum mass loss observed around 300°C, which corresponds to the decomposition of the carbon chain.

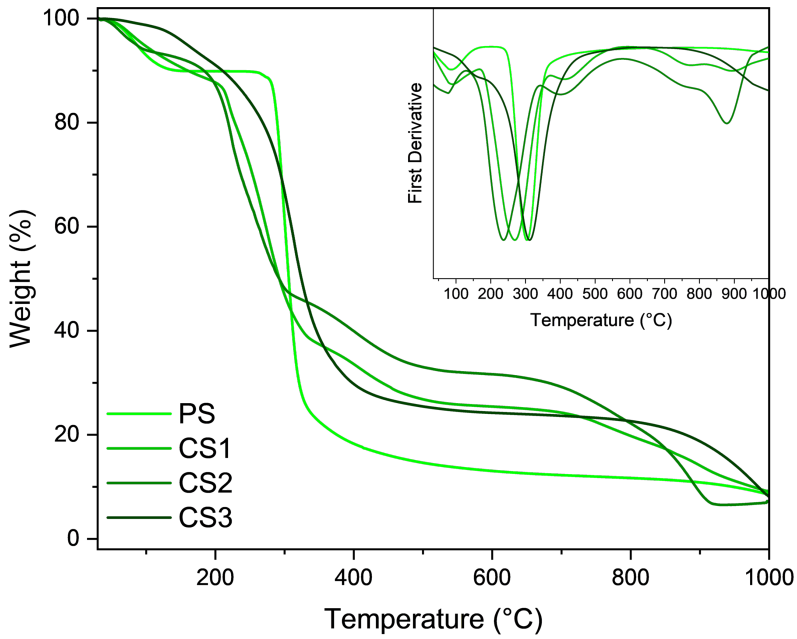

Figure 3.6: TGA and DTG (inset) of CS1-3 compared to PS

In contrast, the modified starch samples exhibit multi-step degradation curves,

likely indicating the combined decomposition of functionalized and non-functionalized fractions of the polymer.[11] Additionally, as the degree of substitution increases, a transition to a single-step degradation trend is observed, suggesting improved homogeneity in the chain distribution. This is also accompanied by an increase in the thermal stability of the sample.

Photoresponsive properties

The photoresponsive properties of the new material were investigated using both UV-Vis and NMR spectroscopy. Specifically, sample CS1 was analyzed exclusively by UV-Vis spectroscopy, as the cinnamic unit signals in the NMR spectrum, though detectable, were too weak to observe significant changes. In contrast, sample CS2 was studied using both UV-Vis and NMR spectroscopy. The photoresponsive properties of sample CS3 could not be evaluated due to its low solubility, even in organic solvents like DMSO.

- *UV-VIS*

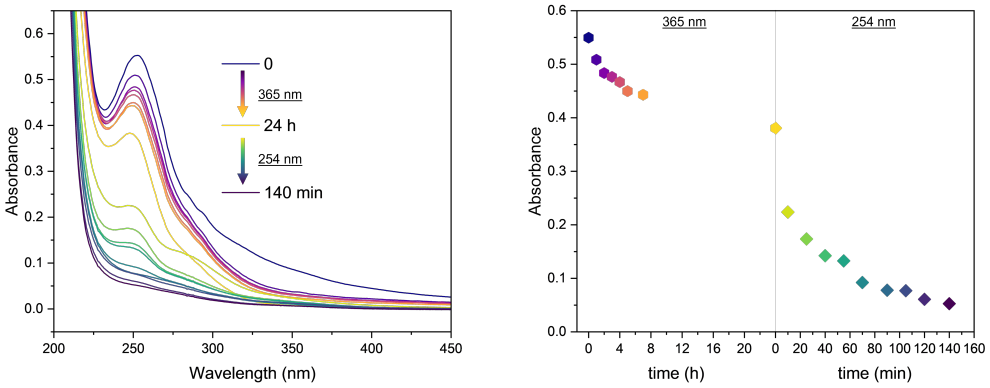

Figure 3.7: UV-Vis spectra of CS1 sample after exposure at $\lambda \sim 365$ nm and, subsequently, at $\lambda = 254$ nm (left); maximum absorption plotted against UV irradiation time at $\lambda \sim 365$ nm and $\lambda = 254$ nm (right)

A solution of CS1 was prepared in water at a concentration of 10^{-4} M for the cinnamic units and analyzed using a UV-Vis spectrophotometer. The solution was placed in a well-sealed quartz cuvette, which was thermostated and irradiated under a 365 nm lamp at different time intervals. After 24 hours of irradiation, the solution was further irradiated using a second lamp at 254 nm. The UV-Vis spectra are shown in the Figure 3.7 (left), while Figure 3.7 (right) depicts the absorbance trend as a function of irradiation time at the wavelength of maximum absorption (250 nm). A progressive decrease in the absorption band is observed, particularly during irradiation at 254 nm. This behavior can be attributed to the loss of conjugation of the cinnamic unit, which reacts with another neighbouring cinnamic unit to form a cyclobutane ring.

Additionally, the absorbance trend over time indicates that, under 365 nm irradiation, the decrease in absorbance is slower and reaches a plateau after 24 hours. In contrast, after subsequent irradiation at 254 nm, the absorbance decreases again, reaching a second plateau within 140 minutes. These preliminary results may suggest that the modified starch undergoes photodimerization in aqueous solution. Sample CS2 exhibited similar behavior; however, the solution was prepared in ethanol, as the degree of substitution prevented its solubility in water.

- *^{1}H-NMR*

The photodimerization properties observed via UV-Vis spectroscopy were further investigated using ^{1}H-NMR spectroscopy to confirm the formation of cyclobutene (Scheme 3.2). CS2 sample was dissolved in DMSO-d6 and irradiated at 365 nm for 24 hours in a quartz cuvette. The ^{1}H-NMR spectra of

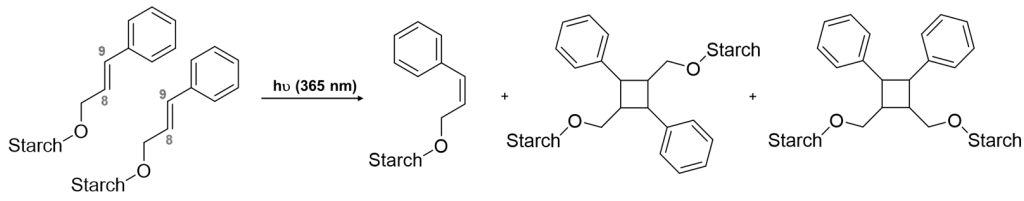

Scheme 3.2: Photodimerization of Cinnamyl Starch

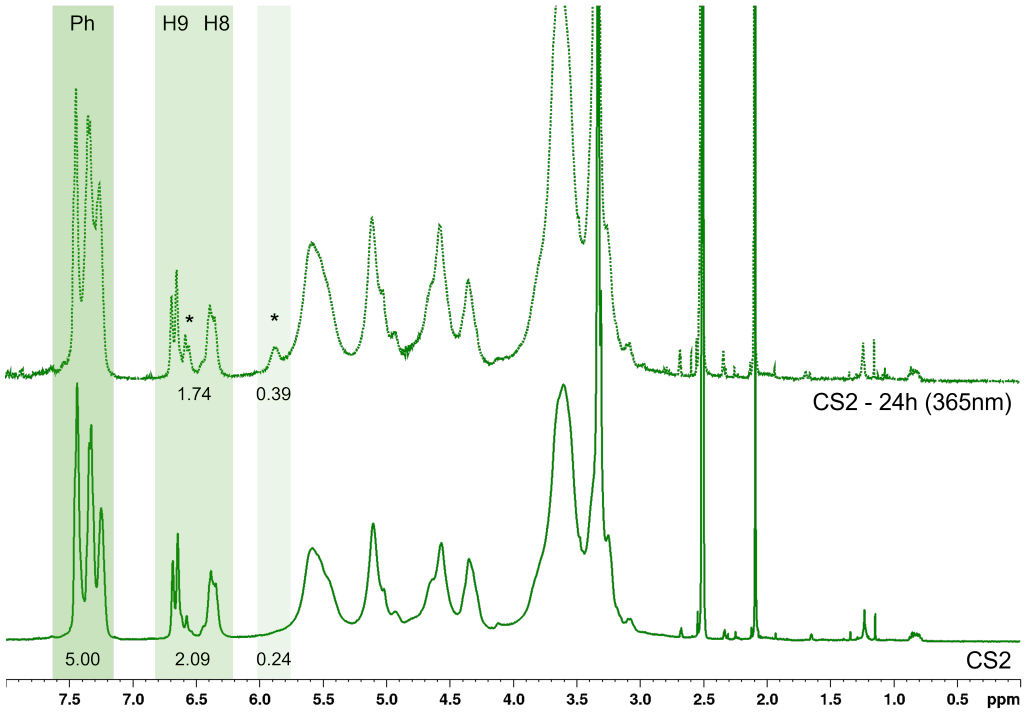

Figure 3.8: ^{1}H-NMR spectra of the CS2 sample in DMSO-d6 before and after 24h UV exposure ($\lambda \sim 365$ nm). Shaded areas highlight spectral changes, with * indicating new peaks; relevant integrals are marked

the sample before and after irradiation are shown in the Figure 3.8. It should be noted that, unlike in Figure 3.3, TFA-d6 was not added to the sample, in order to avoid any potential interference during the irradiation process. According to literature,[12–16] the proton signals of cyclobutane resonate between 4.5 and 3.0 ppm, and their appearance would provide evidence for the photodimerization of the cinnamic unit. However, this region is filled

with broad signals from the starch carbon chain that could obscure the new signals, making it difficult to observe any significant changes. Nevertheless, after irradiation, new signals were observed near the aromatic region at 6.6 and 5.8 ppm (marked with *). These signals can be attributed to protons H-9 and H-8 of the cinnamic unit, respectively, in the Z-configuration, suggesting photoinduced isomerization. Moreover, the sum of the integrals of the two green regions between 7.0 and 5.0 ppm decreased from 2.33 to 2.13 after irradiation, indicating that a portion of the vinyl protons reacted, likely resulting in partial photodimerization. Although further analysis is needed, this behavior suggests a possible competition between photodimerization and photoisomerization of the cinnamyl moieties, especially in solution, as widely reported in the literature.[13, 14] In summary, the combined UV-Vis and NMR investigations support partial but successful cross-linking via $2\pi + 2\pi$ cycloaddition of the double bonds in the starch cinnamyl units when irradiated at 365 nm.

To complete the analysis and provide a comparison with the UV-Vis spectroscopy results, the same sample was subsequently irradiated under a 254 nm lamp for 10 minutes. This led to partial degradation of the starch itself, indicating that the decrease observed in the UV-Vis spectrum after irradiation at 254 nm could also be due to the degradation of the starch chains.

Film

Films were fabricated using the solvent-casting method to demonstrate the potential applicability of the innovative bio-based, bio-inspired polymer. CS1 was selected because of its solubility in water, which is a biocompatible

solvent. The resulting film exhibits a uniform and transparent appearance (Figure 3.9).

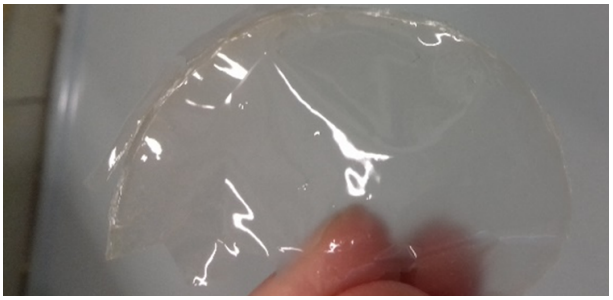

Figure 3.9: Photo of CS1 film fabricated by solvent-casting method

References

(1) Jiang, T.; Duan, Q.; Zhu, J.; Liu, H.; Yu, L. Starch-based biodegradable materials: Challenges and opportunities. *Advanced Industrial and Engineering Polymer Research* **2020**, *3*, 8–18, DOI: 10.1016/j.aiepr.2019.11.003.

(2) Livesey, G. In *Reference Module in Biomedical Sciences*; Elsevier: 2014, B978012801238300043X, DOI: 10.1016/B978-0-12-801238-3.00043-X.

(3) Tabaglio, V.; Fiorini, A.; Ndayisenga, V.; Ndereyimana, A.; Minuti, A.; Nyembo Nyembo, R.; Nyembo Ngoy, D.; Bertoni, G. Sustainable Intensification of Cassava Production towards Food Security in the Lomami Province (DR Congo): Role of Planting Method and Landrace. *Agronomy* **2023**, *13*, 228, DOI: 10.3390/agronomy13010228.

(4) Roy, P. S.; Mention, M. M.; Turner, M. A. P.; Brunissen, F.; Stavros, V. G.; Garnier, G.; Allais, F.; Saito, K. Bio-based photo-reversible self-healing polymer designed from lignin. *Green Chemistry* **2021**, *23*, 10050–10061, DOI: 10.1039/D1GC02957F.

(5) Zhang, R.; Chu, F.; Hu, Y.; Hu, H.; Hu, Y.; Liu, H.; Huo, C.; Wang, H. Preparation of Photo-Crosslinking Starch Colloidal Particles. *Starch - Stärke* **2020**, *72*, 1900175, DOI: 10.1002/star.201900175.

(6) Du, Y.; Niu, L.; Song, X.; Niu, J.; Zhang, C.; Zhi, K. Dual-modified starch as particulate emulsifier for Pickering emulsion: Structure, safety properties, and application for encapsulating curcumin. *International Journal of Biological Macromolecules* **2024**, *266*, 131206, DOI: 10.1016/j.ijbiomac.2024.131206.

(7) Tizzotti, M. J.; Sweedman, M. C.; Tang, D.; Schaefer, C.; Gilbert, R. G. New 1H NMR Procedure for the Characterization of Native and Modified Food-Grade Starches. *Journal of Agricultural and Food Chemistry* **2011**, *59*, 6913–6919, DOI: 10.1021/jf201209z.

(8) Bugnotti, D.; Dalle Vacche, S.; Esposito, L. H.; Callone, E.; Orsini, S. F.; Ceccato, R.; D'Arienzo, M.; Bongiovanni, R.; Dirè, S.; Vitale, A. Structure of Starch-Sepiolite Bio-Nanocomposites: Effect of Processing and Matrix-Filler Interactions. *Polymers* **2023**, *15*, 1207, DOI: 10.3390/polym15051207.

(9) Kasashima, Y.; Uzawa, A.; Hashimoto, K.; Nishida, T.; Murakami, K.; Mino, T.; Sakamoto, M.; Fujita, T. Synthesis of Cinnamyl Ethers from α-Vinylbenzyl Alcohol Using Iodine as Catalyst. *Journal of Oleo Science* **2010**, *59*, 549–555, DOI: 10.5650/jos.59.549.

(10) Wu, X.; Zilm, K. Complete Spectral Editing in CPMAS NMR. *Journal of Magnetic Resonance, Series A* **1993**, *102*, 205–213, DOI: 10.1006/jmra.1993.1092.

(11) Tester, R. F.; Karkalas, J.; Qi, X. Starch—composition, fine structure and architecture. *Journal of Cereal Science* **2004**, *39*, 151–165, DOI: 10.1016/j.jcs.2003.12.001.

(12) Cohen, M. D.; Schmidt, G. M. J.; Sonntag, F. I. 384. Topochemistry. Part II. The photochemistry of trans-cinnamic acids. *Journal of the Chemical Society (Resumed)* **1964**, 2000, DOI: 10.1039/jr9640002000.

(13) Schmidt, G. M. J. 385. Topochemistry. Part III. The crystal chemistry of some trans-cinnamic acids. *Journal of the Chemical Society (Resumed)* **1964**, 2014, DOI: 10.1039/jr9640002014.

(14) Egerton, P. L.; Hyde, E. M.; Trigg, J.; Payne, A.; Beynon, P.; Mijovic, M. V.; Reiser, A. Photocycloaddition in liquid ethyl cinnamate and in ethyl cinnamate glasses. The photoreaction as a probe into the micromorphology of the solid. *Journal of the American Chemical Society* **1981**, *103*, 3859–3863, DOI: 10.1021/ja00403a039.

(15) Amjaour, H.; Wang, Z.; Mabin, M.; Puttkammer, J.; Busch, S.; Chu, Q. R. Scalable preparation and property investigation of a cis-cyclobutane-1,2-dicarboxylic acid from β-trans-cinnamic acid. *Chemical Communications* **2018**, *55*, 214–217, DOI: 10.1039/C8CC08017H.

(16) Fonseca, I.; Hayes, S. E.; Blümich, B.; Bertmer, M. Temperature stability and photodimerization kinetics of β-cinnamic acid and comparison to its α-polymorph as studied by solid-state NMR spectroscopy techniques and DFT calculations. *Physical Chemistry Chemical Physics* **2008**, *10*, 5898, DOI: 10.1039/b806861e.

Chapter 4

Proof of concept of starch-based nanocomposites

This chapter focuses on the development and characterization of bio-nanocomposites, specifically those based on starch and sepiolite or silica nanoparticles. The goal is to create materials that can respond to external stimuli, such as light, through reversible assembly and disassembly, making them particularly promising for applications like sustainable packaging.

The first part of the chapter examines the interactions between sepiolite and starch, as previously explored in collaborative studies. These bio-nanocomposites, consisting of yuca starch, glycerol as a plasticizer, and varying amounts of sepiolite, show potential as biodegradable alternatives to petroleum-based plastics. The study highlights that while sepiolite enhances thermal stability, mechanical strength, and water resistance, higher concentrations can lead to aggregation and inhomogeneous dispersion.

To address these challenges, functionalizing agents such as cinnamic units were introduced to both the filler and the polymer matrix. These units have the potential to create covalent bonds between the matrix and filler, forming a stable network that can be disassembled under specific light conditions. This feature aligns with circular economy principles, enabling the formation and degradation of these materials with minimal environmental impact.

The second part of this chapter presents initial trials in preparing bio-nanocomposites using silica nanoparticles functionalized with cinnamic units. These nanoparticles were selected as a model system. Additionally, a low-substitution yuca starch was chosen as the polymer matrix to ensure water-processability, making the material suitable for eco-friendly applications.

Throughout the chapter, the groundwork is laid for further exploration. This

includes optimizing the preparation process, investigating different degrees of functionalization, and studying how these parameters affect the final properties of the material, such as mechanical strength, thermal stability, biodegradability, and photocrosslinking behavior.

4.1 Starch-Sepiolite Bio-Nanocomposites

Regarding this project and the potential to develop starch-based bionanocomposites that can assemble and disassemble in response to the wavelength of incident radiation, a collaboration with the University of Trento was initiated. The first step involved studying the interaction between raw sepiolite and raw starch, as reported by Bugnotti et al.[1] in the paper titled "Structure of Starch–Sepiolite Bio-Nanocomposites: Effect of Processing and Matrix–Filler Interactions".

This study explores how the processing method and the inclusion of sepiolite clay influence the microstructure and properties of starch-based bionanocomposites. These materials hold great promise for applications such as sustainable packaging due to their biodegradability and potential to replace petroleum-based plastics.

The bio-nanocomposites were prepared by combining starch (from yuca), 40 wt.% glycerol (as a plasticizer), and untreated sepiolite at various loadings (3, 5, 10, and 15 wt.%). The processing involved starch gelatinization, where the rigid lattice structure of semicrystalline starch is disrupted by heating, followed by mixing with glycerol and sepiolite, and casting to form thin films. The goal was to produce flexible, transparent films suitable for use as packaging materials. The results provided valuable insights into the structural, thermal, and mechanical behavior of the composite films, influenced by both the processing method and filler content.

In order to have a total overview of systems, the acronyms used in this work are listed in the Figure 4.1.

Sample	Glycerol (% *w/w*)	Sepiolite (% *w/w*)	Sample Form
Y_p	0	0	Powder
Y_f	0	0	Film
YG_f	40	0	Film
$YG3S_f$	40	3	Film
$YG5S_f$	40	5	Film
$YG10S_f$	40	10	Film
$YG15S_f$	40	15	Film
$Y5S_f$	0	5	Film
$Y10S_f$	0	10	Film

Figure 4.1: Sample list and labeling: Y = yuca starch, G = glycerol, S = sepiolite. Percentages are given relative to starch content[1]

The gelatinization process used to form the films effectively disrupted the semicrystalline structure of starch, as analyzed by ^{13}C CPMAS NMR. The spectra of pristine starch powder (Y_p), starch film (Y_f), and plasticized starch film (YG_f) are shown in Figure 4.2, with carbon labels provided in the inset. The C1 and C4 carbons, involved in glycosidic bonds, are the most sensitive to starch conformation, as they reflect the geometry of these linkages. In Y_p, the C1 region exhibited a shoulder characteristic of a V-type polymorph and a triplet signal of an A-type polymorph. In contrast, Y_f and YG_f films showed a different C1 signal, typical of amorphous starch.

The C2,3,5 region also broadened significantly, forming a less defined signal, while the intensity of the C4 site, related to the amorphous regions of starch, increased. This confirmed that starch had transformed into an amorphous form during film processing, indicating successful gelatinization. The YG_f sample also revealed distinct glycerol resonances, confirming its presence in the film.

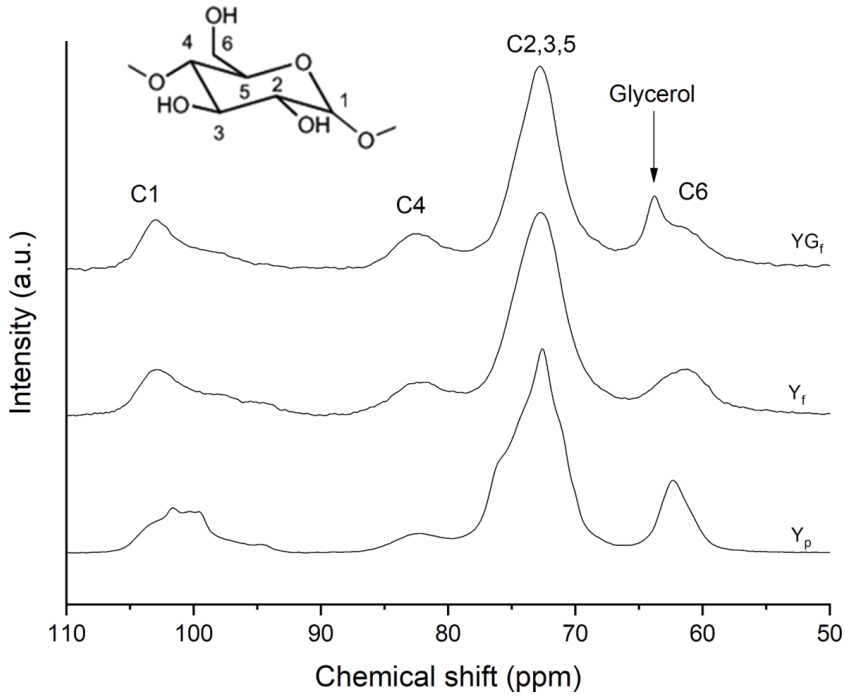

Figure 4.2: ^{13}C CPMAS NMR spectra of Y_p, Y_f, and YG_f samples. The arrow points to the glycerol methylene peak[1]

XRD analysis showed that pristine starch (Y_p) displayed typical A-type crystalline reflections with 45.2% crystallinity and a small V-type content (1.5%). In contrast, Y_f and YG_f films showed amorphous halos, consistent with the NMR results, indicating a loss of crystalline structure. In YG_f, the amorphous halo's intensity and position shifted slightly due to glycerol interactions with starch chains (Figure 4.3).

Similarly, FTIR analysis confirmed these structural changes, with shifts in the O-H stretching band and reduced crystalline peak intensity. Glycerol, used as a plasticizer to enhance flexibility, had a significant impact on the starch structure, promoting amorphization through strong hydrogen bonding with the hydroxyl groups of starch.

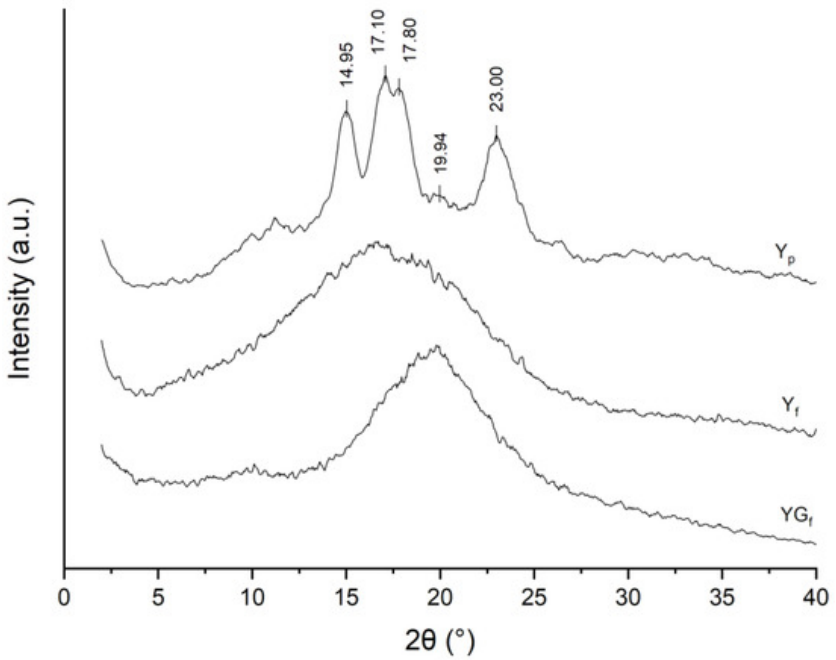

Figure 4.3: XRD patterns of Y_p, Y_f and YG_f samples[1]

Sepiolite's inclusion also affected the films' structure and properties. Figure 4.4 illustrates the uniform and transparent nature of the films, regardless of sepiolite content, though a yellowish tint became more pronounced with higher filler content. Transparency, evaluated using UV-Vis spectroscopy, showed that glycerol and sepiolite had little effect in the visible range. However, in the nanocomposite film with the highest sepiolite content ($YG15S_f$), an absorbance peak appeared below 300 nm, attributed to Mg-O-Si bonds in sepiolite, indicating interaction between sepiolite and the starch matrix.

SEM analysis showed that the sepiolite filler, with its needle-like shape, was well-dispersed throughout the starch matrix in both $YG3S_f$ (lowest filler content) and $YG15S_f$ (highest filler content) (Figure 4.5). Some agglomeration was observed at the highest sepiolite concentration (15 wt.%).

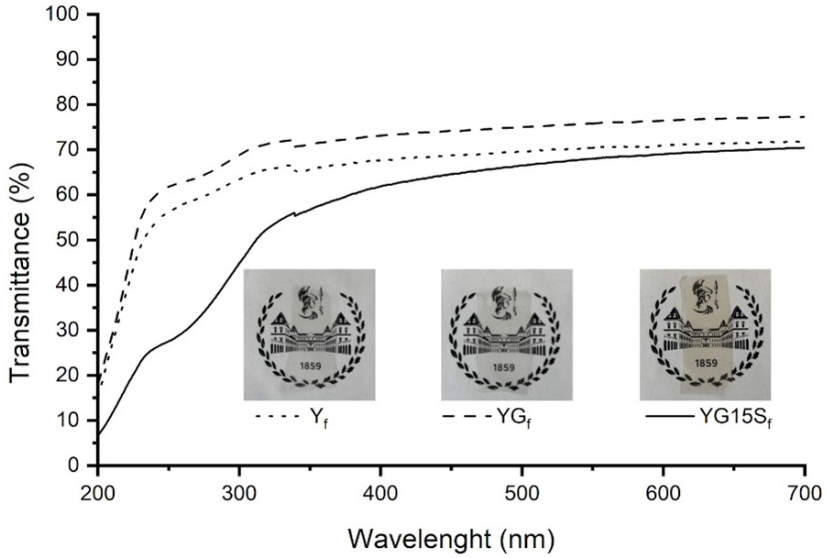

Figure 4.4: UV–Vis transmittance spectra and images of starch film (Y_f), plasticized starch film (YG_f), and nanocomposite films with 15 wt.% sepiolite ($YG15S_f$)[1]

The ^{13}C CPMAS NMR spectra of composites, along with the reference YG_f, indicated that sepiolite does not significantly affect the amorphous structure of the starch matrix (Figure 4.6). The glycerol peak remained at a consistent resonance position but broadened and lost intensity in the composites, suggesting reduced chain mobility or increased anisotropy due to glycerol–sepiolite interactions.

^{29}Si CPMAS NMR was employed to analyse sepiolite in nanocomposite films, using neat sepiolite as a reference (see paragraph 2.3.2.2 for an explanation of sepiolite peaks). The Si1 peak, located near structural water at the edges of the octahedral sheets, showed reduced intensity in the composite films compared to neat sepiolite. In neat sepiolite, the intensity ratio of the triplet resonances was approximately 1:1:1, but this ratio changed in

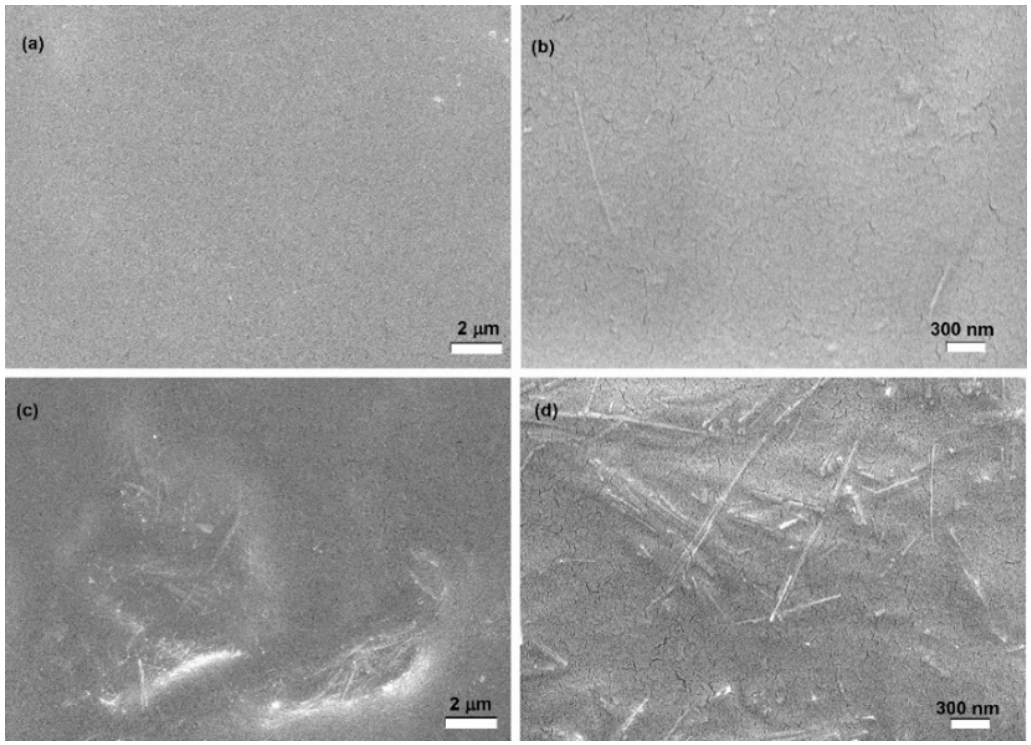

Figure 4.5: SEM images of $YG3S_f$ (a, b) at 10 kX and 50 kX magnification, and $YG15S_f$ (c, d) at 10 kX and 50 kX magnification, showing consistent dispersion of sepiolite particles[1]

the composites. This suggests that glycerol may be replacing zeolitic water within sepiolite's channels, interacting with structural water or Mg-OH protons, thereby altering the intensity ratio. To investigate further, two film samples of starch and sepiolite were prepared without glycerol. The ^{29}Si CPMAS NMR spectra of these samples (Figure 4.7) confirmed that starch alone does not interact with sepiolite's channels, verifying that the decrease in Si1 intensity is due to glycerol intercalation within the sepiolite structure.

XRD analysis was performed to examine the long-range order of nanocomposite films with diffractograms presented in Figure 4.8. The basal plane

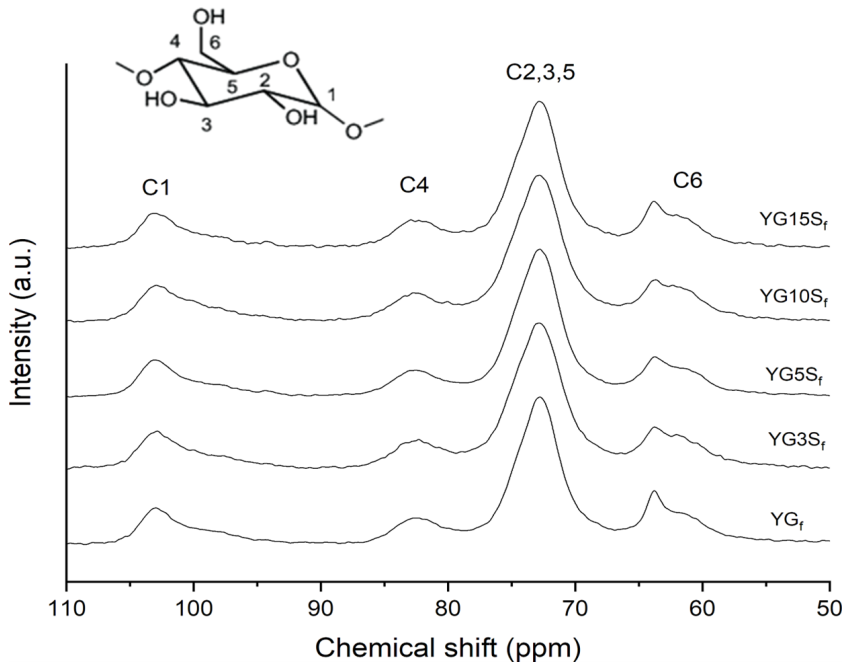

Figure 4.6: ^{13}C CPMAS NMR spectra of plasticized starch film (YG_f) and composite films with sepiolite at various loadings: $YG3S_f$, $YG5S_f$, $YG10S_f$, and $YG15S_f$[1]

(110) of sepiolite as observed at approximately 7.20°, corresponding to a d-spacing of 1.22 nm (calculated via Bragg's law), and was consistently visible in all composite films. Glycerol and starch did not disrupt the internal channels of sepiolite, as its sheets are covalently bonded and cannot be exfoliated. Additional sepiolite reflections were detected at 2δ values of 19.8°, 20.5° (weak), 23.6°, and 26.3°. The peak intensities increased with higher sepiolite content, notably for the (060) reflection at 19.8° and the (080) peak at 26.3°. However, no crystalline starch peaks were observed in the nanocomposites, indicating that the amorphous structure of starch remained unchanged, consistent with NMR findings. The enhanced intensity of the 0k0 reflections, combined with the unchanged crystallite size and ^{13}C CPMAS NMR results, suggests the emergence of a filler-preferred orienta-

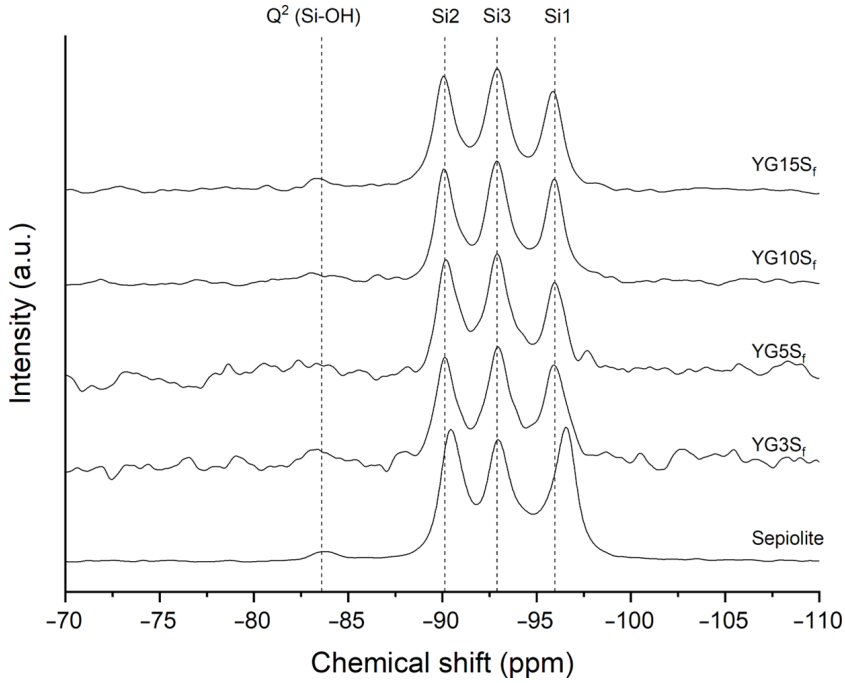

Figure 4.7: ^{29}Si CPMAS NMR spectra of pristine sepiolite compared with nanocomposites at different sepiolite loadings: YG3S$_f$, YG5S$_f$, and YG10S$_f$[1]

tion in the bio-composites. This is likely due to interactions between starch and sepiolite, leading to its alignment within the matrix.

FTIR spectra showed no major changes with the addition of sepiolite, but an increase in the area under the peak at 970 cm^{-1} with higher filler content indicated more Si-OH bond vibrations, confirming sepiolite-starch interactions.

Thermogravimetric analysis revealed that sepiolite enhanced the thermal resistance of the films, though thermal stability decreased slightly at the highest sepiolite content (15 wt.%). At lower concentrations (3–5 wt.%), sepiolite was well-dispersed throughout the starch matrix, but agglomeration

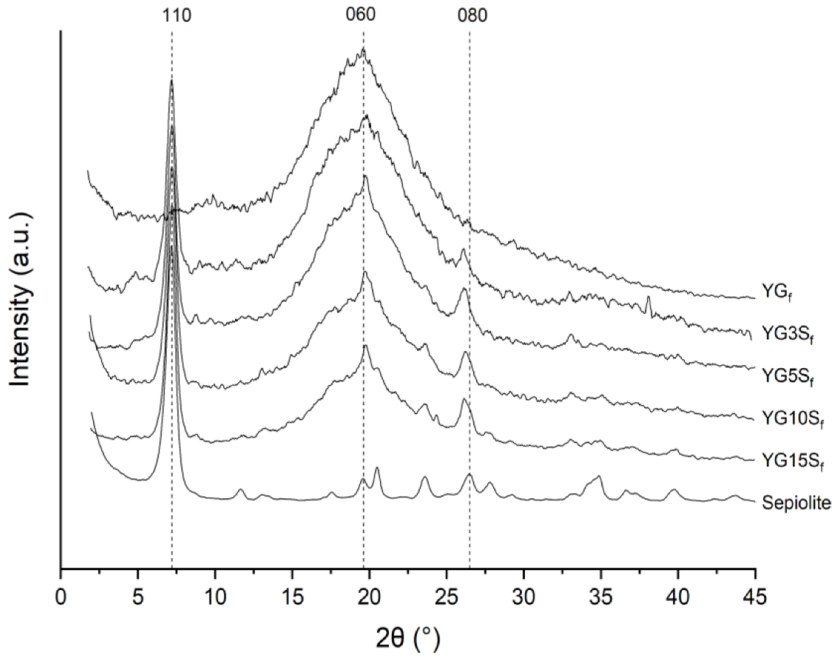

Figure 4.8: Diffractograms of pristine sepiolite, plasticized starch film (YG_f), and nanocomposite films with varying sepiolite loadings ($YG3S_f$, $YG5S_f$, $YG10S_f$, and $YG15S_f$)[1]

occurred at higher concentrations (10–15 wt.%), suggesting complex interactions between sepiolite, glycerol, and starch chains.

The study demonstrated that starch processing significantly disrupted its crystalline structure, resulting in an amorphous film, particularly when glycerol was added. Sepiolite, when incorporated into these films, interacted with glycerol, leading to subtle structural reorientations, but did not alter the overall amorphous nature of the starch. The nanocomposites exhibited improved thermal stability due to the presence of sepiolite, highlighting the potential of these materials for applications such as sustainable packaging. However, at higher loadings, aggregates and inhomogeneous filler dispersion may occur. The interaction between the filler and the polymer

matrix is primarily electrostatic, which could lead to phase separation over time due to environmental factors such as humidity and temperature. A potential solution to this issue is to introduce a functionalizing agent on the filler surface to improve dispersion within the polymer matrix. Additionally, modifying both the filler and the polymer matrix with photoreversible units, such as cinnamic groups, could create a nanocomposite with strong covalent bonds between the matrix and the filler. This network could be activated by irradiation at a specific wavelength and broken by irradiation at another wavelength, offering a reversible, low-environmental-impact approach in line with circular economy principles.

The following section presents a preliminary attempt to create bio-nanocomposites with photoresponsive properties based on these findings.

4.2 Bio-Nanocomposites with photo-responsive properties

In Chapter 2, the design of two types of fillers, SiO_2 nanoparticles (SiO_2 NPs) and sepiolite nanofibers (SepOH NFs), both functionalized with cinnamic units, was discussed in detail. These cinnamic units impart photoresponsive properties to the system. Chapter 3 focused on the modification of yuca starch polymer chains with the same cinnamic units, resulting in three different degrees of substitution depending on the reaction conditions.

Considering this background, the aim of this section is to present an initial attempt at preparing photoresponsive bio-nanocomposites using the aforementioned materials. Specifically, silica nanoparticles functionalized with cinnamic units via the one-pot procedure (SiO_2@CN) were selected, as this method results in a higher degree of functionalization, approximately 1.8 n./nm^2, compared to the two-step strategy. Silica nanoparticles were chosen as the model system to simplify the development and the study of the photoresponsive bio-nanocomposite by minimizing other factors such as the anisotropy and porosity characteristic of sepiolite, which can trap glycerol or intercalate polymer chains.

For the polymer matrix, the sample with the lowest degree of substitution (CS1) was selected, as it can be processed in water. As described in Chapter 3, higher degrees of substitution reduce water solubility but increase solubility in organic solvents. Additionally, with the lower degree of substitution, glycerol remains necessary as a plasticizer, since it forms hydrogen bonds with the unmodified hydroxyl groups in the starch chains.

This section introduces the first trials in the preparation of these photoresponsive bio-nanocomposites, laying the groundwork for further exploration and optimization.

4.2.1 Experimental procedure

12.5 mg of SiO_2@CN was dispersed in 10 mL of distilled water, initially by ultrasonication for 10 minutes, followed by magnetic stirring at room temperature (RT) for 24 hours. Afterward, 250 mg of CS1 and 100 mg of glycerol were added to the mixture, which was then stirred, heated, and maintained at 90°C for 30 minutes. To minimize air bubbles during the film formation process, the suspension was cooled to room temperature and subjected to an additional 10 minutes of ultrasonication. The mixture was cast into a low-density polyethylene (PE) petri dish with a diameter of 4 cm, and the solvent was allowed to evaporate at 40°C in an oven for 48 hours. This process resulted in a transparent, free-standing film with a pale yellow tint, labeled CS1-G-5SiCN (Figure 4.9).

Figure 4.9: Photo of CS1-G-5SiCN film

The Figure 4.10 illustrates the experimental procedure and clarifies the abbreviations used for these bio-nanocomposites based on their composition. This method offers a reliable approach to creating uniform, transparent films with photoresponsive properties.

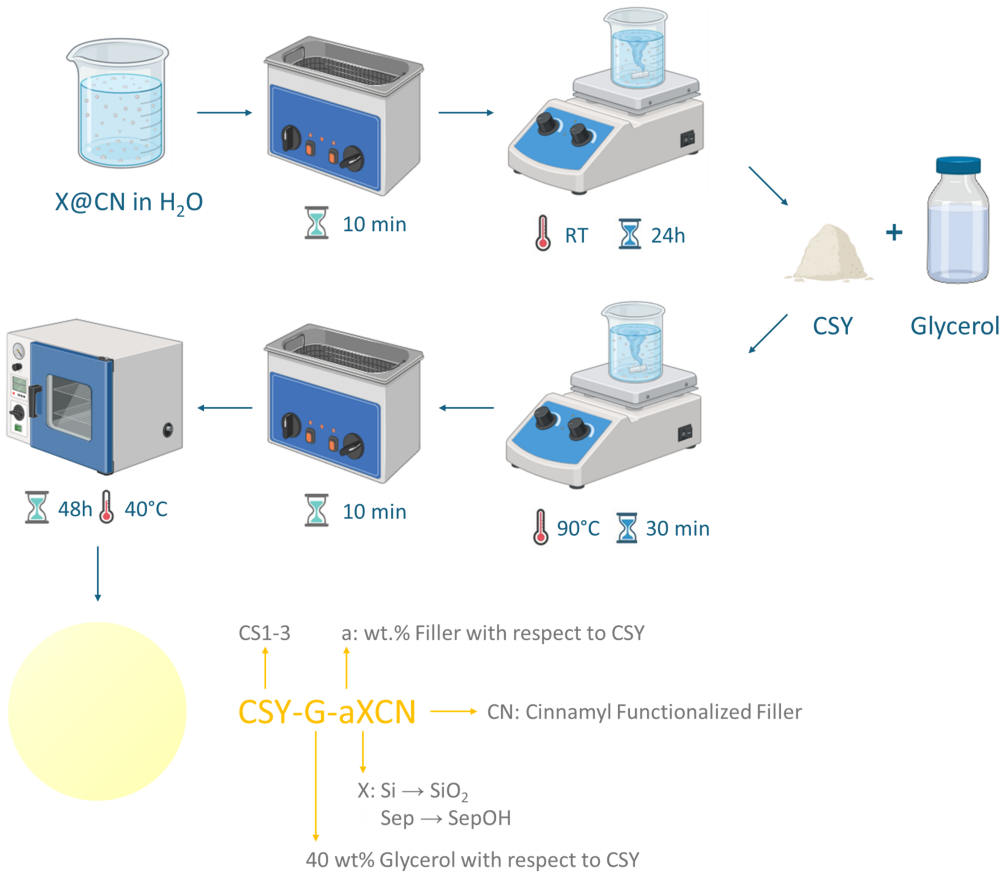

Figure 4.10: Generic scheme for the preparation of photoresponsive nanocomposites from X@CN, glycerol, and CSY, along with the labeling procedure for the nanocomposites

4.2.2 Preliminary DRS Analysis

A preliminary DRS spectrum of the sample was obtained to verify its absorption properties (Figure 4.11). The graph shows a reflectance band that begins to decrease around 350 nm, followed by a sharp decline from 300 nm to 190 nm. This behavior is consistent with what has been observed for silica nanoparticles functionalized with cinnamic units, confirming the sample's absorption characteristics.

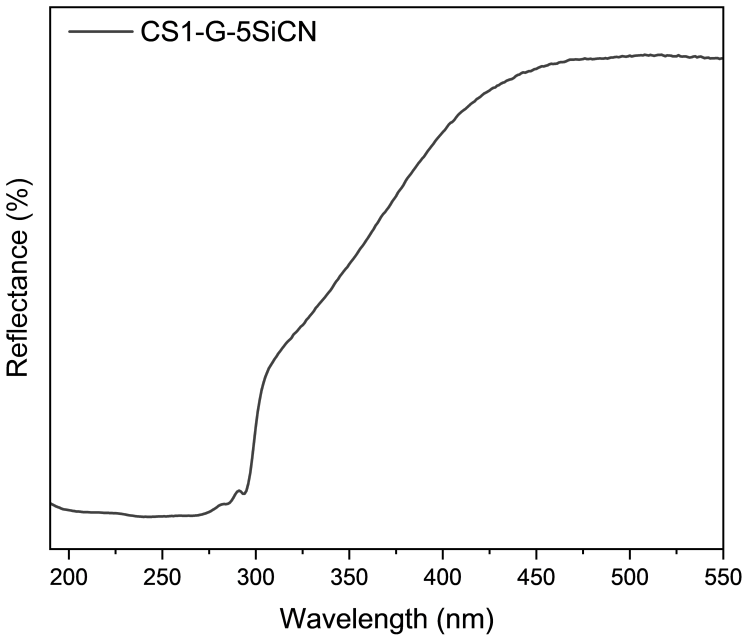

Figure 4.11: DRS spectrum of CS1-G-5SiCN

This experiment serves as a proof of concept for the development of these new photoresponsive bio-nanocomposites. However, much work remains to be done. A deep characterization of the materials is essential, including optimizing the preparation process for each system. For example, an appro-

priate solvent must be identified to dissolve the highly substituted starch samples and to process the film. The effect of the cinnamic unit, the type and content of filler, and how the degree of functionalization impacts the final properties of the material all need to be systematically studied. Additionally, the influence of the starch substitution degree on the composite's overall performance must be evaluated.

In addition, the structural, thermal, and mechanical properties, the biodegradability and compostability of the material must also be assessed, especially for its potential applications in the food packaging industry. Despite these challenges, the preliminary findings indicate that this material holds great promise for future advancements.

References

(1) Bugnotti, D.; Dalle Vacche, S.; Esposito, L. H.; Callone, E.; Orsini, S. F.; Ceccato, R.; D'Arienzo, M.; Bongiovanni, R.; Dirè, S.; Vitale, A. Structure of Starch-Sepiolite Bio-Nanocomposites: Effect of Processing and Matrix-Filler Interactions. *Polymers* **2023**, *15*, 1207, DOI: 10.3390/polym15051207.

Chapter 5

Preparation of thermo-responsive SNFs

The chapter focuses on the preparation of solvent-free nanofluids, a concept introduced deeply in the introduction. This research was conducted during a period at the Charles Gerhardt Institute in Montpellier (CNRS).

The first part of this section describes the synthesis of a guanidinium-containing silane, which was then employed in a one-step functionalization of both silica nanoparticles and sepiolite nanofibers. The success of the functionalization was confirmed through ATR-FTIR, solid-state NMR (ss-NMR), and zeta potential measurements. TGA and CHNS analyses were used to estimate the degree of functionalization.

The functionalized fillers were modified with sulfonated polyethylene glycol (sulfo-PEG). Various weight ratios of sulfo-PEG to fillers were tested to examine how the polymer-to-filler ratio affects the properties of the final system. ATR-FTIR provided preliminary insights into the composite systems, while TGA and DSC were used to study the thermal behavior of the composites in relation to the sulfo-PEG matrix and functionalized fillers. Additionally, TD-NMR was employed to evaluate molecular mobility within the nanocomposites by measuring T_2 relaxation times. This allowed differentiation between mobile and bound polymer regions, helping to assess the impact of filler loading on polymer-filler interactions. A preliminary proof of concept of thermal macroscopic behaviour is finally presented.

Together, these characterization techniques offer a comprehensive understanding of the thermal, structural, and dynamic properties of the silica and sepiolite-based composites, which is essential for optimizing their performance in application like smart lubricant.

5.1 Synthesis of guanidinium alkoxysilane

The guanidinium ion, the protonated form of guanidine, originates from guanine, a natural product found in Peruvian guano. Guanidine has an exceptionally high basicity (pKa = 13.6), surpassing hydroxide ions, pyridines, amines, and amidines. This makes guanidinium groups highly effective in participating in various biological processes, including membrane transport and channeling, making them essential in human biology. In organic chemistry, guanidines are widely used as strong organic bases and as catalysts in reactions such as the Michael reaction and the Henry reaction. With the growing advancements in organocatalysis, their role as efficient and selective catalysts has expanded significantly.[1]

Guanidinium groups, due to their strong basicity and resonance-stabilized structure, form stable noncovalent complexes with a variety of anionic species, particularly in aqueous environments. In particular, the Guanidinium-Sulfonate interactions (Figure 5.1) are particularly noteworthy due to their high affinity, which is driven by electrostatic forces, hydrogen bonding, and the complementary geometries of the interacting molecules. Sulfonate groups are commonly found in biological molecules, and their interactions with guanidinium groups, such as those present in the side chain of arginine, are crucial for processes like protein-ligand recognition and membrane transport. On the other hand, in synthetic systems, guanidinium-functionalized molecules are designed to bind strongly with sulfonate-based ligands or receptors. This interaction is often used to mimic biological systems, particularly for molecular recognition in drug development or the creation of host-guest systems.

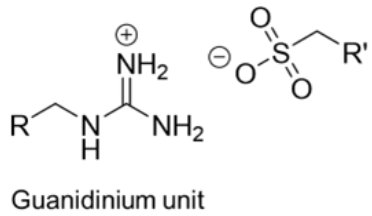

Figure 5.1: Guanidinium-Sulfonate ionic interaction

These guanidinium-sulfonate interactions are increasingly utilized in the design of molecular recognition systems, synthetic receptors, and catalysts. The stability and specificity of these interactions make them valuable in areas like drug delivery, sensor design, and catalysis. The strong acidity of sulfonate groups, which can form stable dianionic species, enhances their interactions with guanidinium, leading to more robust complexes. This characteristic makes sulfonate groups preferable in synthetic applications over carboxylates, which are more common in nature but form comparatively weaker complexes.[2, 3]

Guanidinium ions have also been used to functionalize silica nanoparticles.[4] In particular, Guodong et al.[1] synthesized these systems using a one-pot procedure, modifying the amino group of APTES. However, this one-pot procedure is characterized by low yields, which could potentially be improved by using a silane covalently bearing a guanidinium unit.

Materials

1H-Pyrazole-1-carboxamidine hydrochloride 98% (PyzCA) was purchased from Alfa Aesar. Poly(ethylene glycol) 4-nonylphenyl 3-sulfopropyl ether potassium salt (sulfo-PEG) was purchased from Sigma-Aldrich. APTES

98% was purchased from abcr. Absolute anhydrous Ethanol was purchased from VWR.

5.1.1 Experimental Procedure of GuPTES

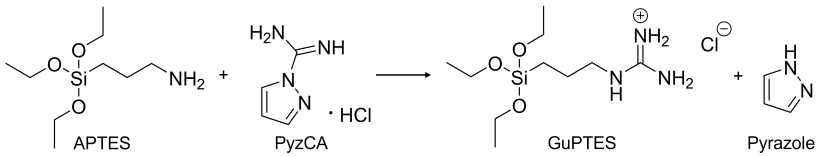

Scheme 5.1: Preparation of GuPTES

The preparation procedure of the new GuPTES organosilane is described in Scheme 5.1.
2.73 g of PyzCa was dispersed in 10.0 mL of absolute anhydrous EtOH in a Schlenk tube under an inert gas atmosphere. Then, 4.12 g of APTES was added dropwise to the dispersion. The addition of APTES resulted in heat release and the dissolution of PyzCa. The clear yellow solution was stirred at room temperature overnight. The solvent was removed using a vacuum pump, and the resulting yellow oily product was stored under inert gas.

5.1.2 Characterization of GuPTES

NMR

The characterization of the newly synthesized organosilane was carried out using ^{1}H-NMR, ^{13}C-NMR, and ^{1}H-^{13}C HSQC spectroscopy. For a comprehensive analysis, the spectrum was compared with those of two reference compounds, PyzCA and APTES (Figure 5.2).

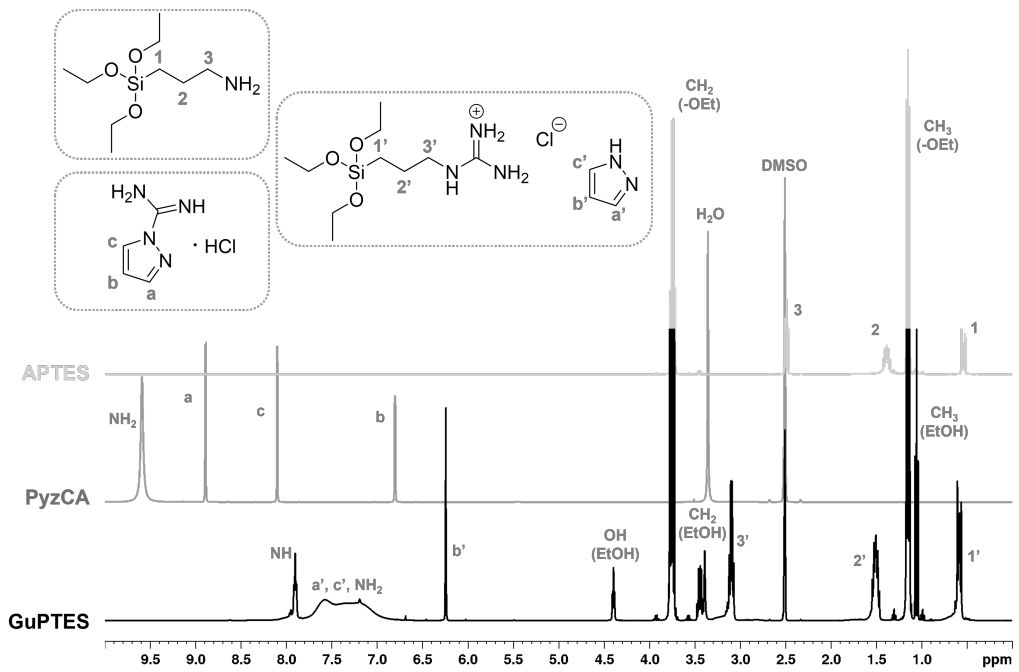

Figure 5.2: ^{1}H NMR spectra of APTES, PyzCA, and the novel GuPTES organosilane

The spectra of both PyzCA and APTES are consistent with the tabulated values found in the literature [5, 6], and their peaks were assigned accordingly. In the case of GuPTES, the signals corresponding to protons at positions 1' and 2' exhibit chemical shifts very similar to those observed for the same protons in APTES. In contrast, the protons at position 3' exhibit a downfield shift of approximately 0.6 ppm. This could indicate a modification of the amine group of APTES into a guanidinium group. In this case, the positive charge of the guanidinium group attracts the electron cloud, resulting in increased deshielding of the protons at position 3'.

Furthermore, signals related to the ethoxy groups of the silane are observed in the region between 4.5 and 0 ppm. Signals indicating significant contamination with ethanol, the reaction solvent, are also present. This suggests

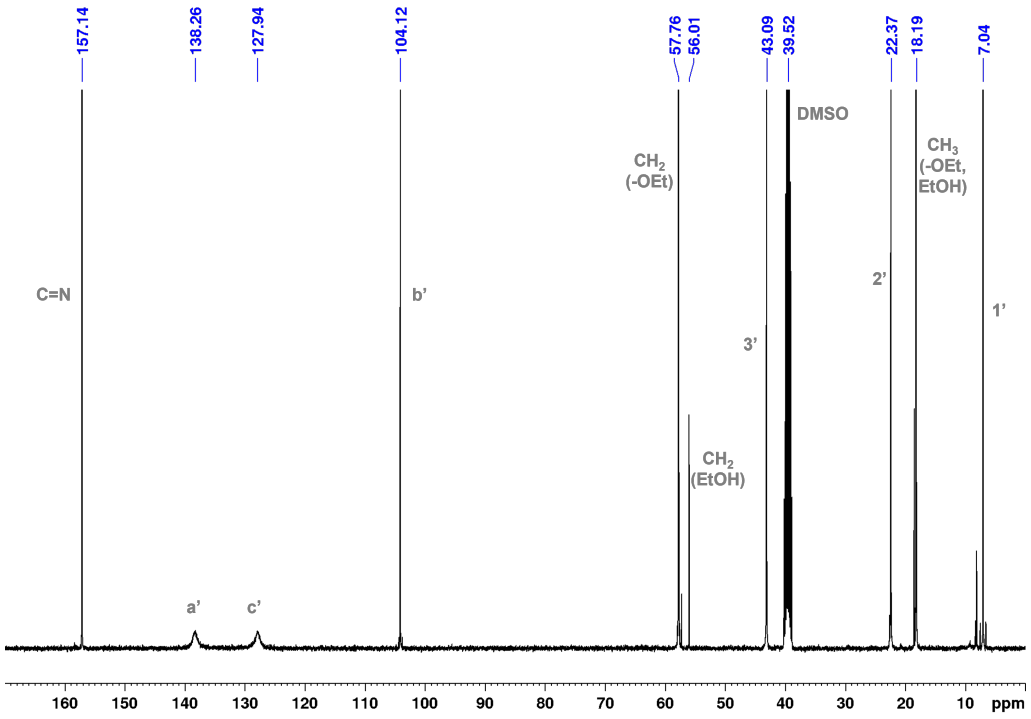

Figure 5.3: ^{13}C-NMR spectrum of GuPTES

that not all of the solvent was effectively removed from the final product or that hydrolysis of some of the ethoxy groups of silane occurred, generating ethanol molecules. This is further confirmed by the fact that the relative ratio between the integrals of the signals of the ethoxy groups of the silane and the protons of the propyl chain is lower than expected.

The signals of the by-product, pyrazole, resonate in the region between 8.0 and 6.0 ppm. The proton at position b' resonates at approximately 6.25 ppm, while the protons at positions a' and c' form two broad signals within the 8.0 to 6.5 ppm region, consistent with literature data.[7, 8] Notably, in the starting reagent, PyzCA, the same protons resonate at higher chemical shifts, which further confirms the success of the synthesis.

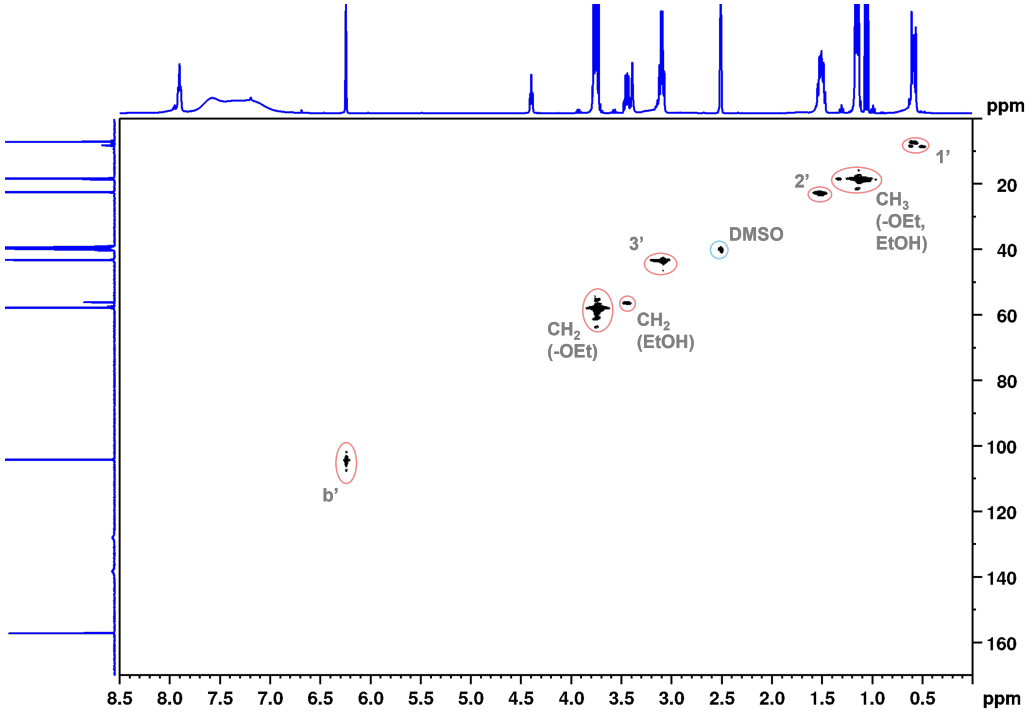

Figure 5.4: ^{1}H-^{13}C HSQC NMR spectrum of GuPTES

The signals from the NH_2 groups of the guanidinium moiety in GuPTES, as well as the proton of the NH group directly bonded to carbon at position 3', also fall within the same region. The absence of signals attributable to the starting reagents made it impossible to determine the reaction yield precisely. However, based on the outcomes, it can be estimated to be greater than 95%, indicating an excellent result for the synthesis.[9]

As further evidence of the successful synthesis of GuPTES, Figure 5.3 and Figure 5.4 show the ^{13}C NMR spectrum and the heterocorrelated HSQC 2D NMR spectrum, respectively. Using the information already obtained from the ^{1}H-NMR analysis, it was possible to assign each signal. In the ^{13}C spectrum, the most deshielded carbon is the one involved in the guanidinium unit, while the signals for carbons C-a' and C-c', which are related to the

pyrazole ring, are broader due to the fact that the nitrogen-bound proton can "jump" between the two nitrogen atoms. These same signals converge into a single signal, making the carbons at positions a' and c' equivalent when measured at higher temperatures. In the HSQC spectrum, these signals are visible only at high magnification and coincide with those described in the ^{1}H-NMR spectrum (broad signals between 8.0 and 6.5 ppm).

5.2 Preparation of guanidinium functionalized fillers

5.2.1 Experimental Procedure

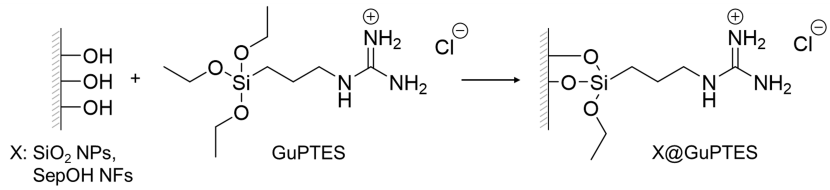

Scheme 5.2: Functionalization procedure of SiO_2 NPs and SepOH NFs

Both silica nanoparticles and sepiolite nanofibers were functionalized using the experimental procedures previously described for their functionalization with APTES. Reaction scheme is reported in Scheme 5.2. In particular, details have already been reported in sections 2.3.3.1 and 2.3.4.1. The mass of GuPTES used was calculated so that the moles of GuPTES were equal to the moles of APTES for both materials. Since GuPTES was not purified, the presence of pyrazole was also accounted for in the weighed mass, as it is stoichiometrically present with respect to GuPTES.

5.2.2 Characterization

ATR-FTIR

Infrared analysis was initially used to verify the presence of GuPTES on the surface of the fillers. Figure 5.5 show the comparison between the spectrum of GuPTES, the spectrum of the bare filler, and the spectrum of the functionalized filler.

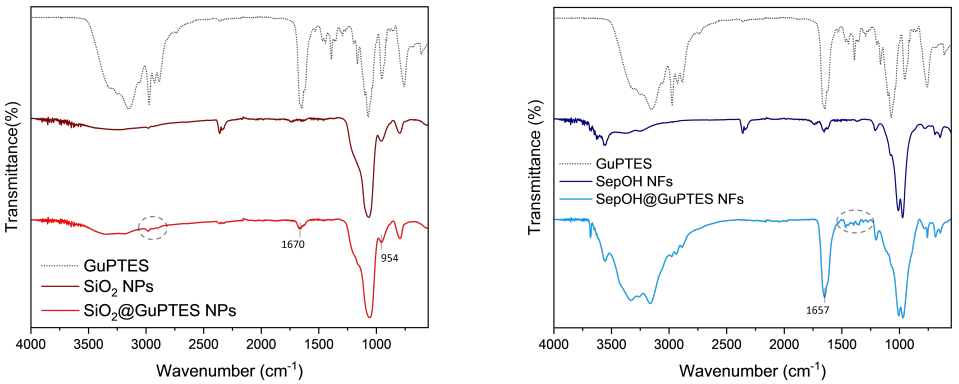

Figure 5.5: ATR-FTIR-normalized spectra of (left) GuPTES, pristine SiO_2 NPs and SiO_2@GuPTES NPs; (right) GuPTES, pristine SepOH NPs and SepOH@GuPTES NPs

Specifically, regarding the silica nanoparticles, it can be observed that following functionalization, a peak appears around 1670 cm^{-1}, which can be attributed to the C=N bond. Additionally, new signals appear around 3000 cm^{-1}, which are attributable to the propyl chain. Furthermore, a change in the lineshape of the curve can be seen in the range between 3500 and 3200 cm^{-1}, with the preliminary formation of two separate and more pronounced signals, similar to those observed in GuPTES, probably attributable to the vibration of the N-H bond.[10]

For the sepiolite nanofibers, the same signals discussed for the silica nanoparticles are also observed, with the difference that the additional signals in this case are significantly more intense. This could indicate a higher functionalization yield.

ss-NMR

The Figure 5.6 shows the ^{29}Si CPMAS spectra of the fillers, both function-

alized and unfunctionalized.

In the spectra of silica nanoparticles, the three components assigned to Q^2, Q^3, and Q^4 structural units are clearly visible. The functionalization of SiO_2 with GuPTES appears to be efficient, as indicated by the presence of T^2 and T^3 structural units at 55 and 65 ppm, respectively. The high intensity of the T units, relative to the Q units, and the low Q^3/Q^4 ratio further confirm successful functionalization.

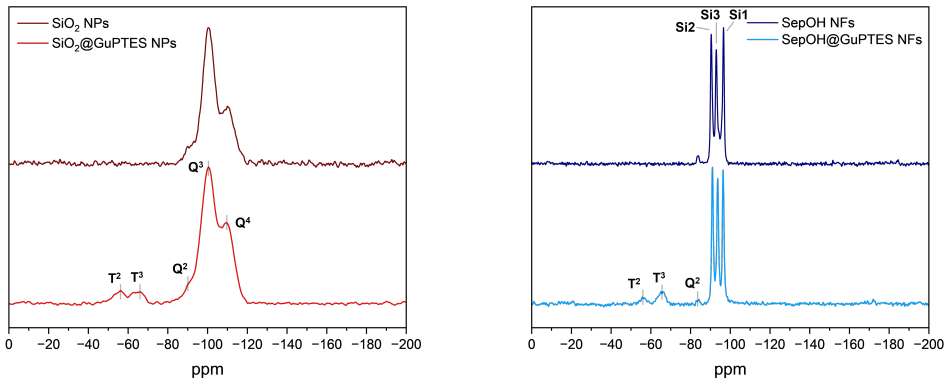

Figure 5.6: ^{29}Si CPMAS spectra of (left) pristine SiO_2 NPs and SiO_2@GuPTES NPs; (right) pristine SepOH NPs and SepOH@GuPTES NPs

According to the literature,[11] the silicon spectra of the sepiolite samples show that the sepiolite structure is characterized by four types of silicon atoms: one Q^2 and three Q^3, producing sharp and well-resolved resonances corresponding to Q^3 in different positions of the Si atom within the structure. These include the edge (Si1) at -96.6 ppm, center (Si3) at -92.9 ppm, near edge (Si2) at -90.4 ppm, and Q^2 silanols at -84 ppm (see Figure 2. 23). The functionalization of SepOH with GuPTES leads to partial consumption of the sepiolite silanols, as indicated by the reduction in the intensity of Q^2

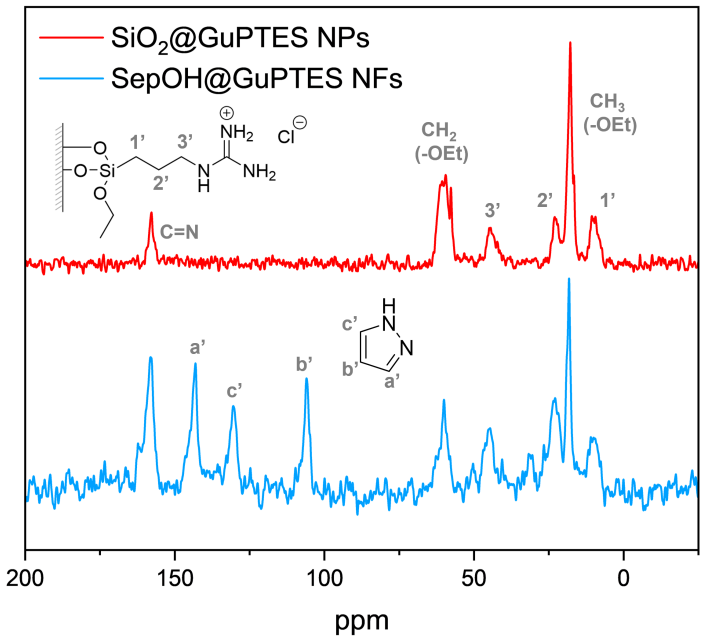

Figure 5.7: ^{13}C MAS spectra of SiO_2@GuPTES NPs and SepOH@GuPTES NFs

units and a slight alteration of the 1:1:1 Q^3 peak group. Specifically, the Si1 peak, which is located at the edges of the octahedral sheets and very close to structural water, decreases in intensity compared to bare sepiolite and exhibits a downfield shift of approximately 0.4 ppm, while Si2 and Si3 exhibit an upfield shift of about 0.6 ppm. This suggests an interaction with the silane, with partial substitution of zeolitic water inside the sepiolite channels by GuPTES molecules.[11]

Figure 5.7 shows the carbon spectra of both silica and sepiolite functionalized with GuPTES.
The assignment was performed based on the ^{13}C NMR spectrum of GuPTES (Figure 5.3). In both spectra, the resonances corresponding to the GuPTES chain are visible, along with intense peaks from unreacted ethoxy groups,

especially in SiO_2@GuPTES. Interestingly, in the SepOH@GuPTES sample, the resonances (C-a', C-b', C-c') of pyrazole, the by-product, are present,[12] whereas in SiO_2@GuPTES, only the GuPTES signals are visible. The significant intensity of the pyrazole signals indicates that the purification of the sepiolite nanofibers was insufficient for its removal, and it is highly probable that pyrazole has entered the sepiolite channels and remained adsorbed on their surface. Therefore, it is necessary to optimize the purification procedure for the sepiolite nanofibers, or even earlier, to find a method to purify GuPTES from its by-product.

ζ-potential

The mean ζ-potential values of the two different fillers, both functionalized and unfunctionalized, are summarized in the Table 5.1.

Table 5.1: ζ-potential values of bare fillers and guanidinium functionalized fillers

Sample	Silica	Sepiolite
X	-19 ± 3 mV	-20 ± 5 mV
X@GuPTES	33 ± 4 mV	39 ± 7 mV

In agreement with previous studies,[13] unmodified silica nanoparticles exhibited negative ζ-potentials in distilled water. In contrast, according to the literature,[14] sepiolite nanofibers should exhibit a positive ζ-potential at pH 7. However, these nanofibers were previously treated in a basic solution to increase the number of surface hydroxyl groups. This pretreatment might explain the negative ζ-potential value observed for bare sepiolite nanofibers. For the functionalized samples, in both cases, it was observed that the ζ-potential value became positive. This behaviour is expected due to the

guanidinium group of the compatibilizing agent. This finding further confirms the effectiveness of the functionalization reaction and the presence of a positively charged group on both fillers.

TGA

The results of the thermogravimetric analysis (TGA) are provided in the Table 5.2, and using the equations explained in the appendix, the degree of functionalization of both fillers was calculated. For the silica nanoparticles, the results were highly promising and consistent with previous observations obtained using other compatibilizing agents (CINN-APTES and APTES). In contrast, for the sepiolite nanofibers, a relatively high weight loss in the TGA was observed, which resulted in an unrealistic calculation of the degree of functionalization. Considering the solid-state NMR analysis, which shows a strong presence of pyrazole (a by-product of the GuPTES synthesis) and evidence of intercalation of material within the sepiolite channels, the degree of functionalization for sepiolite is likely overestimated.

Table 5.2: Functionalization yields (wt% and σ) of both SiO_2@GuPTES and SepOH@GuPTES

Sample	**wt.%(Y)**	σ **(n./nm^2)**
SiO_2@GuPTES NPs	6.89	1.28
SepOH@GuPTES NFs	32.84	9.43

CHNS

The elemental analyses carried out on both functionalized and non-functionalized samples of both fillers (see Table 5.3 and Table 5.4) indicate that functionalization leads to a significant increase in the percentage of both carbon

and nitrogen atoms, attributable to the presence of GuPTES. The degree of functionalization of the silica nanoparticles and sepiolite, calculated based on the carbon content and using the equations provided in the appendix, is 1.67 and 12.87 n./nm^2, respectively. These values are slightly higher than those obtained with TGA, but it must always be considered that elemental analysis also accounts for any residual solvent adsorbed on the surface that has not been completely removed. It is important to emphasize again that the functionalization result for sepiolite is likely overestimated due to the reasons previously explained.

Table 5.3: CHNS elemental analysis results for bare SiO_2 NPs and SiO_2@GuPTES NPs

Sample	**C (wt.%)**	**H (wt.%)**	**N (wt.%)**	**S (wt.%)**
SiO_2	2.46	1.314	0.83	0.133
SiO_2@GuPTES	5.54	1.614	2.49	0.226

Table 5.4: CHNS elemental analysis results for bare SepOH NFs and SepOH@GuPTES NFs

Sample	**C (wt.%)**	**H (wt.%)**	**N (wt.%)**	**S (wt.%)**
SepOH	0.24	2.096	0.62	0.17
SepOH@GuPTES	15.33	3.862	10.17	0.064

5.3 Modification of guanidinium fillers with sulfo-PEG

5.3.1 Experimental Procedure

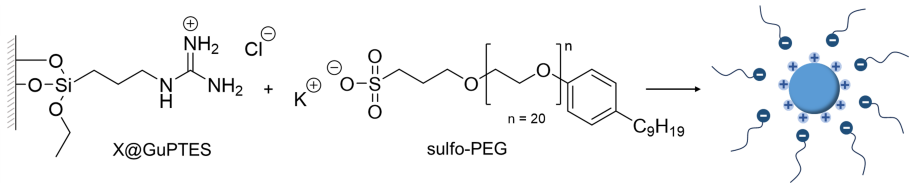

Scheme 5.3: Procedure of modification of guanidinium fillers with sulfo-PEG

100 mg of X@GuPTES NPs were dispersed in 5 mL of an aqueous sulfo-PEG solution using an ultrasonication bath. The preparation scheme is shown in Scheme 5.3. The amounts of sulfo-PEG are provided in the Table 5.5. The mixture was then heated to 70°C and maintained at this temperature for 24 hours under vigorous magnetic stirring. Afterward, the solvent was removed using a vacuum pump, and the samples were stored at room temperature.

Table 5.5: Amounts of sulfo-PEG used for the nanocomposite preparation

X	Sample	sulfo-PEG (mg)	Weight ratio	Loading
SiO_2	**SiGu-sPEG_1**	100	1:1	50 wt.%
	SiGu-sPEG_2	200	1:2	33 wt.%
	SiGu-sPEG_3	300	1:3	25 wt.%
	SiGu-sPEG_5	500	1:5	17 wt.%
Sep	**SepGu-sPEG_1**	100	1:1	50 wt.%
	SepGu-sPEG_2	200	1:2	33 wt.%
	SepGu-sPEG_3	300	1:3	25 wt.%
	SepGu-sPEG_5	500	1:5	17 wt.%

The texture of the samples is shown in Figure 5.8.

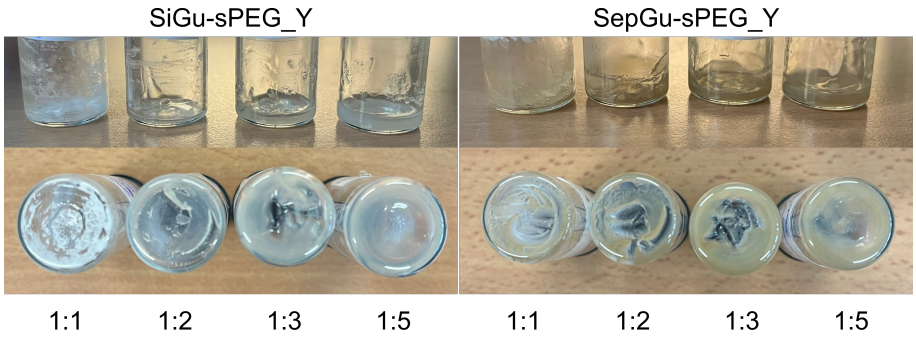

Figure 5.8: Photos of the nanocomposites

5.3.2 Characterization

ATR-FTIR

Infrared analysis performed on all samples (Figure 5.9) reveals that, for both silica nanoparticles and sepiolite nanofibers, as the filler loading in the composites decreases from 50 wt.% to 17 wt.%, the spectral features increasingly resemble those of the polymer matrix. This trend indicates a progressive loss in the ability to identify the characteristic signals of the filler materials. Specifically, at lower filler concentrations, the absorption bands associated with the silica nanoparticles and sepiolite nanofibers are gradually obscured by the dominant spectral features of the polymer.

TGA

TGA was exploited to assess the thermal stability and composition of the nanocomposites. As shown in Figure 5.10, for all silica-containing composites, except for the one with the highest loading, the decomposition tempera-

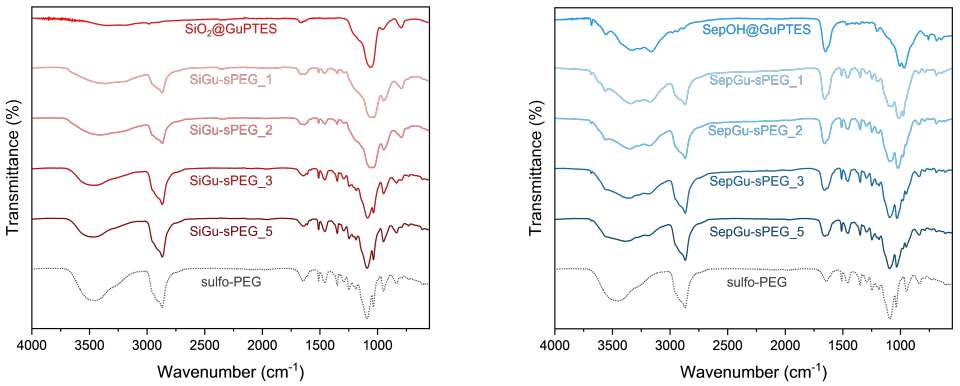

Figure 5.9: ATR-FTIR spectra of silica nanocomposites (left) and sepiolite nanocomposites (right) compared to functionalized filler and sulfo-PEG

ture increases by approximately 40 °C compared to sulfo-PEG. Furthermore, the nominal loading values (50%, 33%, 25%, 17%) correspond closely to the values calculated using the percentage of undegraded residue at 1000°C (Table 5.6).

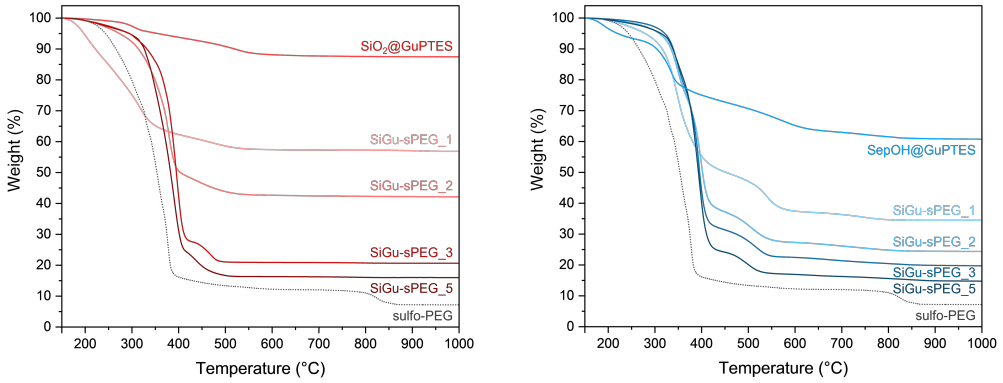

Figure 5.10: Thermograms of silica nanocomposites (left) and sepiolite nanocomposites (right) compared to functionalized filler and sulfo-PEG

Notably, for the sample with the highest loading, phase separation occurs over time, and the lack of homogeneity may explain why it begins to degrade

Table 5.6: Comparison of nominal loading and loading calculated using TGA results

X	Sample	Nominal Loading	TGA Loading
SiO_2	**SiGu-sPEG_1**	50 wt.%	57 wt.%
	SiGu-sPEG_2	33 wt.%	40 wt.%
	SiGu-sPEG_3	25 wt.%	15 wt.%
	SiGu-sPEG_5	17 wt.%	10 wt.%
Sep	**SepGu-sPEG_1**	50 wt.%	45 wt.%
	SepGu-sPEG_2	33 wt.%	28 wt.%
	SepGu-sPEG_3	25 wt.%	21 wt.%
	SepGu-sPEG_5	17 wt.%	12 wt.%

at lower temperatures. Another significant observation is the emergence of a second degradation step, particularly in the 25% and 17% samples. This can be attributed to the degradation of polymer chains directly bonded to the surface of the nanoparticles, which become more rigid and confined. This likely indicates the presence of an interface between the nanoparticles and the polymer.

In the case of sepiolite composites, an increase in degradation temperature of approximately 50°C is observed across all loadings. An higher mass loss is observed in the SepOH@GuPTES sample compared to the SiO_2@GuPTES sample. The mass loss is partly due to the decomposition of the silane (GuPTES), pyrazole intercalated within the pores, and potentially solvent trapped within the sepiolite structure. This also occurs in the composites, which is why the percentage of undegraded material at 1000°C is lower than the nominal loading.

Additionally, unlike the silica composites, a second degradation step is observed in all sepiolite samples, even at lower loadings. This behavior is likely caused by interfacial interactions, as well as the polymer being intercalated

within the sepiolite channels, which "delays" its degradation.

DSC

DSC measurements were performed to study the thermal behavior of the raw materials and the composites. The samples were first heated to 180°C to eliminate the thermal history of the materials, cooled to -80°C, and then subjected to a final heating cycle up to 180°C. The results from this final heating phase are shown in Figure 5.11 and Figure 5.12, corresponding to silica and sepiolite composites, respectively. The thermograms of the composites were compared with those of sulfo-PEG and the initial functionalized fillers.

In the case of sulfo-PEG, the glass transition temperature (Tg) occurs around -20°C. Due to the low molecular weight of the polymer, this Tg is lower than that of medium- and high-molecular-weight PEGs. An additional endothermic signal around 35°C corresponds to the melting of the polymer's crystalline domains, consistent with the behavior reported in the literature for low-molecular-weight PEG samples.[15]

A similar melting signal is observed in all composites containing functionalized silica. In samples with higher silica content (50% and 33%), the melting peak broadens, likely due to increased amounts of silica influencing the variation in crystallite sizes. Additionally, an endothermic relaxation around 70°C suggests internal structural relaxation, caused by changes in the spatial arrangement of the polymer chains. These changes are reflected in temperature shifts, indicating modifications in the polymer chain organi-

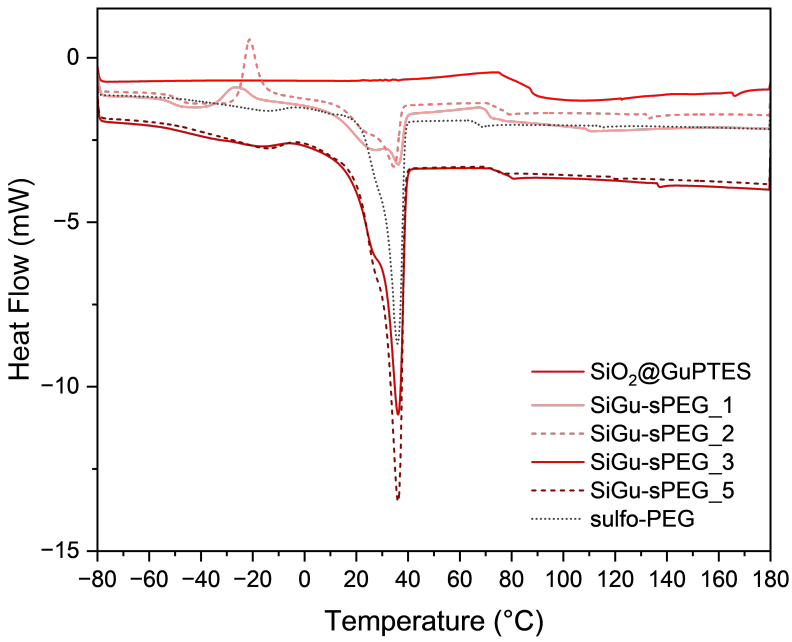

Figure 5.11: DSC curves of SiO_2@GuPTES, sulfo-PEG and silica nanocomposites

zation due to the presence of silica.

For composites with higher silica loading, an additional exothermic peak around -20°C is observed, likely due to structural relaxation, which enhances heat emission. This may result from the formation of distinct polymeric domains between the silica nanoparticles. In sepiolite composites, a similar thermal trend is observed, further amplified by the anisotropy of sepiolite and its ability to self-assemble into network structures, forming confined polymer domains.[16] Additionally, sepiolite's porosity may allow the polymer to channel through its structure, shifting the melting peak to lower temperatures compared to sulfo-PEG. In the sample with lower sepiolite loading (17%), a splitting of the melting peak is observed, likely due to the presence

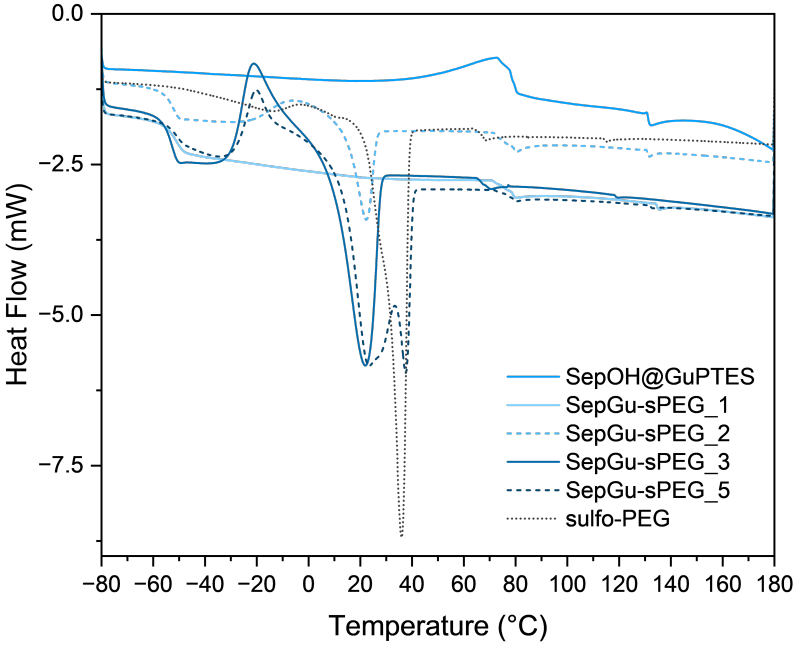

Figure 5.12: DSC curves of SepOH@GuPTES, sulfo-PEG and sepiolite nanocomposites

of both free polymer and surface-bound polymer trapped between sepiolite fibers and within its channels. The broadening of the peaks is attributed to the formation of crystalline domains of varying sizes within the composite.

HE TD-NMR

Relaxation times are closely linked to molecular motion regimes in materials, with trends affected by factors such as molecular mobility, temperature, and material composition. These parameters are interrelated through the correlation time (τ_c), which represents the time required for molecules to undergo conformational changes. The relationship between relaxation times and the logarithm of the correlation time is depicted in the accompanying Figure

5.13. Two key types of relaxation times are typically observed: longitudinal spin-reticulum relaxation time (T_1) and transverse spin-spin relaxation time (T_2), which correspond to distinct relaxation mechanisms.

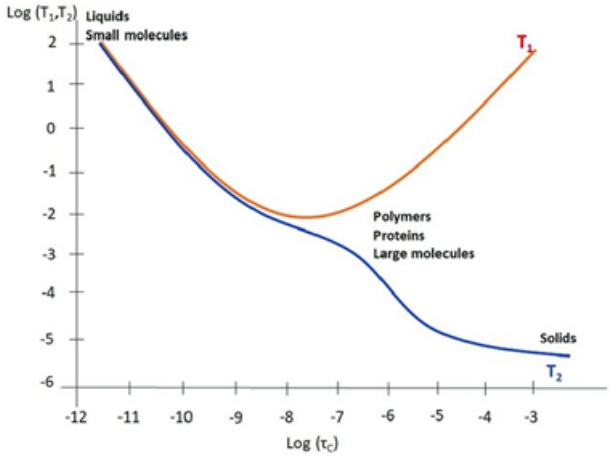

Figure 5.13: Behavior of T_1 and T_2 as a function of correlation time (in double-log scale) for $\frac{1}{2}$ spins[17]

The transverse spin-spin relaxation time (T_2) was measured using the Hahn Echo (HE) pulse sequence in this study. Initially, T_2 values are relatively high but decrease to a plateau in the region corresponding to rigid materials or solids, which have higher correlation times. In rigid materials, spin-spin interactions become more pronounced, leading to rapid phase coherence loss and faster cancellation of transverse magnetization.[17]

In this study, the Hahn Echo (HE) sequence was used to assess the T_2 relaxation time of the composite. While T_1 is generally more suitable for studying the interaction between the spin and the lattice (reticulum), T_2 also provides valuable information about the direct interactions between different proton populations within the components. The aim was to distinguish the various

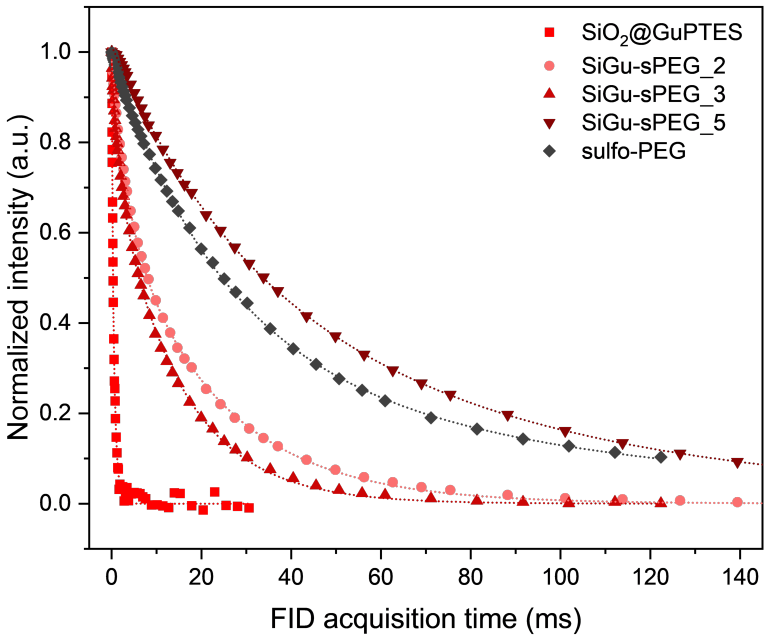

Figure 5.14: T_2 trends and two-component exponential function of SiO_2@GuPTES, sulfo-PEG and silica nanocomposites

contributions from these proton populations and evaluate the presence of an interphase between the filler and the sulfo-PEG matrix. This analysis aids in understanding the material's structural dynamics and the potential interactions at the filler-polymer interface.

For this analysis, it was decided to focus only on the three nanocomposites with the highest loadings, excluding the sample with a 50 wt.% loading. This exclusion was made because, even at the macroscopic level, significant inhomogeneities were observed in the 50 wt.% sample, with phase-separated zones. This high loading prevented the nanoparticles from exhibiting liquid-like behavior, while the generation of sticky agglomerates prevails. These agglomerates compromise the uniform distribution of the nanoparticles within

the matrix, negatively affecting the material's overall properties and performance.

Figure 5.14 illustrates the transverse relaxation trends for the silica composites, comparing them with pure sulfo-PEG and the functionalized nanoparticles (SiO_2@GuPTES). For all samples, the relaxation data is well-represented by a two-component exponential function (Equation 5.1).

$$y = y0 + A1 \cdot exp^{-\frac{x}{t1}} + A2 \cdot exp^{-\frac{x}{t2}} \tag{5.1}$$

This model indicates the presence of two distinct proton populations: one that is more mobile and another that is more constraint. The Table 5.7 presents the results of the bi-component exponential fit for each sample, with y0 fixed at *zero* across all samples. The R^2 coefficient shows optimal values for most samples, confirming the accuracy of the model, except in the case of the SiO_2@GuPTES powder, where the relaxation trend displays a non-uniform behaviour. This anomaly suggests variability in the relaxation dynamics of the powder, potentially due to heterogeneous proton environments or variations in nanoparticle interactions.

Table 5.7: Two-component exponential function parameter of SiO_2@GuPTES, sulfo-PEG and silica nanocomposites

Sample	A1	t1	A2	t2	R^2
NPs	0.40 ± 0.08	0.17 ± 0.04	0.72 ± 0.09	0.64 ± 0.05	0.99793
Si1:2	0.31 ± 0.01	3.5 ± 0.2	0.67 ± 0.01	22.3 ± 0.4	0.99976
Si1:3	0.24 ± 0.01	1.8 ± 0.1	0.74 ± 0.01	14.8 ± 0.3	0.99952
Si1:5	0.48 ± 0.06	30 ± 2	0.53 ± 0.06	78 ± 4	0.99984
sPEG	0.68 ± 0.04	24.8 ± 0.9	0.32 ± 0.04	101 ± 10	0.99983

Notably, the sulfo-PEG polymer itself displays two distinct components: a

less mobile component with a T_2 of 25 ms and a more mobile one with a T_2 of 101 ms, indicating possible inhomogeneity in the proton population. When SiO_2@GuPTES nanoparticles are introduced, this two-component inhomogeneity remains but with significant shifts in relaxation times for both the mobile and constrained components. For instance, in the SiGu-sPEG_2 sample, the more rigid component has a T_2 of 3.5 ms, while the more mobile component shows a T_2 of 22.3 ms. A similar trend is observed in the SiGu-sPEG_3 sample (as shown in Table 5.7). These shifts likely result from a highly restricted interfacial region caused by ionic interactions between the nanoparticles and the polymer chains.

The persistence of two components as the system transitions from pure polymer to composite suggests the formation of a stable interface between the filler and the polymer, likely driven by ionic interactions. If no such interactions were present, additional components would likely appear, reflecting the independent behavior of the polymer and the filler.

However, this trend is not consistent across all samples. For example, the SiGu-sPEG_5 sample (17% loading) exhibits higher mobility than the pure polymer, which may indicate phase separation within the system or the presence of both free polymer and polymer bound to the filler surface. Additionally, composites loaded with 33% and 25% of filler exhibit an unexpected behavior, with lower loading leading to higher stiffness. This deviation from theoretical expectations may be due to mass inhomogeneities introduced during sample preparation.

For the sepiolite composites, a clear relationship between increasing sulfo-

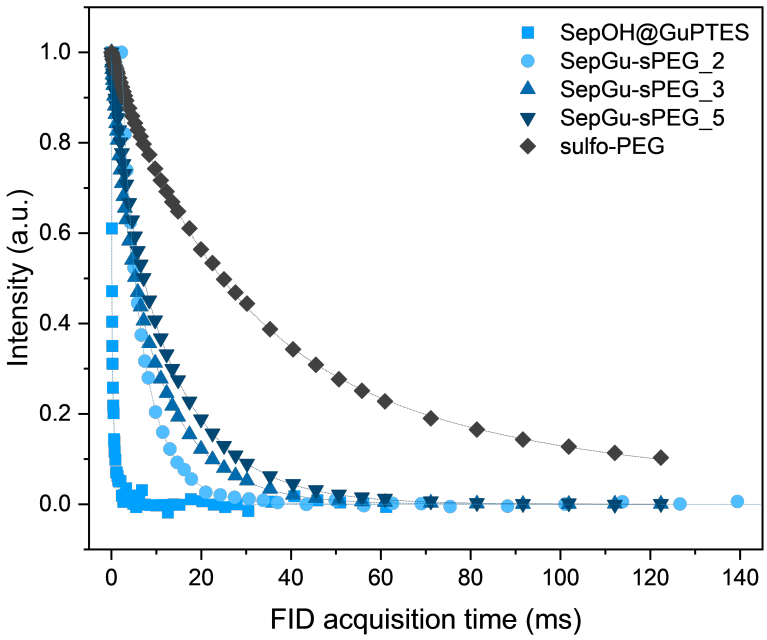

Figure 5.15: T_2 trends and two-component exponential function of SepOH@GuPTES, sulfo-PEG and sepiolite nanocomposites

PEG chain weight fraction and enhanced mobility is observed, with lower filler loading resulting in lower stiffness (as shown in Figure 5.15). Similar to the silica composites, a two-component behavior is present in all sepiolite composites, supported by excellent R^2 values (Table 5.8), suggesting the formation of ionic interactions between the filler and the polymer. The significant shift in relaxation times between the mobile and constrained components from pure sulfo-PEG to the composite further confirms the presence of a strong nanoparticle-polymer interface. In this case, the relaxation trends correlate well with the nanoparticle loading, indicating that sepiolite composites are particularly promising for applications requiring fine-tuned mobility and robust interfacial interactions. Additionally, it should be noted that the polymer, as previously observed, intercalates within the sepiolite

structure, further contributing to the reduction of sulfo-PEG chain mobility.

Table 5.8: Two-component exponential function parameter of SepOH@GuPTES, sulfo-PEG and sepiolite nanocomposites

Sample	A1	t1	A2	t2	R^2
NFs	1.38 ± 0.09	0.046 ± 0.004	0.44 ± 0.02	0.60 ± 0.04	0.9944
Sep1:2	0.94 ± 0.09	2.4 ± 0.3	0.9 ± 0.1	6.5 ± 0.35	0.99975
Sep1:3	0.28 ± 0.01	3.0 ± 0.1	0.72 ± 0.01	11.3 ± 0.2	0.99995
Sep1:5	0.22 ± 0.01	3.9 ± 0.2	0.78 ± 0.01	14.0 ± 0.1	0.99997
sPEG	0.68 ± 0.04	24.8 ± 0.9	0.32 ± 0.04	101 ± 10	0.99983

Macroscopical Thermo-responsive Properties

An initial attempt was made to assess the thermoresponsive properties of the material.[18] At room temperature, the system exhibits a highly viscous texture. However, when the temperature is increased to 70°C, a decrease in viscosity is observed, and the composite becomes more transparent. Notably, this behavior is fully reversible, when the system cools back to room temperature, it regains its original viscosity and opacity. This thermal cycling process was repeated multiple times, consistently demonstrating the material's thermoresponsive performance. Figure 5.16 shows the sample SiGu-sPEG_2 before and after the thermal treatment at 70°C.

To better understand the underlying mechanisms at play, further analysis is needed to explore the structural changes occurring within the system. In future studies, ^{1}H Time-Domain Nuclear Magnetic Resonance (^{1}H TD-NMR) experiments will be performed at different temperatures to investigate how polymer chain mobility varies as a function of temperature. Additionally, Small Angle X-ray Scattering (SAXS) is planned to analyze how the polymer

Figure 5.16: Photos of SiGu-sPEG_2 before (left) and after (right) thermal treatment at 70°C

organizes itself in the presence and absence of silica and sepiolite nanoparticles, providing insight into the material's microstructural arrangement and interactions.

Moreover, a priority for future work will be the removal of pyrazole, a by-product of the GuPTES synthesis that remains into sepiolite structure, to study its impact on the system in more detail. The removal of this by-product will be crucial for optimizing the material's performance and ensuring its long-term stability.

In summary, these systems exhibit significant potential for applications requiring thermoresponsive properties. The ability to fine-tune viscosity and transparency with temperature change could be useful in a variety of fields, in particular for smart lubricant application. Further investigation into the molecular and structural dynamics will help unlock new possibilities for these thermoresponsive SNFs.

References

(1) Guodong, F.; Mingming, G.; Qi, L.; Hongyu, M.; Guanghua, L.; Qiang, M.; Qiang, F.; Yanfu, H.; Zhiguang, S. One-pot synthesis and application of novel amino-functionalized silica nanoparticles using guanidine as amino group. *New Journal of Chemistry* **2016**, *40*, 8444–8450, DOI: 10.1039/C6NJ02094A.

(2) Butschies, M.; Frey, W.; Laschat, S. Designer Ionic Liquid Crystals Based on Congruently Shaped Guanidinium Sulfonates. *Chemistry - A European Journal* **2012**, *18*, 3014–3022, DOI: 10.1002/chem.201101925.

(3) Schug, K. A.; Lindner, W. Noncovalent Binding between Guanidinium and Anionic Groups. *Chemical Reviews* **2005**, *105*, 67–114, DOI: 10.1021/cr040603j.

(4) Dadashev, A.; Tertykh, V.; Yanovska, E.; Yanova, K. New Approach to Synthesis of Silica with Chemically Bound Guanidine Hydrochloride for Preconcentration of Metal Ions. *American Journal of Analytical Chemistry* **2016**, *7*, 411–420, DOI: 10.4236/ajac.2016.75038.

(5) Jung, H.-S.; Moon, D.-S.; Lee, J.-K. Quantitative Analysis and Efficient Surface Modification of Silica Nanoparticles. *Journal of Nanomaterials* **2012**, *2012*, 593471, DOI: 10.1155/2012/593471.

(6) Zhao, J.; Jin, B.; Peng, R.; Liu, Q.; Tan, B.; Chu, S. Synthesis and characterization of a new energetic salt 1H-pyrazole-1-carboxamidine dinitramide and its thermal properties. *Journal of Thermal Analysis and Calorimetry* **2016**, *124*, 1431–1439, DOI: 10.1007/s10973-016-5315-z.

(7) Fulmer, G. R.; Miller, A. J. M.; Sherden, N. H.; Gottlieb, H. E.; Nudelman, A.; Stoltz, B. M.; Bercaw, J. E.; Goldberg, K. I. NMR Chemical Shifts of Trace Impurities: Common Laboratory Solvents, Organics, and Gases in Deuterated Solvents Relevant to the Organometallic Chemist. *Organometallics* **2010**, *29*, 2176–2179, DOI: 10.1021/om100106e.

(8) NMR Chemical Shift Values Table - Chemistry Steps https://www.chemistrysteps.com/nmr-chemical-shift-values-table/ (accessed 10/26/2024).

(9) Litchman, W. M. Proton exchange and temperature studies of pyrazole in dimethyl-d6 sulfoxide by carbon-13 NMR. *Journal of the American Chemical Society* **1979**, *101*, 545–547, DOI: 10.1021/ja00497a008.

(10) Drozd, M. Molecular structure and infrared spectra of guanidinium cation: A combined theoretical and spectroscopic study. *Materials Science and Engineering: B* **2007**, *136*, 20–28, DOI: 10.1016/j.mseb.2006.08.063.

(11) Bugnotti, D.; Dalle Vacche, S.; Esposito, L. H.; Callone, E.; Orsini, S. F.; Ceccato, R.; D'Arienzo, M.; Bongiovanni, R.; Dirè, S.; Vitale, A. Structure of Starch-Sepiolite Bio-Nanocomposites: Effect of Processing and Matrix-Filler Interactions. *Polymers* **2023**, *15*, 1207, DOI: 10.3390/polym15051207.

(12) Lopez, C.; Claramunt, R. M.; Trofimenko, S.; Elguero, J. A 13C NMR spectroscopy study of the structure of N-H pyrazoles and indazoles. *Canadian Journal of Chemistry* **1993**, *71*, 678–684, DOI: 10.1139/v93-092.

(13) Branda, F.; Silvestri, B.; Costantini, A.; Luciani, G. Effect of exposure to growth media on size and surface charge of silica based Stöber nanoparticles: a DLS and ζ-potential study. *Journal of Sol-Gel Science and Technology* **2015**, *73*, 54–61, DOI: 10.1007/s10971-014-3494-2.

(14) Alkan, M.; Tekin, G.; Namli, H. FTIR and zeta potential measurements of sepiolite treated with some organosilanes. *Microporous and Mesoporous Materials* **2005**, *84*, 75–83, DOI: 10.1016/j.micromeso.2005.05.016.

(15) Pielichowski, K.; Flejtuch, K. Differential scanning calorimetry studies on poly(ethylene glycol) with different molecular weights for thermal energy storage materials. *Polymers for Advanced Technologies* **2002**, *13*, 690–696, DOI: 10.1002/pat.276.

(16) Di Credico, B.; Cobani, E.; Callone, E.; Conzatti, L.; Cristofori, D.; D'Arienzo, M.; Dirè, S.; Giannini, L.; Hanel, T.; Scotti, R.; Stagnaro, P.; Tadiello, L.; Morazzoni, F. Size-controlled self-assembly of anisotropic sepiolite fibers in rubber nanocomposites. *Applied Clay Science* **2018**, *152*, 51–64, DOI: 10.1016/j.clay.2017.10.032.

(17) Besghini, D.; Mauri, M.; Simonutti, R. Time Domain NMR in Polymer Science: From the Laboratory to the Industry. *Applied Sciences* **2019**, *9*, 1801, DOI: 10.3390/app9091801.

(18) Du, P.; Liu, D.; Yuan, P.; Deng, L.; Wang, S.; Zhou, J.; Zhong, X. Controlling the macroscopic liquid-like behaviour of halloysite-based solvent-free nanofluids via a facile core pretreatment. *Applied Clay Science* **2018**, *156*, 126–133, DOI: 10.1016/j.clay.2018.01.037.

Chapter 6

Conclusions

The present work is focused on the **development of novel stimuli-responsive filler materials for smart composite applications**. The key findings from each experimental attempt and the potential perspectives are briefly summarized below referring to the relative chapter of the thesis.

Chapter 2 explored the development of **light-responsive fillers** using silica nanoparticles (SiO_2 NPs) and sepiolite nanofibers (Sep NFs). Two types of **photoresponsive units**, capable of undergoing reversible $2\pi + 2\pi$ cycloaddition reactions, were employed. The **cinnamic unit** was anchored to the silica nanoparticles through two different approaches: (1) a **one-step** functionalization using CINN-APTES, a newly synthesized alkoxysilane, and (2) a **two-step** method involving pre-grafted APTES groups, followed by modification with cinnamic derivatives (CINN-NHS or CNCOCl). The results showed that, in any case, the **one-step method enables to achieve the highest functionalization yield**, while the success of the two-step method depends on the reactivity of the starting molecule, with CNCOCl proving to be more effective than CINN-NHS. Preliminary tests confirm the photoresponsive behavior of these fillers, indicating their potential for integration into polymer matrices functionalized with the same units. Additionally, an initial attempt to functionalize SiO_2 NPs with **coumarin units** using a two-step procedure was also carried out and the performance preliminary assessed. Further endeavours will be devoted to scale-up the preparation of the filler bearing the CINN groups as well as to optimize the functionalization procedure with coumarin derivatives.

Chapter 3 detailed the **successful modification of starch through etherification with cinnamyl chloride**, resulting in varying degrees of

substitution depending on the reaction conditions. This produces photoresponsive crosslinking units as pendant groups on the polymer chains. The degree of substitution affects the solubility and processability of the starch, which is relevant for its application. For example, samples with the lowest degree of substitution can form **free-standing films under biocompatible conditions**. The photoresponsive behavior of these modified starches was preliminarily evaluated using UV-Vis spectroscopy and solution-phase NMR. UV-Vis analysis revealed a decrease in the absorbance of the functionalized starch sample when irradiated at 365 nm. This trend continued even after irradiation at 254 nm, which was unexpected; normally, absorbance should increase at 254 nm as the original molecule is expected to reform. NMR indicated that irradiation at 365 nm prompts competition between the isomerization and dimerization reactions. Irradiation at 254 nm highlights sample degradation. Further studies are needed to achieve selective photodimerization at 365 nm and to explore an experimental setup that would break the cyclobutane linkage without degrading the starch itself. Despite these challenges, the results are promising, showcasing the efficacy of this methodological approach in developing a bio-based, light-responsive system with potential applications in packaging products.

Chapter 4 described the firsts attempts to create a bio-nanocomposite using low-substitution starch developed in Chapter 3 and SiO_2 nanoparticles functionalized with CINN-APTES synthesized as reported in Chapter 2. Diffuse Reflectance Spectroscopy (DRS) was employed to confirm the UV-Vis absorption properties of this film. This preliminary work lays the foundation for the development of **photoresponsive nanocomposites**, with potential applications in smart packaging. Considerable further research is required

to optimize film preparation, especially for the starch samples with higher degrees of substitution, which are water-insoluble. Other essential factors include examining how the starch substitution degree, filler functionalization yield and aspect ratio affect the nanocomposite's structural, thermal, mechanical, photoresponsive, and biodegradable properties. Another important goal will be to optimize the preparation of fillers, the modification of starch, and the film production process by using greener solvents. This approach aims to create composites with more sustainable components and eco-friendly film-forming methods. These elements are crucial, particularly for applications in food packaging. While challenges remain, the initial findings indicate promising avenues for future development.

Finally, **Chapter 5** focused on the design of **thermoresponsive solvent-free nanofluids** for use in smart lubricants. SiO_2 NPs and Sep NFs were functionalized with a newly synthesized silane containing a **guanidinium unit (GuPTES)**. After confirming and quantifying the functionalization of both fillers, they were further modified with **sulfo-PEG** chains. The interaction between the nanoparticles and sulfo-PEG chains was primarily confirmed by HE TD-NMR, where the composites consistently exhibited a two-component exponential function, similar to sulfo-PEG alone. This finding indicates that the composites have a stable strong interface between the components. The thermoresponsive properties of the system were investigated using DSC and macroscopic observations, which suggest that temperature-induced rearrangement of the chains affects both viscosity and transparency of the SNFs. These preliminary results will be further explored using HE TD-NMR analyses to study how the mobility of proton populations within the system changes at different temperatures. Additional work is needed

to remove pyrazole, a byproduct of GuPTES synthesis, from functionalized sepiolite to accurately assess the properties of sepiolite nanocomposites without interference. These systems show considerable potential for applications requiring thermoresponsiveness, such as in smart lubricants.

In summary, all the materials developed demonstrated **promising stimuli-responsive behaviors**, indicating a significant potential for use in smart packaging and lubricant applications. Future research should focus on optimizing and thoroughly characterizing these nanocomposites, enhancing their long-term stability and performance in industrial settings, and expanding the range of stimuli-responsive functionalities. Additionally, exploring environmentally sustainable and biodegradable materials will be crucial for realizing the eco-friendly advanced composites.

Appendix A

Characterization methods

A.1 Liquid state NMR

Nuclear Magnetic Resonance (NMR) is a widely used spectroscopic technique for determining molecular structures in solution. It is non-destructive, and its sensitivity depends on factors such as the abundance of isotopes and their magnetic moments. In an applied magnetic field, nuclei with spin quantum number III have different energy levels, and for nuclei with spin 1/2 (e.g., ^{1}H or ^{13}C), these levels depend on the magnetic field strength and the gyromagnetic ratio.

Modern NMR spectrometers use radiofrequency pulses to excite nuclei, and Fourier transform is applied to convert the resulting data from the time domain to the frequency domain, identifying transitions between energy levels. Chemical shifts (δ) are used to describe the local magnetic environment of a nucleus, measured relative to a reference compound like tetramethylsilane (TMS). Shielded nuclei have chemical shifts ($\delta<0$) at higher magnetic fields, while deshielded nuclei ($\delta>0$) appear at lower magnetic fields.

Spin-spin coupling between neighboring nuclei results in multiplet patterns, providing additional structural information. The integrated intensity of a signal is proportional to the number of equivalent nuclei, which aids in spectral assignments. NMR experiments, including ^{1}H, ^{13}C, and HSQC, are performed in solvents like $CDCl_3$ or DMSO-d6 at room temperature using a Bruker Avance 400WB spectrometer at 400.13 MHz, providing detailed insights into the molecular structure and interactions.

A.2 Solid state NMR

Solid-state nuclear magnetic resonance (ss-NMR) spectroscopy is a specialized type of NMR characterized by the presence of anisotropic interactions within solid samples. To enhance spectral resolution, magic-angle spinning (MAS) is commonly employed in ss-NMR experiments. In MAS, the sample is rapidly spun at an angle of approximately 54.74°, known as the magic angle, with respect to the direction of the external magnetic field. By spinning at frequencies ranging from 1 to 100 kHz, this technique effectively averages out anisotropic interactions, resulting in narrower spectral lines and significantly improved resolution, allowing for more precise identification and analysis of the solid-state spectrum.

Solid state Magic Angle Spinning (MAS) NMR analyses were carried out with a Bruker 400WB spectrometer operating at a proton frequency of 400.13 MHz. Spectra were acquired with single (SP) or cross polarization (CP) pulse sequence under the following conditions: ^{29}Si frequency: 79.48 MHz, contact time 10 ms, decoupling length 6.8 μs, recycle delay: 10 s, 5k scans. ^{13}C frequency: 100.48 MHz, contact time 1.5 ms, decoupling length 5.6 μs, recycle delay 3 s, 2 k scans. Samples were packed in 4 mm zirconia rotors, which were spun at 6 kHz under air flow. Adamantane and Q8M8 were used as external secondary references. The Si structural units are labeled according to the usual NMR notation: Tn and Qn indicate R-SiO_3 and SiO_4 silicon units, respectively, and n is the number of oxo-bridges. Bruker TopSpin software was used for the lineshape analysis. The results were considered acceptable with a confidence level >95%.

A.3 ATR-FTIR

The surface chemistry of the analyzed materials was qualitatively characterized using vibrational spectroscopy. The absorption of infrared radiation at various wavelengths corresponds to the vibrational modes of different chemical bonds. Attenuated Total Reflectance (ATR) spectroscopy operates based on the principle of total internal reflection within a crystal. When the angle of incidence at the interface between the crystal and the sample exceeds the critical angle, total internal reflection occurs, causing the radiation to penetrate slightly beyond the reflecting surface. When the sample is in direct contact with this surface, energy is absorbed at specific wavelengths where the material interacts with the radiation. This absorbed energy is then measured and plotted as a function of wavelength.

ATR measurements were conducted at room temperature using a ThermoFisher Nicolet iS20 instrument, with a spectral resolution of 4 cm^{-1} and 64 scans in the range of 4000–550 cm^{-1}. The resulting ATR-FTIR spectra were processed using OMNIC software, which included background subtraction and baseline correction to ensure accurate spectral interpretation.

A.4 UV-Vis Spectroscopy

UV-Vis spectroscopy is an analytical technique used for both qualitative and quantitative analysis, focusing on the interaction between a solution-phase sample and electromagnetic radiation within the wavelength range of 190 to 900 nm. In this range, the absorption of electromagnetic radiation results in valence electron transitions and bond formation, and is directly propor-

tional to the concentration of molecules in the sample. This relationship is described by the Lambert-Beer law, which establishes a linear correlation between concentration and absorbance (A):

$$T = \frac{P}{P_0}, A = -log_{10}(T) = log_{10}(\frac{P}{P_0}), A_\lambda = \epsilon_\lambda bc$$

where T represents transmittance, P is the transmitted radiation, P0 is the incident radiation, ϵ_λ is the molar extinction coefficient specific to each molecule, b is the optical path length, and c is the concentration. The Lambert-Beer law is valid for monochromatic radiation and is applicable only to dilute solutions (less than 0.01 M) and in the absence of electrolytes, as electrostatic interactions can cause deviations from linearity.

UV-Vis spectroscopy also provides qualitative information about the presence or absence of functional groups that absorb radiation within the range of 180 to 1000 nm. The absorption spectra and kinetic analyses were carried out using a UV-Vis Cary 60 spectrophotometer and a 5 mm cuvette.

A.5 DRS spectroscopy

Diffuse reflectance spectroscopy (DRS) is a surface analysis technique that employs UV-Visible radiation to gather information about the structural characterization and optoelectronic properties of solid-state samples. It specifically measures the light scattered by the sample when exposed to radiation in the 200 to 800 nm range and represents it as a percentage of reflectance. In general, light scattering (R) is always accompanied by absorption (A) and transmission (T) phenomena, adhering to the following

law:

$$A + T + R = 1$$

Similar to UV-Vis spectroscopy, the interaction between electromagnetic radiation and the material in DRS results in electronic transitions involving both bond and valence electrons.

The instrument used in this study was a Perkin Elmer Lambda 1050+ UV/Vis/NIR spectrophotometer, which consists of a light source, a diffraction grating monochromator, a sample holder, and a detector. The powders were dispersed in EtOH and drop-casted on a quartz slide. The resulting spectrum is presented as percent reflectance (R%) as a function of wavelength.

A.6 DSC

Differential Scanning Calorimetry (DSC) is a thermal analysis technique used to measure the heat flow associated with material transitions as a function of temperature. In DSC analysis, both a sample and a reference are heated or cooled simultaneously, and the difference in energy required to maintain the same temperature between them is recorded. This enables the determination of thermal events such as melting, crystallization, glass transitions, and decomposition. The technique is commonly employed to characterize the thermal properties of various materials, including polymers, metals, and ceramics, providing valuable information on thermal stability, phase transitions, and heat capacity.

In this study, an initial heating ramp was performed up to 180°C to erase the sample's thermal history. The sample was then cooled to -80°C, followed by reheating to 180°C. The curves presented in the graphs represent only the final heating ramp. The measurements were carried out using a Mettler Toledo DSC Stare instrument, ensuring precise control and analysis of the thermal transitions.

A.7 TEM

Transmission Electron Microscopy (TEM) is a powerful technique for morphological characterization of nanostructured materials, offering much higher resolution than Scanning Electron Microscopy (SEM). TEM analysis utilizes a high-energy electron beam, which can be accelerated up to 300 kV, and a series of electromagnetic lenses to achieve high-resolution imaging. The sample, typically supported on a 3 mm copper grid, is exposed to the electron beam, which interacts with the material and produces transmitted and elastically scattered electrons. These electrons form a diffraction pattern, which is then reconstructed by a projection lens into a two-dimensional image of the sample.

TEM can effectively resolve fine details, making it suitable for analyzing powders, nanostructured materials, and ultrathin sections of composites, with images showing features down to 0.17 nm resolution.

TEM images on materials were collected by using a JEOL JEM-2100Plus TEM (JEOL, Akishima, Tokio, Japan) operating at an acceleration voltage of 200 kV, equipped with an 8-megapixel Gatan (Gatan, Pleasanton, CA,

USA) Rio complementary metal-oxide-semiconductor camera. The samples were deposited onto carbon-coated Cu TEM mesh grids by drop-casting dilute NPs dispersions in ethanol.

A.8 SEM

The Scanning Electron Microscope (SEM) is a powerful instrument used for morphological characterization, enabling the observation of large specimens at high resolutions and magnifications far exceeding those of ordinary light microscopy. The first SEM prototype was developed in 1942 by Russian engineer Vladimir Zvorykin.

SEM operates by directing a high-energy electron beam in a vacuum onto the sample, using a lens system to focus and deflect the beam. This interaction generates various signals, which are detected and converted into images using specialized software. The electron beam is produced by an illumination source, or electron gun, which can utilize either thermionic or field emission.

Due to its high resolution, SEM is widely utilized for assessing surface morphology, defects, surface potential, and chemical composition, often in conjunction with Energy Dispersive X-ray (EDX) analysis. SEM images on materials were collected by a Vega TS5136 XM Tescan microscope in a high-vacuum configuration. The electron beam excitation was 30 kV at a beam current of 25 pA, and the working distance was 12 mm. In this configuration, the beam spot was 38 nm. The samples were dispersed in EtOH,

deposited onto an aluminium substrate by drop-casting and covered with gold coating.

A.9 Nitrogen Physisorption

Nitrogen physisorption is a non-destructive analytical technique used to determine specific surface area, pore size distribution, and pore volume of solid materials. It is based on the physical adsorption of nitrogen gas onto the surface of a solid at a constant temperature (-196°C or 77 K), using an inert gas like N_2 due to its chemical stability and appropriate condensation properties. The adsorption phenomenon involves interactions between the surface atoms and the adsorbate via Van der Waals forces, with interaction energies around 20 kJ/mol.

The output of the analysis is an adsorption isotherm, which plots the adsorbed gas volume (V_ads) versus the relative pressure (P/P_0). The isotherm reflects how gas adsorption occurs on different pore sizes, with small pores being filled at low relative pressures and larger pores filled as the pressure increases. Near saturation pressure, all pores are filled, and the total pore volume can be determined.

The International Union of Pure and Applied Chemistry (IUPAC) classifies pores into micropores (pore size $<$ 2 nm), mesopores (2-50 nm), and macropores ($>$ 50 nm). IUPAC also recognizes six basic types of adsorption isotherms, which are indicative of the nature of the material's surface and porosity. For example, type I is typical for microporous materials, while types IV and V exhibit hysteresis loops associated with mesoporous materi-

als.

The desorption isotherm often shows hysteresis, which indicates differences in adsorption and desorption behavior, commonly due to capillary condensation in mesopores. There are four types of hysteresis classified by IUPAC: H1 (associated with homogeneous pore sizes), H2 (non-uniform pore distribution), H3 (flat-shaped pores like cracks with non-uniform sizes), and H4 (flat-shaped pores with uniform sizes).

Various models are used to analyze different regions of the adsorption isotherm. The Brunauer-Emmett-Teller (B.E.T.) method is widely used for determining specific surface area, while other methods, such as the Dubinin method and Langmuir isotherm, can also be applied. The Barrett-Joyner-Halenda (BJH) method, Horvath and Kawazoe method, and Saito-Foley method are used to evaluate pore size distribution, while the t-plot method is used to determine micropore volume, and the Kelvin equation is applied for mesopore size and volume.

Non-local density functional theory (NLDFT) is another powerful approach to determine the porosity of a sample, specifically pore size and pore size distribution, from measured gas adsorption isotherms. NLDFT builds upon density functional theory (DFT), which is a computational tool in quantum physics used to approximate solutions to the Schrödinger equation for multibody systems. In the context of gas adsorption, DFT models the properties of the adsorptive fluid, such as nitrogen, confined in porous solids. NLDFT improves upon DFT by using non-local approximations, allowing it to better represent non-homogeneous fluid behavior within pores. The advantage of NLDFT lies in its ability to characterize materials with porosity spanning

multiple scales, from micropores to mesopores and macropores, providing a continuous pore size distribution that captures the complete porosity profile of materials like activated carbons and zeolites. The analysis is performed using a Quantachrome Autosorb-1 apparatus, which provides valuable insights into the textural properties of solid materials.

A.10 Thermogravimetric Analysis

Thermogravimetric analysis (TGA) thermograms were collected using a Mettler Toledo TGA/DSC1 STARe system under a constant air flow of 50 cm^3 min^{-1}. The materials were heated from 30 °C to 150 °C at a rate of 10 °C min^{-1}, with an isothermal hold at 150 °C for 10 minutes. This was followed by heating from 150 °C to 1000 °C at the same rate, with the samples then held at 1000 °C for 5 minutes. The sample holder was an alumina pan with a volume of 75 μL, used without a pan and filled to at least half of its capacity. The analysis recorded the weight loss percentage of the samples during heating, which occurred due to decomposition reactions, oxidation, and physical processes such as vaporization and desorption.

Thermogravimetric analysis (TGA) was primarily used to estimate the number of surface hydroxyl (OH) groups present on bare nanoparticles, as well as the number of functionalization agents on grafted nanoparticles. The calculation specifically focused on the mass loss observed between 150°C and 1000°C, which is attributed to the decomposition of surface-bound hydroxyl groups and the surface-bound functionalization agent. This analysis assumes that within the selected temperature range (150°C to 1000°C), no other significant mass loss events occur, such as the loss of organic contaminants or

physically adsorbed species (which are typically lost below 150°C). These factors must be carefully considered when interpreting the results.

The equation used to calculate the OH surface content of bare nanoparticles (Equation A.1) takes into account the normalized mass loss measured during TGA in the range of 150°C to 1000°C (δwt%$_{(\mathrm{OH+OEt})\mathrm{st}}$ (NPs)) and correlates it with the moles of hydroxyl groups per gram of nanoparticles.

$$OH_{sup}[mol/g(NPs)] = \frac{\Delta wt.\%_{(OH+OEt)st}(NPs) \cdot 2}{MW(H_2O) \cdot wt.\%_{(1000°C)st}} \tag{A.1}$$

To determine the number of hydroxyl groups per unit surface area, Equation A.2 is used, which considers the moles of hydroxyl groups per gram of nanoparticles (calculated by Eq. 1) and the specific surface area of nanoparticles ($\mathrm{SSA_{BET}}$), as determined by physisorption analysis using the BET method.

$$OH_{sup}[n./nm^2] = \frac{OH_{sup}[mol/g(NPs)] \cdot N_A[n./mol]}{SSA_{BET}[m^2/g] \cdot 10^{18}[nm^2/m^2]} \tag{A.2}$$

To estimate the degree of functionalization of grafted nanoparticles, several factors must be considered: the normalized weight loss from 150°C to 1000°C of the grafted nanoparticles ($\Delta wt.\%_{(150-1000°C)st}$), the normalized weight loss from 150°C to 1000°C of the bare nanoparticles ($\Delta wt.\%_{(OH+OEt)st}$ (NPs)), the molecular weight of the organic chain lost during heat treatment (MW(Y)), and the molecular weight of water (MW($\mathrm{H_2O}$)). Equation A.3 calculates

the percentage of mass loss attributable solely to the functionalizing agent (wt.%(Y)), assuming that, on average, each silane molecule binds with two of the three available hydroxyl groups. Unreacted hydroxyl groups on both the nanoparticle surface and the functionalizing agent are also accounted for in this equation.

It is important to note that other factors, which cannot be easily predicted, may contribute to the mass loss. Consequently, the result is an estimate, not an absolute value.

$$wt.\%(Y) = \frac{\Delta wt.\%_{(150-1000°C)st} - \Delta wt.\%_{(OH+OEt)st}(NPs)}{MW(Y) - \frac{MW(H_2O)}{2}} MW(Y) \quad \text{(A.3)}$$

As with the hydroxyl group calculation, the percentage of mass loss (wt%(Y)), (calculated by Equation A.3) can be converted into σ, the number of molecules per unit area (Equation A.4), by considering the SSA_{BET} of the bare particles and MW(Y).

$$\sigma[n./nm^2] = \frac{\frac{wt.\%(Y)}{MW(Y)} \cdot N_A[n./mol]}{wt.\%_{(1000°C)st} \cdot SSA_{BET}[m^2/g] \cdot 10^{18}[nm^2/m^2]} \quad \text{(A.4)}$$

A.11 CHNS analysis

CHNS analysis is a rapid method for determining the concentrations of carbon, hydrogen, nitrogen, and sulfur in various materials, including solids, liquids, and viscous samples. This technique is applicable across multiple fields, such as pharmaceuticals, polymers, environmental science, food, and energy.

The analysis involves high-temperature combustion in an oxygen-rich environment, typically around 1000 °C, which can occur under static or dynamic conditions, often with catalysts to enhance the process. During combustion, carbon is converted to carbon dioxide, hydrogen to water, nitrogen to molecular nitrogen or nitrogen oxides, and sulfur to sulfur dioxide. The combustion products are carried away by an inert gas (helium) through heated, pure copper, which removes any unreacted oxygen and converts nitrogen oxides back to molecular nitrogen. The gases are then directed through an absorbent trap to isolate carbon dioxide, water, nitrogen gas, and sulfur dioxide.

Gas detection methods include chromatography and the use of infrared and thermal conductivity cells. Element quantification requires calibration against high-purity micro-analytical standards like acetanilide and benzoic acid. The analysis is performed using an Elementar VarioMICRO analyzer in CHNS configuration, with a measurement uncertainty of 0.1%. The combustion column operates at 1150 °C, while the reduction column is maintained at 850 °C, and measurements are normalized to a sulfanilamide standard.

In this study, CHNS analysis was primarily used to evaluate the degree of

substitution in functionalized nanoparticles. By converting the difference in the percentage of carbon mass between functionalized and bare nanoparticles into moles of the functionalizing agent, Eq. 4 can be applied to calculate the number of functionalizing agent molecules per unit area. This result can then be compared with the thermogravimetric analysis to confirm the estimate of the degree of functionalization.

While it would also be possible to perform a similar analysis using the difference in the nitrogen mass percentage (since all the functionalizing agents in this thesis contain nitrogen), this approach is problematic. Some synthetic procedures use ammonia as a catalyst, which could remain as a residue in the samples, skewing the results. Additionally, the instrument used has calibration issues for nitrogen, affecting all users, which have not been resolved.

A.12 ^{1}H TD-NMR

The ^{1}H TD-NMR analyses were performed using the Bruker Minispec instrument, a time-domain NMR spectrometer equipped with a permanent magnet that generates a magnetic field of 0.47 T and a Larmor frequency of 20 MHz for ^{1}H nuclei. Due to its rapid analysis, reproducibility, non-destructive nature, and straightforward sample preparation procedure, this instrument is widely used in various applications, from polymer studies to the agri-food industry, both in research and quality control.

The instrument consists of three main components:

- Magnet Unit: This contains the permanent magnet that generates the 0.47 T magnetic field. At the top of this unit is an aperture where a

glass tube, with an outer diameter of 10 mm, containing the sample material is inserted. The sample is positioned inside the instrument at a height of 14.3 cm from the inlet nozzle to the center of the sample in the tube (usually occupying about 1 cm from the bottom of the tube). This ensures the sample is at the point of maximum magnetic field homogeneity. Surrounding the probe is a coil that generates RF pulses and collects the electrical signal from the free induction decay (FID), as explained in the previous chapter on NMR mechanisms.

- Magnetic Control Unit: This unit consists of various electronic boards responsible for generating the RF pulses according to the user-defined settings and receiving the NMR signal.

- Gradient Unit: Positioned between the magnet and magnetic control units, this component allows the generation of gradient pulses to create controlled inhomogeneity in the magnetic field.

The instrument is equipped with a BVT3000 temperature control system, which operates with nitrogen gas flow and calibrates the temperature using an external thermocouple system with an accuracy of $\pm$ 1 K and a precision of 0.1 K. For low-temperature operations, the instrument can be connected to a liquid nitrogen evaporator controlled by the same unit.

Hahn Echo (HE)

Field inhomogeneities, which are especially prominent in solid samples and low-field instruments, cause significant spin deflection. As a result, in a standard NMR experiment that includes a 90° pulse followed by signal acqui-

sition, the transverse magnetization decays more quickly than anticipated. The time constant associated with this faster decay is known as T_2*, and the relation $T_2 \leq T_2$* always holds true.

To address the issue of inhomogeneities and accurately measure T_2, Hahn Echo (HE) sequences are commonly employed. These sequences mitigate the problem by using pulses that refocus the spins, which lose phase coherence due to field effects, resulting in what is known as a spin echo.

The Hahn Echo sequence proceeds as follows (Figure A.1):

1. A 90° pulse is applied, rotating the magnetization from the z-axis to the xy-plane.

2. A variable delay time, τ, is introduced, during which the magnetization partially recovers its initial state.

3. A 180° pulse is then applied to refocus the spins. This 180° pulse reverses the precession of the spins in the xy-plane, leading to the formation of the echo signal.

By repeating the experiment with different τ values, the T_2 relaxation time can be measured. The experimental data obtained are then fitted using the Equation A.5

$$I(t) = I_0(e^{\frac{\tau}{T_2}}) \tag{A.5}$$

where I(t) is the signal intensity at time τ, I_0 is the initial signal intensity, and T_2 is the transverse relaxation time.

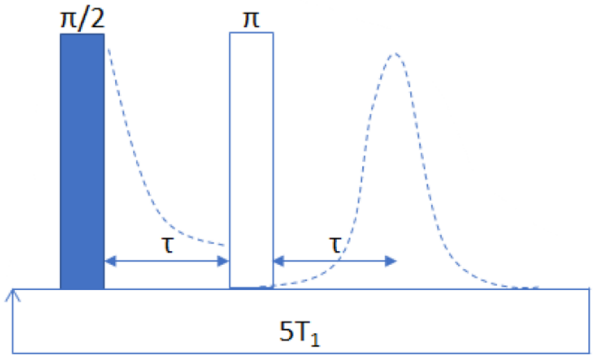

Figure A.1: Hahn Echo sequence